




5-2012

Characteristics and Functionalities of Natural and Bioinspired Nanomaterials

Lijin Xia
lxia@utk.edu

Follow this and additional works at: https://trace.tennessee.edu/utk_graddiss

 Part of the [Biology and Biomimetic Materials Commons](#), and the [Biomedical Engineering and Bioengineering Commons](#)

Recommended Citation

Xia, Lijin, "Characteristics and Functionalities of Natural and Bioinspired Nanomaterials. " PhD diss., University of Tennessee, 2012.
https://trace.tennessee.edu/utk_graddiss/1373

This Dissertation is brought to you for free and open access by the Graduate School at TRACE: Tennessee Research and Creative Exchange. It has been accepted for inclusion in Doctoral Dissertations by an authorized administrator of TRACE: Tennessee Research and Creative Exchange. For more information, please contact trace@utk.edu.

To the Graduate Council:

I am submitting herewith a dissertation written by Lijin Xia entitled "Characteristics and Functionalities of Natural and Bioinspired Nanomaterials." I have examined the final electronic copy of this dissertation for form and content and recommend that it be accepted in partial fulfillment of the requirements for the degree of Doctor of Philosophy, with a major in Biomedical Engineering.

Mingjun Zhang, Major Professor

We have read this dissertation and recommend its acceptance:

William R. Hamel, Wei He, Ramón V. León, Siqun Wang

Accepted for the Council:

Carolyn R. Hodges

Vice Provost and Dean of the Graduate School

(Original signatures are on file with official student records.)

Characteristics and Functionalities of Natural and Bioinspired Nanomaterials

A Dissertation
Presented for the
Doctor of Philosophy Degree
The University of Tennessee, Knoxville

Lijin Xia
May 2012

Copyright © 2012 by Lijin Xia
All rights reserved.

ACKNOWLEDGEMENTS

I would like to express my sincere gratitude to my advisor, Dr. Mingjun Zhang, for his support, guidance, and encouragement during this endeavor. Without his insightful and constructive guidance on the research topics, I would not have been where I am now.

I gratefully acknowledge other professors in my doctoral committee, Dr. William R. Hamel, Dr. Wei He, Dr. Ramón V. León, and Dr. Siqun Wang for taking their precious time to serve on my committee and giving insightful suggestions.

I would also like to extend my appreciation to my other colleagues and friends for their assistance and generous support on my research. I would also like to recognize the Army Research Office and the Department of Mechanical, Aerospace and Biomedical Engineering, the University of Tennessee for their financial support.

Finally, I would like to thank my families. Their best wish is always my best gift.

ABSTRACT

Green nanoscience is a rapidly emerging field that aims to achieve the maximum performance and benefits from nanotechnology, while minimizing the impact on the environment. In this study, several methods for the green nanomanufacturing of biomedically important nanomaterials, specifically through the use of natural plants, have been extensively investigated. It was found that natural nanomaterials are inherent within plants, and can be further manipulated for potential biomedical applications. In addition, the metabolites and reductive capacity of plant extracts can be used to synthesize metallic nanoparticles with advantages over semi-conductor based nanomaterials. Nanoparticles were found to exist in the extracts produced from tea leaves, the adventitious roots of English ivy (*Hedera helix*), the adhesive of the sundew (*Drosera sp.*), and the rhizome of the Chinese yam (*Dioscoera opposita*). These nanoparticles showed highly uniform repeating structures varying in size from 50-200 nm. Plant-derived nanofibers were also observed in the traditional Chinese medicine, Yunnan Baiyao, and from the polysaccharide components of the sundew adhesive and the viscous pulp extract from the Chinese yam. The nanofibers observed from the dried polysaccharides of the sundew and Chinese yam formed network structures with various pore sizes and fiber diameters. Due to their organic backbone, advantageous material properties, and biocompatibility, these natural nanomaterials offer significant advantages for biomedical applications. As such, these natural nanomaterials were further tested from medical prospects. Ivy

nanoparticles were found to have unique optical property, blocking the transmission of ultraviolet light, which has potential for sunscreen and cosmetic applications. Nanofiber networks created from the sundew and Chinese yam showed strong cell attachment and proliferation with multiple cell lines, indicating their potential use as coatings for implants in the field of tissue engineering. Finally, gold and silver nanoparticles were synthesized using the extracts from homogenized ivy rootlets, by live sundew plant, or by herbicide additive. Through this study, the potential of plants has been demonstrated to vastly expand the current field of nanomanufacturing, and to reduce the environmental concerns associated with synthetic nanomaterials.

TABLE OF CONTENTS

| | |
|---|----|
| CHAPTER I. Introduction | 1 |
| Organization of the Dissertation | 7 |
| CHAPTER II. Identification of nanofibers in the Chinese herbal medicine: | |
| Yunnan Baiyao | 14 |
| Introduction | 15 |
| Materials and Methods | 18 |
| Yunnan Baiyao | 18 |
| Sample preparation | 18 |
| AFM imaging..... | 18 |
| Results and Discussion..... | 19 |
| CHAPTER III. Evaluation of nanofibrillar structure of Dioscoera oppositae | |
| extract for cell attachment..... | 27 |
| Introduction | 28 |
| Materials and Methods | 32 |
| Extraction of soluble and insoluble components | 32 |
| Atomic force microscopy imaging | 33 |
| Cell culture..... | 33 |
| Substrate coating..... | 34 |
| Cell attachment..... | 35 |
| Soluble extract and cell interactions | 35 |
| Biomolecules in soluble extract..... | 35 |
| Results and Discussion | 36 |
| Nanofiber-based scaffold from the Dioscorea oppositae soluble extract | 36 |
| Formation of nanofibers from insoluble components | 38 |
| HeLa cell attachment and growth on soluble extract formed scaffolds | 40 |
| MC3T3 attachment and growth on soluble extract formed scaffolds | 41 |
| Soluble components and cell surface interactions | 44 |
| Biomolecules in soluble extract..... | 46 |
| Conclusions..... | 47 |
| CHAPTER IV. Nanofibers and nanoparticles from the insect-capturing | |
| adhesive of the sundew (Drosera) for cell attachment | 49 |
| Introduction | 50 |
| Materials and Methods | 53 |
| Plants..... | 53 |
| Sample preparation | 54 |
| Atomic force microscopy..... | 56 |
| Transmission electron microscopy..... | 56 |
| Results and Discussion | 57 |
| Nanostructure of the sundew adhesives | 57 |
| Polysaccharides in the nanostructured sundew adhesives..... | 59 |

| | |
|---|-----|
| Nanoparticles in the fibrous adhesives | 61 |
| Chemical characterization of metal components in adhesives..... | 61 |
| Mechanical properties of sundew adhesives | 65 |
| Neuron cell response to the nanostructured sundew adhesives..... | 69 |
| Conclusions..... | 72 |
| | |
| CHAPTER V. Naturally occurring nanoparticles from English ivy: an alternative to metal-based nanoparticles for UV protection | 74 |
| Introduction | 75 |
| Materials and Methods | 79 |
| Ivy nanoparticle isolation..... | 79 |
| Atomic force microscopy..... | 80 |
| Sample preparation | 81 |
| UV/Vis extinction..... | 81 |
| Cytotoxicity study..... | 81 |
| Nanoparticle degradation..... | 82 |
| Statistical analysis | 83 |
| Results and Discussion | 83 |
| Ivy nanoparticle isolation and topographic characterization..... | 83 |
| UV extinction of ivy nanoparticles | 84 |
| Cytotoxicity | 87 |
| Degradation | 90 |
| Skin penetration..... | 91 |
| Conclusions..... | 95 |
| | |
| CHAPTER VI. Characterization of English ivy (<i>Hedera helix</i>) adhesion force and imaging using atomic force microscopy | 98 |
| Introduction | 99 |
| Materials and Methods | 103 |
| Sample preparation | 103 |
| AFM imaging..... | 104 |
| Adhesion force measurement..... | 105 |
| Results and Discussion | 106 |
| Nanoparticles produced from in vitro ivy rootlets | 106 |
| High adhesion strength of ivy nanoparticles | 108 |
| High elasticity of ivy nanoparticles | 109 |
| Time-based loss of adhesion | 111 |
| Limited change in extension length and Young's modulus | 113 |
| Mechanics model of ivy nanoparticle adhesion..... | 117 |
| Conclusions..... | 120 |
| | |
| CHAPTER VII. Live sundew plant or extracts from ivy rootlets for metal nanoparticle synthesis | 122 |
| Introduction | 123 |
| Materials and Methods | 125 |

| | |
|--|---------|
| Chemicals and plants..... | 125 |
| Preparation of ivy rootlet extract solutions | 126 |
| Biosynthesis of gold crystals from ivy rootlet extracts | 126 |
| UV/Vis spectroscopy study | 127 |
| DLS analysis of gold crystals | 127 |
| Biosynthesis of silver nanoparticles in live sundew plant..... | 128 |
| Tracking of fluorescent quantum dots in live sundew plant..... | 128 |
| SEM analysis of gold or silver particle structure | 129 |
| Results and Discussion | 129 |
| UV/Vis spectroscopy of gold crystals from ivy rootlet extracts | 129 |
| Structures of gold crystals from ivy rootlet extracts..... | 130 |
| Silver nanoparticle production from live sundew plant | 135 |
| Tracking of nanoparticle translocation in sundew plant | 137 |
| Conclusions..... | 139 |
| CHAPTER VIII. One-step size-controlled synthesis of gold nanoparticles with surfactant-modified surface properties..... | 140 |
| Introduction | 141 |
| Materials and Methods | 145 |
| Preparation of gold nanocrystals | 145 |
| Characterization..... | 145 |
| Results and Discussion | 146 |
| Facile synthesis of AuNPs in a single mixture | 146 |
| Effect of AuCl ₄ ⁻ and Silwet L-77 concentration on AuNP synthesis | 149 |
| Morphological control of AuNPs by NaOH | 154 |
| Size-controlled synthesis of AuNPs by AgNO ₃ | 156 |
| FTIR analysis of AuNPs..... | 159 |
| Stability and endocytosis of the AuNPs | 159 |
| Conclusion | 165 |
| CHAPTER IX. Conclusions and recommendations | 166 |
| LIST OF REFERENCES..... | 171 |
| VITA..... | 190 |

LIST OF TABLES

| | | |
|---------|---|-----|
| Table 1 | Identified components from Yunnan Baiyao..... | 17 |
| Table 2 | Size of AuNPs measured by DLS. | 152 |

LIST OF FIGURES

| | | |
|-----------|---|-----|
| Figure 1 | AFM topography image of nanoparticles from green tea. | 10 |
| Figure 2 | AFM topography image of nanoparticles from Chinese yam. | 11 |
| Figure 3 | Nanofibers isolated from Yunnan Baiyao solution. | 20 |
| Figure 4 | 3-D rendering of nanofibers against the silica wafer background. | 22 |
| Figure 5 | Phase image of nanofibers showing the difference in phase shift compared to background. | 23 |
| Figure 6 | Morphology of soluble extract from Dioscorea oppositifolia. | 37 |
| Figure 7 | Morphology of nanoparticles and nanofibers from insoluble extract of Dioscorea oppositifolia. | 39 |
| Figure 8 | HeLa cell attachment and proliferation in the Dioscorea oppositifolia soluble extract coated surface. | 42 |
| Figure 9 | MC3T3 cell attachment and proliferation in the Dioscorea oppositifolia soluble extract coated surface. | 43 |
| Figure 10 | Interaction of soluble extract with HeLa and MC3T3 cells. | 45 |
| Figure 11 | Pictures of three species of the sundew. | 51 |
| Figure 12 | AFM images of the sundew adhesive for three sundew species. | 58 |
| Figure 13 | AFM overlay of Alcian Blue stained sundew adhesive. | 60 |
| Figure 14 | Nanoparticle size characterization. | 62 |
| Figure 15 | TEM images showing the crystalline structure of the nanoparticles. | 64 |
| Figure 16 | EDS spectra of control and nanoparticle samples. | 66 |
| Figure 17 | Measurements of extension from the liquid and dried sundew adhesives. | 68 |
| Figure 18 | Light and confocal micrographs of PC12 cells attached to various substrate surfaces. | 71 |
| Figure 19 | AFM characterization of ivy nanoparticles. | 85 |
| Figure 20 | UV extinction spectra. | 86 |
| Figure 21 | Cytotoxicity analysis. | 89 |
| Figure 22 | Biodegradability of ivy nanoparticles. | 92 |
| Figure 23 | Distribution of nanoparticles in SC layer of skin. | 96 |
| Figure 24 | Nanoparticles released from the in vitro grown ivy rootlets. | 107 |
| Figure 25 | Adhesion force of ivy adhesive measured by AFM. | 110 |
| Figure 26 | Change of adhesion force within 24 hours. | 112 |
| Figure 27 | Increased Young's modulus with time for ivy nanoparticles. | 115 |
| Figure 28 | Decreased extension length with time for ivy nanoparticles. | 116 |
| Figure 29 | The relationship of pull-off force and effective elastic modulus of nanoparticles. | 119 |
| Figure 30 | UV/Vis spectra of gold crystals from ivy rootlet extracts. | 131 |
| Figure 31 | SEM images for the gold crystals from ivy rootlet extract solutions. | 133 |
| Figure 32 | Size distribution of gold crystals synthesized by ivy rootlet extracts. | 134 |
| Figure 33 | Confirmation of silver nanoparticle synthesis in sundew stem. | 136 |

| | | |
|-----------|--|-----|
| Figure 34 | Confocal microscopy images of stem and tentacles of sundew plant fed with fluorescent quantum dots. | 138 |
| Figure 35 | Confirmation of AuNP synthesis. | 148 |
| Figure 36 | Tracking of λ_{\max} of AuNP SPB with time. | 150 |
| Figure 37 | AuNPs under different concentration of $\text{HAuCl}_4 \cdot 3\text{H}_2\text{O}$ | 153 |
| Figure 38 | NaOH led to the homodispersion of AuNPs. | 155 |
| Figure 39 | AgNO_3 led to the decreased size and increased clustering of AuNPs. | 157 |
| Figure 40 | DLS data for the AuNPs under different concentration of AgNO_3 | 158 |
| Figure 41 | FTIR of AuNPs. | 160 |
| Figure 42 | Stability of AuNPs. | 162 |
| Figure 43 | Endocytosis of AuNPs in MC3T3 cells. | 163 |
| Figure 44 | Dark-field light microscopy images of MC3T3 cells with or without AuNPs. | 164 |

CHAPTER I. INTRODUCTION

In an era when “nano” becomes a label of high technology, the identification or successful synthesis of new functional nanomaterials with unique properties has greatly advanced the techniques or brought forth new ideas in the related fields. The development of nanofibers has rapidly enhanced the scope for fabricating scaffolds that can potentially mimic the architecture of natural human tissue at the nanoscale, which leads to the next generation of materials in tissue engineering. Recently developed highly regular, single-crystalline nanopillar array of optically active semiconductors on aluminum substrates enable high absorption of light and efficient collection of carriers, which hasn't been achieved previously using other macroscale materials [1]. The strategy to incorporate nanoparticles into the delivery of therapeutic or imaging agents to cancer has shown great promise for early diagnosis and targeted drug delivery that could revolutionize cancer treatment [2]. Today, even some clay are being manufactured to nanoclay which can then be modified to organic-inorganic nanomaterials with potential use in polymer nanocomposites, as rheological modifiers, gas absorbents and drug delivery carriers [2]. Like these and many other innovations, nanomaterials with attractive properties have experienced rapid progress with the introduction of concept of “nano”, such as the invention of nanoneedle, nanostar, nanorod, nanoshell, nanopore and many others to come in the future.

The beauty of nanotechnology lies in not only the invention of functionally advanced novel materials, but also facilitating our understanding of the current

systems that may rarely have opportunities to be understood without going into this tiny scale. A well-known example is gecko that climbs freely over the ceiling without any external assistance. The secret of its free movement lies in the internal assistance of millions of tiny, spatula-shaped hairs on its toepads which are not recognized until small-scale examination. Another example is the identification of unique self-cleaning property of lotus leaves [3]. It is found that a hierarchical structure that goes into nanoscale on the lotus leaves has contributed to its super hydrophobic surface with self-cleaning capacity [4].

As in gecko toepads and lotus leaves, nature has evolved objects with high performance and multifunctionality using commonly found materials over the history of evolution. These common materials are organized from the molecular to the nanoscale, microscale and macroscale structures in a hierarchical manner to make up a myriad of different functional elements [5]. It is thus not surprised that nanoscale materials are one of the main structures found in nature that support the life through the long history of earth under even extreme conditions. Many current existing viruses themselves simply are functionally active nanoparticles. In bacteria, the flagella that rotate at a high speed of over 10,000 revolutions per minute (rpm) are driven by a nanoscale flagellar motor with a diameter of less than 50 nm [6]. In animal, excellent thermal-insulating property of duck feather is attributed mainly to a nanoscale and hierarchical structure with trapped air inside it [7]. In plant, a slippery epicuticular wax layer that plays a crucial role in insect trapping and prey retention on leaves is composed of a large

number of nanocellulose tubules with an outer diameter of 100 nm and inner diameter of 70 nm [8]. Although some natural nanomaterials will eventually develop to micro- to macro-scale structures to fulfill their functions, many nanostructures themselves are still the key components towards their micro- to macro-scale performance.

The preference and high performance of nanostructures in nature is attributed to their unique properties due to the unusually high surface area to volume ratio, which alters the mechanical, thermal, catalytic and other properties of the materials. The increase in surface area to volume ratio also leads to the increasing dominance of atoms on the material surface, thus altering the material properties and interactions with surrounding materials [9]. Based on the limited number of commonly found materials, nature has evolved to exploit a complex interplay between the surface structure and morphology of materials besides their physical and chemical properties to achieve multifunctionality. A wide variety of examples can be found which include self-repairing of wounds, self-cleaning of lotus leaves, energy conversion of chlorophyll, dry adhesion of gecko toepads, super-hydrophobicity of water fern leaves, etc.

The identification of natural nanomaterials and the confirmation of their contribution to the unique properties of materials have triggered direct applications or bioinspired and biomimetic approaches to design nanomaterials for human purpose. The discovery of the nano- to micro-structure in gecko toepads has promoted the synthesis of microfiber- and nanofiber-based dry

adhesives that equal to, and in some cases exceed, in the aspect of shear stresses, that of real gecko [10]. Climbing robots based on the synthetic dry adhesives are being designed for potential applications in firefighting, spy, or under other extreme conditions that are not accessible to human. The biomimetic approaches inspired by the discovery of nanostructures from lotus leaves have led to the development of various nanofibrillar super-hydrophobic and self-cleaning surfaces commercially or in the laboratory, such as self-cleaning, transparent and permanent paints, roof tiles, fabrics and coatings for glassware, vehicles, lighting and optical instruments [11]. The identification of arrays of multilayered nanometer structures covering the scales of butterfly wings has advanced the synthesis of domino-like photonic nanostructures for applications in optical gas sensor, filter for flat-panel display, and other optical devices [12].

Till today, bioinspired and biomimetic nanomaterials have experienced success in very broad areas, such as in structural coloration, wet and dry adhesion, energy conversion and conservation, self-cleaning, antireflection, sensory-aid mechanisms, etc. Interest of nanostructures in medicinal applications also begins to explode in recent years, due to the innovative understanding of nanomaterials-cell/tissue interactions. In human, cell is the basic unit to be organized into tissues and organs in the body, and its normal functions and responses are important for human health. Cell activities and responses have a long history to be attributed to the chemical signals inside itself or from its surroundings. Recent intensive research towards nanoscale investigations,

however, suggests that nanostructures of surrounding materials, such as extracellular matrix, play important roles in many aspects of cell activities, including cell attachment, spreading, proliferation and differentiation, even for stem cells [13].

Thus, towards medical applications, such as in tissue engineering and regenerative medicine, a lot of attention has been diverted recently to bioinspired and biomimetic approaches, to synthesize nanomaterials with intended functions. Aligned peptide amphiphile nanofibers integrated with Sonic hedgehog have showed success in the regeneration and repair of cavernous nerve [14]. Self-assembly of bioactive nanofibers into the pores of titanium alloy foams have been applied for bone repair [15]. Recent study by Stout et al. found that poly(lactic-co-glycolic acid)-carbon nanofiber composites could form conductive scaffolds which promote adhesion and proliferation of cardiomyocytes and neurons in the cardiac tissue, thus serving perfectly for cardiovascular applications [16].

As in the above and in many other cases, the bioinspired and biomimetic approaches to synthesize nanomaterials usually require elaborate design, complicated preparation and accurate controlling process, which prevent a high yield of functional materials for actual applications. Another concern for the synthetic nanomaterials is its cytotoxicity in actual applications, especially in *in vivo* medical applications. For these reasons, natural existing nanomaterials with expected functionalities are considered as preferred candidates for biomedical

applications, thus having drawn a great attention in recent years. Encouraging findings include microbial cellulose working as a wound-healing device for severely damaged skin and as a small-diameter blood vessel replacement, and crustacean-derived chitosan for wound dressing and drug delivery.

While natural nanomaterials from bacteria and animals have been introduced and their applications in medicine have been validated since their discovery, nanomaterials from plant source have rarely been reported, especially from medical prospect. It is thus well worth to investigate nanomaterials from plant, the largest category of materials on the continents, as a potential resource of materials for medical applications.

In this study, possible existence of nanomaterials are thus surveyed from plants that show attractive characteristics either due to their unique physical properties or due to their wide applications for human health. Specific focus is placed on the nanoscale understanding of the plant materials in regarding to their structure, physical, biochemical and mechanical properties that lead to their applications in medicine. Inspired by the capacity to grow beneficent nanomaterials by plant, next step in the study is to exploit plant themselves or bio-inspired approaches to intentionally mimic or “green-manufacture” medicinal nanomaterials towards applications.

Organization of the Dissertation

To identify potential functional nanomaterials from nature, plant materials with well-known functionalities were selected and investigated at the first stage of the

study. Herbal medicine, mainly traditional Chinese medicine, was tested first due to its long history in the applications for human benefits. Yunnan Baiyao is one of the most famous traditional Chinese medicines in western countries. It has been widely used in bleeding healing and increasing circulation. So, in Chapter II, nanostructures from this herbal medicine were first examined, and the nanostructures that may relate to medical effects of this medicine was discussed.

Another popular herbal medicine, *Rhizoma dioscoera*, was addressed next in Chapter III. *Rhizoma dioscoera*, also known as Chinese yam, Korea yam and Japanese mountain yam, is especially effective in relieving cough and soothing mucous membrane. From its mucilage part, a large amount of liquid adhesive was collected, which was found to form nanofiber network on the solid substrates under examination. Synthetic nanofiber network has been widely used in tissue engineering applications [17]. To verify similar functionality of natural occurring nanomaterials from yam, cell culture studies including cell attachment and proliferation were performed on this nanofiber network. HeLa cells, a cell line derived from cervical disease, were found to grow well on the *Rhizoma dioscoera* mucilage coated surface. This observation provides direct evidence that plant-derived nanomaterials might possess essential properties required for tissue engineering applications in medicine.

After confirmation the medical benefits of plant nanomaterials with known functionalities, the immediate aim was to examine plant materials without reported medical effects. In Chapter IV, plant adhesive with unique mechanical

properties from *Drosera*, commonly known as sundew, was studied. The adhesive on the tentacles of sundew plant has attracted interest due to its capacity to capture preys, such as flies. No obvious medical effect has been reported for the adhesive part from sundew. Similar to the studies from *Rhizoma dioscoera*, the nanostructures formed by the adhesive were first examined, followed by the cellular response to the nanostructures. Various nanofiber-formed networks were observed from adhesives of different species of sundew, and different cell types including neuron cells were found to attach and grow well on these nano-fibrous surfaces. This discovery further substantiates that plants, even some rarely known plants, might provide a potential source of nanomaterials with essential medical benefits.

Except nanofibers, another important format of nanomaterials, spherical nanoparticles, have also been incorporated into the study. As shown in Figures 1 and 2, different sizes of nanoparticles could be clearly found from the plants with medical effects, such tea leaves and *Rhizoma dioscoera*. The identification of nanoparticles from plants is not surprising since nanoparticles have high surface-to-mass ratio which might provide them unique properties. One of the recent discoveries in our lab is the nanoparticles from ivy rootlets [18], which are believed to provide ivy strong adhesion force to attach and climb onto high buildings and the top of trees. Towards medical applications, natural nanomaterials including nanoparticles possess some obvious advantages over the synthetic materials, such as biocompatibility and biodegradability, especially

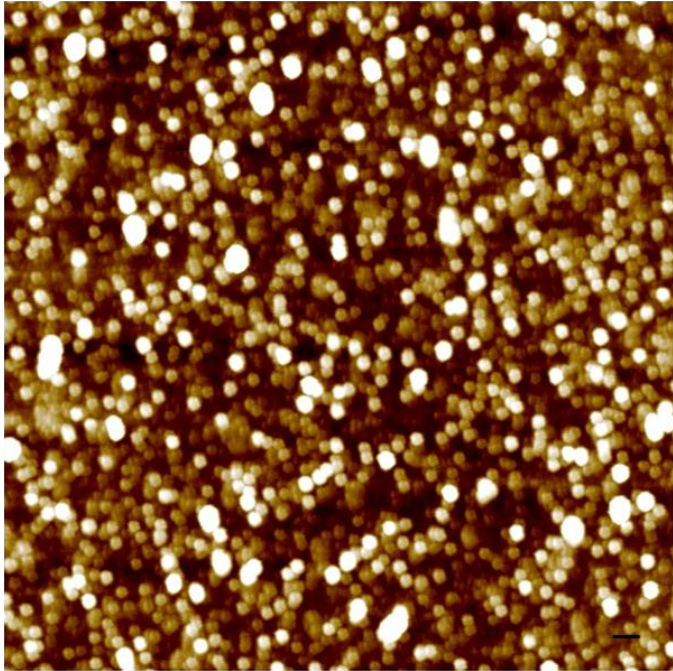


Figure 1 AFM topography image of nanoparticles from green tea.

Scale bar = 200 nm.

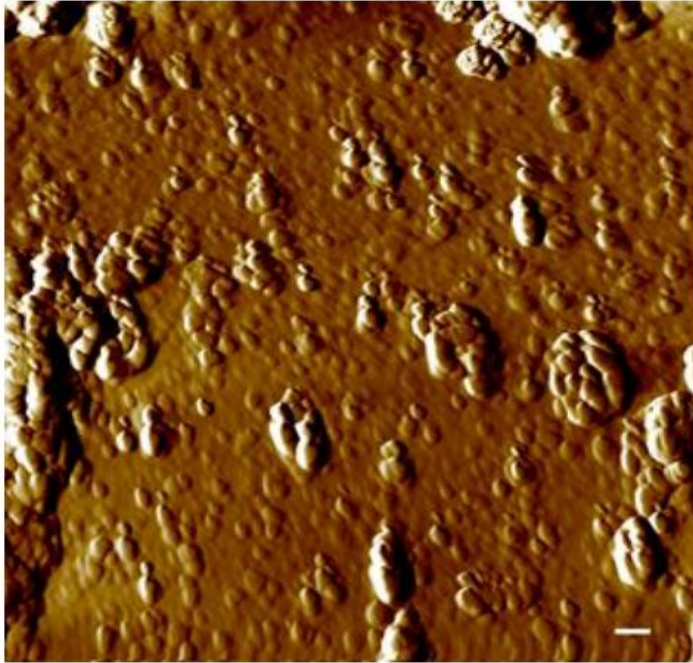


Figure 2 AFM topography image of nanoparticles from Chinese yam.

Scale bar = 500 nm.

for *in vivo* applications. Combined with their unique properties from nature nanoparticles, they might offer some unexpected benefits in human health. Using ivy nanoparticles as a case, detailed studies were performed to evaluate whether and how the unique properties of nature nanoparticles might be exploited from medical aspect. In Chapter V, light scattering and absorbance properties of the ivy nanoparticles were comprehensively studied towards cosmetic applications. In Chapter VI, the focus was turned to the mechanical properties of the ivy nanoparticles. Possible mechanisms that contribute to the strong adhesion of ivy nanoparticles were investigated. Through the study, it is expected that unique adhesion properties of ivy nanoparticles might inspire the design of stronger, more biocompatible and generally accepted medical adhesives.

The identified nanofibers and spherical nanoparticles from plants or nature provide us a valuable source of green nanomaterials towards medical applications. However, it should be recognized that limitations still exist since there are limited functionalities or type of nanomaterials that could be extracted from plants or nature. An optimal and alternative strategy would be to utilize plant's capacity as a manufacturing system to grow nanoparticles with desired functionalities, that is, to directly grow non-inherent nanomaterials with object functions from plant. This approach will greatly expand the capacity and role of plant in providing beneficent nanomaterials in green nano-manufacturing. In Chapter VII, the focus was placed on using ivy rootlets and live sundew plants to grow metal nanoparticles with medical benefits.

Only limited amount, types and sizes of nanomaterials might be synthesized by plant or nature. To overcome this limitation, one of potential strategies is to add into plants some chemicals, which are non-toxic and will cooperate with inherent molecules from plants to synthesize non-inherent nanomaterials. The selection of proper chemicals might be blind at this moment but one of intuitive choices would be insecticides or other additives that are already developed for plants. In Chapter VIII, a case was reported to show how chemical additives to plants could “green manufacture” nanoparticles, such as gold nanoparticles. Following this preliminary study, the eventual goal in the future would be to accurately control the growth of nanoparticles from plant with the assistance of chemical additives.

The overall objective of the present study is to furnish an idea to study or pay more attention to nature especially plant system towards biosynthesis of nanomaterials. This will greatly expand the current resource of nanomaterials and minimize the requirement of synthetic nanomaterials. Also, the understanding of plant-derived nanomaterials with cell/tissue interactions will assist with the explanation of medicinal effects of herbal medicine, facilitating its popularization and general acceptance. More importantly, through this study, it is expected that plant-inspired approaches can be exploited towards the intentional synthesis of nanomaterials with desired functionalities and properties. This study thus serves to promote the real “green manufacturing” of functional nanomaterials from plant or nature towards medical applications.

**CHAPTER II. IDENTIFICATION OF NANOFIBERS IN THE
CHINESE HERBAL MEDICINE: YUNNAN BAIYAO**

A version of this chapter was originally published by Scott C. Lenaghan, Lijin Xia and Mingjun Zhang:

Scott C. Lenaghan, Lijin Xia and Mingjun Zhang. "Identification of nanofibers in the Chinese herbal medicine: Yunnan Baiyao." *Journal of Biomedical Nanotechnology* 5 (2009): 472-476.

Lijin Xia performed the experiments in this study. Scott C. Lenaghan analyzed the data and wrote the manuscript. Dr. Mingjun Zhang initiated and manipulated the project.

Introduction

Yunnan Baiyao (syn Yunan Bai yao, Yunnan Paiyao) is a traditional Chinese herbal medicine that has been used for the treatment of a variety of ailments since its inception in 1902. The formulation of this medicine remains a closely guarded Chinese secret, and remained unknown to the western world until the Vietnam War (1959–1975) when American troops began to notice that the Vietnamese carried small bottles with them to treat battlefield wounds. Upon further inquiry, the Americans discovered that the Vietnamese were using bottles of Yunnan Baiyao, and purchased these bottles to treat their own wounds [19].

Claims have been made that Yunnan Baiyao can treat a wide variety of diseases and ailments. Most commonly, Yunnan Baiyao has been used to reduce bleeding and to increase clotting and platelet aggregation. It has also been reported that Yunnan Baiyao can be used as an antibacterial or even

applied topically to help to seal wounds [20]. Other reports claim that it has cytotoxic effects and can be used for the treatment of cancer [21-25]. Despite its widespread use, very little clinical evidence exists to substantiate these claims and the mechanism used to generate these health benefits remains unknown. Due to the secretive nature, only some of the components of Yunnan Baiyao are known (Table I). Isolation of these components from Yunnan Baiyao has led to the discovery of a large number of saponins that contribute to the antibacterial and anti-inflammatory properties of the drug [26]. Other components have been shown to have both anti-coagulant and platelet aggregating roles, which seem to counter one another [27-29]. In the early 1970's, there was a theory stating that Yunnan Baiyao contained micro- to nano-scale particulate matter that could potentially help to cause platelet aggregation, although this claim was never proven [20].

Recently, however, it has been demonstrated that nanoparticles and nanotubes can have drastic effects on the abilities of platelets to activate and respond to injury. Researchers have found that the effect of platelet aggregation induced by nanoparticles is dependent on the composition of the nanoparticles. Gold nano-shells strongly increase platelet aggregation and can induce thrombosis, while nano-silver has anti-coagulatory effects that decrease the formation of clots [30, 31]. A more comprehensive study found that the greatest effects on platelet aggregation were seen with carbon nanotubes, followed by the mixed carbon nanoparticles [32]. Isolated biological nanoparticles have also been

Table 1 Identified components from Yunnan Baiyao.

| Common Name | Scientific Name | Known Functions |
|----------------------------|--|--|
| Pseudoginseng, San qi | <i>Panax pseudoginseng</i> , | Decreased platelet activation [27, 33-35] |
| Wild yam root | <i>Dioscorea hypoglauca</i> | Cytotoxicity of cancer cells [22, 23] |
| Sweet geranium | <i>Erodium stephanianum</i> | Antimicrobial, antiviral, antioxidative [36-38] |
| Gao liang jiang Borneol | <i>Alpinia officinarum</i> | Antimicrobial [26] Penetration enhancer, cytotoxicity, antimicrobial [21, 28, 39] |
| Dragon's blood | <i>Daemonorops draco</i> | Cytotoxicity, anti-platelet functions [24, 30] |
| Himalayan trillium | <i>Paris polyphylla</i> var. <i>chinensis</i> | Cytotoxicity, antimicrobial [25, 40-42] |

shown to have increased effects on platelet aggregation, leading to faster wound healing *in vitro* [43] .

Materials and Methods

Yunnan Baiyao

Yunnan Baiyao was purchased from a Chinese Grocery Store, Ranch 99, Milpitas, CA. The powder was dissolved in distilled water at varying concentrations from 10 mg/ml to 1 mg/ml. The powder was vortexed until a uniform distribution was achieved and placed at 4°C until use.

Sample preparation

To reduce the number of large particulates, the solution containing the Yunnan Baiyao powder was filtered through a 0.4 µm and 0.2 µm sterile syringe filter. After filtration, the solution was again vortexed, and then approximately 20 µl was spotted onto a silica wafer that had been previously cleaned, sonicated, and dusted with a compressed air canister. Controls using distilled water and a bare silica wafer were prepared alongside the experimental samples. All samples were allowed to dry overnight at 23°C under a laminar flow hood. Experiments were conducted in triplicate to ensure that the results were reproducible.

AFM imaging

Atomic force microscopy (AFM) imaging was performed with an Agilent 5500 AFM system (Agilent Technologies, Chandler, AZ). Samples were scanned

under both contact and AC modes to determine the best imaging conditions for the samples. A Budget Sensors® Tap300Al cantilever (Resonant freq. 300 kHz, force constant 40 N/m) was used for optimal imaging. Image processing was performed using the PicoImage® (Agilent Technologies) software package. Samples were scanned by two independent researchers to verify the identity of the fibers, and to ensure no artifacts were introduced. Random fibers (100) were chosen for analysis of length, height, and diameter from three separate preparations. All measurements were made using PicoImage® software provided by Agilent Technologies.

Results and Discussion

By using AFM, a large number of micro- and nano-scale particulates were observed from the recommended concentration of Yunnan Baiyao (10 mg/ml). At this concentration, the density of particulates was too great to be accurately imaged. To reduce the number of large particulates, a dilution series were conducted to determine the optimal imaging conditions. It was determined that a concentration of 1 mg/ml in distilled water was optimal for imaging. To reduce the number of microscale particulates, the solution was passed through a sterile 0.2 µm syringe filter. This eliminated the background particles, and provided a smooth surface for imaging nanoscale structures (Figure 3). To ensure that no contamination occurred during sample preparation, controls were established for distilled water, syringe-filtered distilled water, and the filter itself. The control

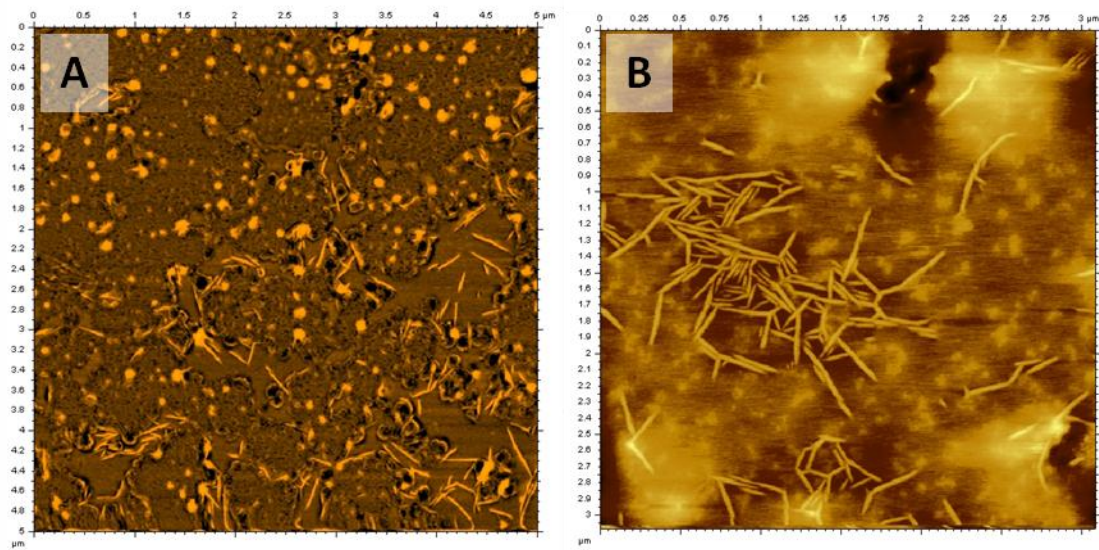


Figure 3 Nanofibers isolated from Yunnan Baiyao solution.

(A) A 5x5 μm scan showing the organization of nanofibers on the surface of the silica wafer. (B) A 3x3 μm scan of surface showing nanofibers.

samples were free from nanoparticles, and imaging of the filter revealed no damage from use. Non-uniform nanoparticles were observed in all Yunnan Baiyao samples, but varied greatly in size and did not possess a definitive shape. Contrary to the nanoparticle data, a large number of uniform nanofibers were present in the Yunnan Baiyao solution (Figure 3). Measurements from 100 fibers revealed an average length of 299.6 nm (Stdev =163.2 nm), with a wide range, from 86-726 nm. On subsequent scans, long fibers were observed ranging from 1-1.5 μm . The large variation in length of the fibers was due to shearing from the filtration process. The nanofibers were uniform in diameter, with an average of 25.1 nm (Stdev = 2.5 nm) and a range from 20 to 29 nm. Similarly, the height of the fibers was consistent with an average of 3.93 nm (Stdev = 0. 02 nm) and a range from 3.90 to 3.99 nm. The height uniformity can easily be seen in a 3-D rendering of height (Figure 4). Most often, the nanofibers were found in bundles, with the fibers overlapping or in close contact with one another. Phase images indicated that the fibers were much softer than the surrounding silica surface, and that the fibers had consistent shifts in phase, ~ 11.5 degree, when subtracted from the background, as indicated by the color of the fibers in Figure 5. From the phase difference between the nanofibers and the surrounding background material, it is safe to claim that there is an adhesive interaction between the tip and the nanofibers. The increased adhesion from these fibers contributes to their medicinal effects.

While there exists some evidence that the medicinal properties of Yunnan

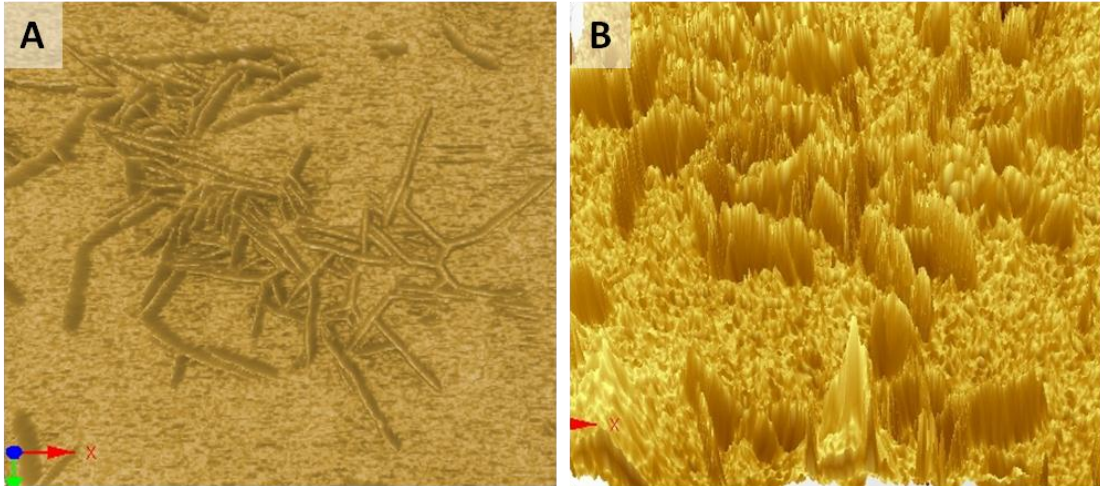


Figure 4 3-D rendering of nanofibers against the silica wafer background.

(A) Top-down view of 3-D rendering demonstrating the uniform height of the nanofibers. (B) Tilted angle of the same nanofibers demonstrating the depth of field, and height of nanofibers relative to the background.

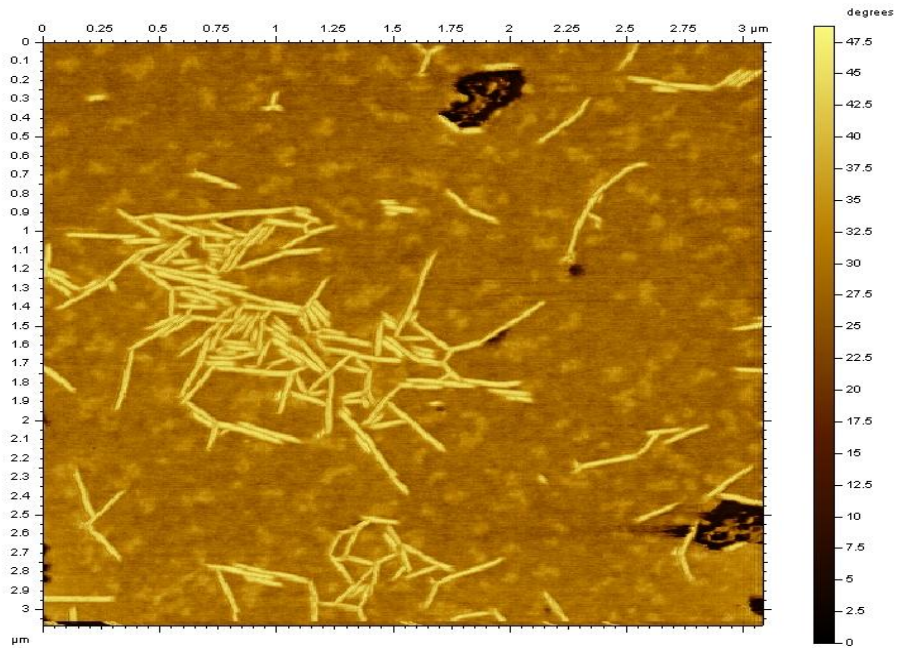


Figure 5 Phase image of nanofibers showing the difference in phase shift compared to background.

Phase can more easily show tip interactions than topography images, and can provide potential information on adhesion and hardness of a structure.

Baiyao can be related to chemical constituents isolated during the compounding process, saponins and triterpenes alone cannot completely explain the mechanism of actions of this curious drug. The elucidation of nanofibers within a solution of Yunnan Baiyao leads to the possibility that there are physical factors, in addition to chemical ones, that lead to the increased platelet aggregation and wound sealing.

It is known that nanoparticles and nanotubes play a significant role in platelet activation and that the amount of activation and subsequent beneficial or detrimental effects can be related to the composition of the nanoparticles [30-32, 43]. In a similar manner, it is believed that the nanofibers discovered in Yunnan Baiyao play a role in the activation of platelets, which may help explain some of its beneficial effects. The nanofibers are most likely carbon based on the fact of their extraction from a variety of plants, and that carbon nanotubes have been demonstrated to have the greatest effects on increasing platelet activation. Increased platelet activation by the nanofibers would lead to an increased clotting rate that would reduce bleeding, one of the most common uses of Yunnan Baiyao. Chemical components of Yunnan Baiyao have been shown to both increase, and decrease platelet activation and coagulation (Table I), and thus the presence of nanofibers would further aid in allowing rapid clot formation and the reduction of bleeding times.

Another potential benefit from the nanofibers would be to facilitate wound sealing to prevent infection. It has been well-established in the literature that

nanofibers have very strong adhesive benefits [44-46]. As in the case of the gecko, they allow the gecko to climb easily using bundles of fibers on the surface of its feet [29, 47, 48]. In addition to the adhesive properties, nanofibers have also been used as scaffolding to initiate the repair of damaged tissue. Schneider et al., found that the combination of a nanofiber scaffold with epidermal growth factor resulted in the regeneration of new skin 5 times faster than without the scaffold [49]. Furthermore, Long et al. concluded that nanofiber scaffolding was effective in wound healing of rabbits with full-thickness skin defects [50]. In this same manner, it is likely that the nanofibers found in Yunnan Baiyao act as scaffolding to initiate the repair of wounds. This scaffolding would allow wounds to repair more rapidly, substantiating the claims that Yunnan Baiyao effectively aids in sealing wounds. In effect, the nanofibers may act as an adhesive bandage that allows a wound to seal by adhesion of the skin layers. In all samples tested, it was observed that nanofibers tended to be found in clumps, and tightly associated with one another, even after being passed through the filter. In highly concentrated samples, there was too much background for the AFM to achieve a contrast that would have allowed visualization of the fibers, thus a series of dilutions was used to optimize the imaging and visualize individual nanofibers. In a concentrated form, as in the recommended doses for treatment of wounds externally (250 mg), the number of fibers would be greatly amplified over our experimental samples. This would lead to a network of nanofibers that would be able to bind to one another and form scaffolding that

may lead to increased cell growth. The true length of the fibers could not be elucidated in this study due to shearing, however fibers of several micrometers were observed in some experiments.

The discovery of consistent and uniform nanofibers in Yunnan Baiyao helps to elucidate the mechanism of action of this Chinese herbal medicine. By applying similar nanofibers to other drugs, it may be possible to increase their effectiveness, specifically in the area of wound healing and blood clotting. Recently there has been a resurgence in the study of herbal remedies for the treatment of a variety of ailments, including cancer [51]. In fact, recent studies have included Yunnan Baiyao and clinical data could dramatically increase the use of this drug [39, 52]. There are in general two possible ways for nanofiber formulation. The first is through the compounding process that these nanofibers are created from a variety of different components. The other is through small plant fibers, such as lignin, that are naturally derived from the crushed herbs. Nanoscale imaging of herbal medicines is not commonly practiced, however, AFM studies of herbal remedies may help to shed light on how some of these mysterious medicines function.

**CHAPTER III. EVALUATION OF NANOFIBRILLAR
STRUCTURE OF DIOSCOERA OPPOSITE EXTRACT
FOR CELL ATTACHMENT**

A version of this chapter was originally published by Lijin Xia, Scott C. Lenaghan, Andrew B. Wills, Yinyuan Chen and Mingjun Zhang:

Lijin Xia, Scott C. Lenaghan, Andrew B. Wills, Yinyuan Chen and Mingjun Zhang. "Evaluation of the nanofibrillar structure of Dioscorea opposite extract for cell attachment." *Colloid and Surfaces B: Biointerfaces* 88 (2011): 425-431.

Lijin Xia finished the major experiments in this study. Scott C. Lenaghan gave profession advice on this work. Andrew B. Wills helped with the atomic force microscopy analysis. Yinyun Chen helped with cell culture maintenance. Dr. Mingjun Zhang initiated and manipulated the project.

Introduction

Research in recent years has greatly advanced the understanding of cell and material surface interactions, and facilitated the development of new implantable biomaterials [53]. Biochemical signaling molecules, chemical composition, wettability, stiffness, topography and many other physical and chemical factors have been recognized as important surface characteristics for cell attachment [54-56]. Recent progress has shown that the natural cellular environment in human tissue is organized not only at the microscale, but also at the nanoscale [57]. As such, the surface topography of implantable biomaterials at the nanoscale may be important in fulfillment of their expected function, such as in the guidance of cellular behavior including cell adhesion, spreading, migration and orientation. Intense efforts in recent years have been placed on developing

nanomaterials to mimic the natural cellular environment for potential biomedical applications. The focus of these efforts are mainly on the synthetic nanomaterials, and to a less content on the naturally existing materials including traditional herbal medicines [58].

Traditional herbal medicine has been employed for centuries despite debate over the mechanisms that result in the medicinal effects. The herbal remedies usually incorporate ingredients from animals, minerals, but mainly are composed of plant extracts [59-62]. Most studies on herbal remedies have focused on identification of the chemical constituents responsible for generating the medicinal effects [63-65]. However, due to the complexity of components in these herbal remedies, the comprehensive identification of active compounds has been proven to be difficult. Recent evidence has shown that, in addition to chemical components, nanoscale morphology of the material also contribute significantly to the observed medicinal effects [66-68]. This is partially due to the increased surface to volume ratio of the nanomaterial components that leads to unique physical and mechanical properties of the materials. The unique properties are believed to contribute to many biological functions of materials that have comprehensive medicinal effects. In this study, nanomorphology was examined from the extract of *Dioscorea opposita*, which has been used in a variety of herbal remedies [63, 69].

The main herbal component of *Dioscorea opposita* is the rhizome, a starchy, mucilaginous structure that is also eaten as a raw vegetable. Although

the complete identification of chemical components from the *Dioscorea opposita* extract has not been conducted, its main component is believed to contain mucilage, polysaccharide and starch [70-73]. Mucilage, extracted from *Dioscorea opposita*, has been reported to have neuroprotection, adipocyte aquaglyceroporin modulation, and antioxidant, fungicide and amnesia amelioration activities [64, 74-78]. Different polysaccharides, including YP-1 and CYP, have been isolated and their enhancement in immune response and anti-cancer activities has been characterized in mouse models [79, 80]. In addition to the polysaccharides, other bioactive chemicals, including soluble viscous proteins, phospholipids, starch, glycoside and some small molecules, such as palmitic acid, beta-sitosterol, oleic acid, beta-sitosterol acetate, have also been isolated from *Dioscorea opposita* [65, 72, 73, 76, 81]. Although the chemical components provide necessary nutrition and physiological activities for *Dioscorea opposita*, the nano-morphology of the extract that might play a role in cellular and physiological activities has not yet been well characterized.

The nanoscale morphology of many plant and animal structures has been studied within the past decade, with many noticed amazing effects employed at this small scale [11]. Due to advancement of nanotechnology and our understanding of these nanostructures, biomimetic and bioinspired approaches have begun to be generated for potential applications in biomedical engineering, tissue engineering, and regenerative medicine [82]. To meet the stringent requirements of an implantable biomaterial, tissue engineering has relied on

mimicking the physical, chemical and mechanical properties of the natural extracellular matrix that allows cells to grow and proliferate. An ideal nanoscale scaffold for tissue engineering must be biocompatible and implemented to match the nutritional and biological need of cells involved in the formation of specific tissue types. Most materials currently studied, are synthetic or derived from bacteria, specifically bacterial cellulose. And the applications of these materials in tissue engineering draw some concerns due to the possible occurrence of unexpected side-effect. Biomacromolecules isolated from plants and animals have a significant potential to be alternatives to these synthetic materials in tissue engineering, as they are biocompatible, cost-effective, biodegradable, and possessing suitable surface chemistry and ideal mechanical properties [83-86]. And these macromolecules are at nanoscale under proper conditions. Thus, in recent years, more biologically derived nanoscale scaffolds, including collagen-based, small intestinal submucosa, decellularized xenogenic matrices, and specifically polysaccharides, have demonstrated various applications in tissue engineering [87-89]. Successful examples include cellulose and chitosan in cartilage and bone repair, and alginate in liver repair [83, 86, 90, 91].

In the present study, the extracts from *Dioscorea opposita* were investigated for their nanoscale morphology and cellular response for potential tissue engineering applications. The sticky excretion from its mucilaginous rhizome was first separated into soluble and insoluble parts, which were then examined for their formed nanostructures on the substrates. Next, these

nanostructures were evaluated for their capacity to allow different types of cells to attach and proliferate *in vitro*. Our observations indicate that a uniform nanoscale scaffold can be formed from the soluble extract, which provides an excellent platform for HeLa cell attachment and proliferation. The results from this study demonstrated the potential for this natural material to be incorporated into tissue engineering applications in the future.

Materials and Methods

Extraction of soluble and insoluble components

Dioscorea opposita was purchased from the Sunrise Supermarket, Knoxville, TN. The rhizome was first washed to remove soil and residue on the surface, and then allowed to dry. After drying, the rhizome was cut exposing the white sticky mucilage, which was squeezed and collected gently using 200 μ l pipette tips. The cutting and collection steps were repeated until 500 μ l of solution was collected. The solution was then centrifuged at 17,000 g for 2 hours, and the supernatant was transferred to a new eppendorf tube. The supernatant was centrifuged twice more at the same speed to remove insoluble components, mainly starch. After the final centrifugation, the supernatant was collected and stored at 4°C prior to analysis. To study the insoluble components, the pellets from the first centrifugation were washed three times with 20-nm-filtered water by centrifugation at 17,000 g for 10 min and the supernatant was removed. After the

final wash, the pellet was resuspended in the 20-nm-filtered water and stored at 4°C for analysis.

Atomic force microscopy imaging

Samples were prepared for imaging by placing 10 µl of soluble extract or resuspended pellet components onto a clean silicon wafer surface, then air-dried overnight at ambient temperature in a 1300 Series Class II, Type B2 Biological Safety Cabinet (Thermo Scientific, Waltham, MA). The air-dried samples were then imaged using an Agilent 6000 ILM/AFM atomic force microscope (AFM) operating in air in AC mode, as previously described [92]. All samples were examined by two independent investigators to eliminate the possibility of artifactual data and misinterpretation. Intermittent contact mode tips, Budget Sensors® Tap150AL-G with a resonant frequency of 150 kHz and a force constant of 5 N/m, were used for all imaging. Prior to scanning, a calibration grid was used to assure that the distance measurements of the Picoview® software (Agilent Technologies) were accurate. Publication quality scans were conducted at a scan speed of less than 1 ln/s with a resolution of 1024×1024 pixels.

Cell culture

HeLa (ATCC# CCL-2.1) cells were cultured following the standard culture procedure recommended by American Type Culture Collection (ATCC). Briefly, cells were incubated at 37°C in a 5% CO₂ environment in Dulbecco's Modified Eagle's Medium (DMEM) supplemented with 10% heat-inactivated fetal bovine

serum (Hyclone Laboratories, Logan, UT), and penicillin/streptomycin (MP Biomedicals, Solon, OH) at 100 U/ml. The HeLa cells were normally grown in 8-10 ml culture medium in T25 flasks (Corning Life Sciences, Lowell, MA), and were passage at 1:5 every 2-3 days with 90% confluence. On occasions where cells were required for specific studies, the HeLa cells were passaged at 1:1 dilution 24 hours before the study.

MC3T3 mouse osteoblast cells were cultured in alpha minimum essential medium (α -MEM) with 10% fetal bovine serum and 1% penicillin/streptomycin at 37°C in a 5% CO₂ environment. Cells were normally grown at 8-10 ml culture medium in T25 flasks and were passaged at 1:5 every 3-4 days with 90% confluence. When cells were required for specific studies, the cells were passaged at 1:1 dilution 24 hours prior to the study.

Substrate coating

The wells in a 24-well plate (Becton Dickinson and Company, Franklin Lakes, NJ) were first pre-coated with 100 μ l of 12% poly-2-hydroxyethyl methacrylate (polyHEMA) except 4 wells which were left untreated for comparison and designated as positive controls. After two days of evaporation, the polyHEMA-coated wells were further coated with 100 μ l of soluble extract, or resuspended insoluble components. A row of 4 polyHEMA-coated wells were not coated with either soluble or insoluble extracted components, and designated as negative controls. After air-drying for two days in a closed 1300 Series Class II, Type B2

Biological Safety Cabinet, the lid of the plate was removed, and the sample was UV sterilized for 30 minutes.

Cell attachment

HeLa or MC3T3 cells were seeded at 5×10^4 cells/cm³ onto the wells coated with the extracted soluble and insoluble components, and to the wells designated as positive and negative controls. Cells were maintained at 37°C in a 5% CO₂ environment for 12 hours, before analyzing cell attachment with an Olympus Fluoview 1000 inverted light microscope (Olympus America, Center Valley, PA). Unattached cells were removed by replacing the original media with fresh cell culture medium. The cell attachment and spreading were tracked every 12 hours.

Soluble extract and cell interactions

The HeLa or MC3T3 cells were seeded at 5×10^4 cells/cm³ onto uncoated wells in a 24-well plate. 30 µl of soluble extract was added to each well and mixed by gently shaking the plate. The cells were then incubated at 37°C in a 5% CO₂ environment, and were examined every 6 hours using an Olympus Fluoview 1000 inverted light microscope.

Biomolecules in soluble extract

In order to identify key components that may contribute to the attachment of cells to the scaffold formed by the soluble extract, it was necessary to perform several colorimetric assays to determine key components. To determine the existence and concentration of proteins in the sample, the standard Pierce® BCA

(bicinchoninic acid) protein assay (Thermo Scientific, Rockford, IL) was conducted per the manufacturer's specification [93]. This assay determines the concentration of proteins relative to a standard curve based on the change in absorbance of the dye at a wavelength of 562 nm. A similar light absorbance assay was performed to determine the existence and concentration of polysaccharide in the soluble extract using 1,9-Dimethyl-Methylene Blue (Sigma Aldrich, St. Louis, MO) at a wavelength of 525 nm [94]. Bovine serum albumin (BSA) was used to generate the standard curve in the BCA assay, while shark chondroitin sulfate (Sigma Aldrich) was used to generate a polysaccharide standard curve. In addition, polysaccharides on the soluble extract-coated surfaces were stained using Alcian Blue following a similar procedure used for identification of polysaccharides in the nanofibers of the sundew adhesive [95].

Results and Discussion

Nanofiber-based scaffold from the *Dioscorea opposita* soluble extract

The sticky excretion from the rhizome of *Dioscorea opposita* contains some starch during the collection steps. The high-speed centrifugation allows the separation of the starch from the soluble extract. After coating onto the silicon wafer surface, the surface morphology of the soluble extract was examined using AFM. As shown in Figure 6, nanofibers were visible on surfaces coated with the extract. The observed nanofibers uniformly spread across the surface and

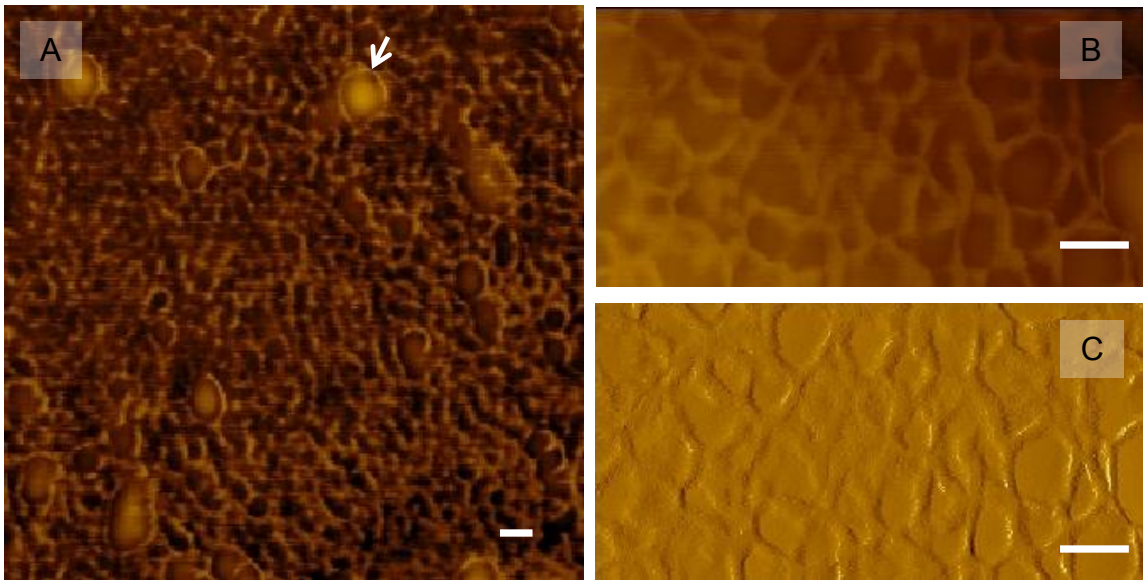


Figure 6 Morphology of soluble extract from *Dioscorea oppositifolia*.

(A) AFM topography image of the soluble extract at a scan size of 0.9x0.9 μm . (B, C) AFM topography & phase images of the soluble extract at a scan size of 0.4x0.2 μm . The arrows pointed the nanoparticles in the nanofiber network. Scale bar = 50 nm.

contained sparsely embedded nanoparticles with a size range from 20-100 nm (Figure 6A). These nanoparticles (indicated by arrow in Figure 6A) of different sizes may represent starch granules that were not completely removed after centrifugation. The nanofibers intertwined to form a porous scaffold. To examine the detail of these nanofibers a smaller area was scanned using AFM and the topography and friction images are shown in Figure 6B and 6C. From these images, it was possible to observe nanofibers with varying lengths and pore sizes. While the length of these fibers was difficult to determine, the diameter of the nanofibers was measured as ~ 10 nm, although variations in diameter existed along individual fibers. The linkages formed among the fibers might be due to branching structures that crosslinked during drying, allowing for formation of the scaffold with an average pore size of ~ 40 nm. The porosity of the scaffold provides the necessary space for diffusion of nutrients, metabolites and soluble factors for cell growth in tissue engineering applications. The porous network formed by interconnected nanofibers resembles the native extracellular matrix structure and may serve as a scaffold for initiating tissue regeneration upon cell seeding [96].

Formation of nanofibers from insoluble components

In addition to the soluble extract, the morphology of the insoluble components was also investigated. As shown in Figure 7, it was again possible to observe nanofibers from the insoluble extract. However, a detailed look at these nanofibers found that these fibers differed significantly from the nanofibers from

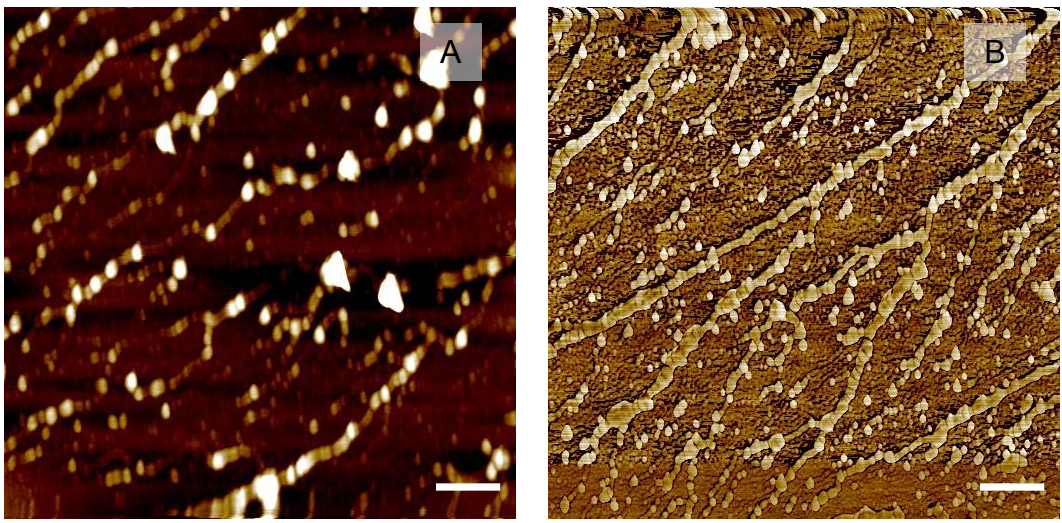


Figure 7 Morphology of nanoparticles and nanofibers from insoluble extract of *Dioscorea oppositifolia*.

(A, B) AFM topography and friction images of resuspended insoluble extract at a scan size of $4 \times 4 \mu\text{m}$. Scale bar = 500 nm.

the soluble extract shown in Figure 6 and other polysaccharide scaffolds [92]. As shown in Figure 7A and 7B, these fibers had a rough surface and very large size distribution. More importantly, these fibers were composed mainly of nanoparticles, as evidenced by the dotted appearance of most of these fibers. The alignment of these nanoparticles to fibers could be easily observed due to larger protrusions from agglomerated nanoparticles along the fibers. The mechanism used to align the nanoparticles for formation of nanofibers is not understood at this time. Two possible explanations are: 1) the nanoparticles are adhesive at nanoscale and bind to each other during the drying process in the diluted condition; or 2) the adhesive soluble components were not fully removed during the washing process. These adhesive components might help the alignment of nanoparticles into non-specific shapes.

HeLa cell attachment and growth on soluble extract formed scaffolds

Nanofiber scaffolds have been studied for applications in different aspects of tissue engineering, such as wound dressing and skin, blood vessel, neuron, bone and cartilage repair [85, 97-99]. The proper pore size and uniform nanofiber structure of the scaffolds from the soluble extract of *Dioscorea opposita* indicate their potential for tissue engineering. To determine if the *Dioscorea opposita* scaffold could support cell attachment, HeLa cells were seeded onto soluble extract-coated surfaces. As shown in Figure 8, HeLa cells were found to adhere to the scaffold-coated surfaces. Due to variations in the coating process, these cells could be seen with varying densities in different areas, as shown in Figure

8A-C. The average density of HeLa cells was 53/mm². However, in the negative control where the surface was coated with polyHEMA only, no HeLa cell attachment was observed. The arrow in Figure 8C shows an exposed polyHEMA-coated area where no HeLa cells attached, similar to the negative control samples. The appearance of an uncoated area in Figure 8C might be due to evaporation from uneven distribution of soluble extract during the coating process. Although some attached cells appeared to “ball-up” into a spherical morphology or even cluster (black arrows in Figure 8B and 8C), most cells began to extend or already spread on the surface of the scaffold. The scaffold thus appeared not only optimal for cell attachment, but also for proliferation of HeLa cells.

MC3T3 attachment and growth on soluble extract formed scaffolds

A similar study was performed to examine the capacity of the scaffold from soluble extract to support MC3T3 osteoblast attachment. Similar to the HeLa cells, the MC3T3 cells attached and grew on the scaffold surfaces. In Figure 9, the observed MC3T3 cells showed an elongated shape compared to the morphology of cells in the positive control. Stressed cells were also observed, as indicated by the black arrows in Figures 9A and 9B. However, compared to the HeLa cells, MC3T3 cells grew at a lower density, 21 cells/mm². These observations indicated that the soluble extract formed scaffolds had a lower capacity for MC3T3 cell attachment compared to HeLa cells.

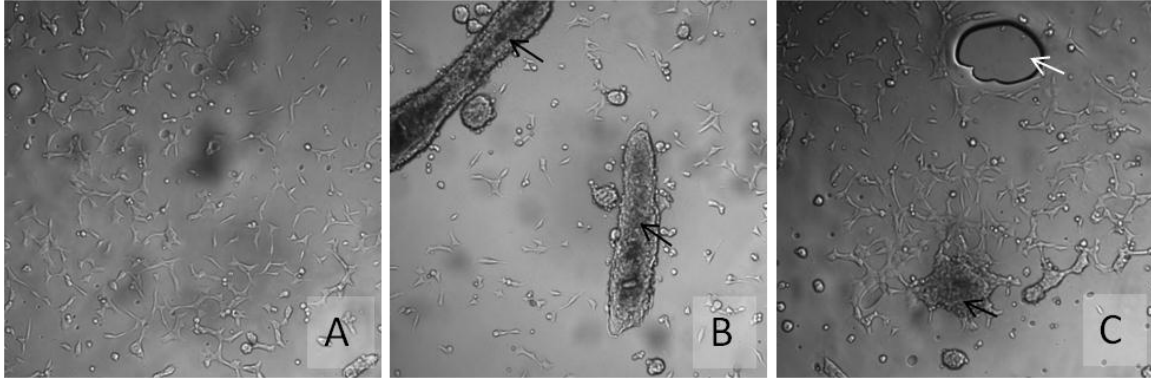


Figure 8 HeLa cell attachment and proliferation in the Dioscorea opposite soluble extract coated surface.

(A, B, C) Cells show attachment, growth and proliferation from different areas. The irregular bindle shapes with angle show cell growth and proliferation, and the dots show cell attachment prior to spreading. The black arrows in (B) and (C) show the stressed and clustered cells and white arrow in (C) show a bubble which is coated by polyHEMA but not by soluble extract.

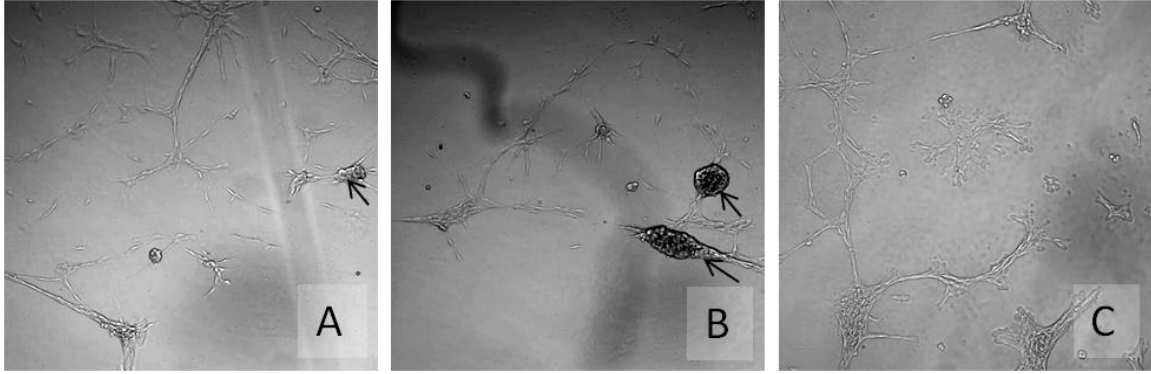


Figure 9 MC3T3 cell attachment and proliferation in the Dioscorea opposite soluble extract coated surface.

(A, B, C) Cells show attachment, growth and proliferation from different areas. The irregular bindle shapes with angle show cell growth and proliferation, and the dots show cell attachment prior to spreading. The black arrows in (A) and (B) show stressed and clustered cells.

As discovered by AFM images shown in Figure 7, the suspended insoluble components also formed nanofiber structures. But these nanofibers didn't form a network or scaffold. To examine the capacity of these nanofibers for cell attachment, similar studies were performed by seeding the HeLa or MC3T3 cells to the insoluble component-coated surfaces. No cell attachment or cell spreading was observed in these studies from either HeLa or MC3T3 cells. These observations concluded that the insoluble nanofibers did not have the capacity for cell attachment, indicating that only the soluble extract would serve as an appropriate biomaterial for medical applications.

Soluble components and cell surface interactions

The initiation of cell attachment to a scaffold usually requires the direct interactions of scaffold with cell surface molecules [100]. To determine whether there were interactions between cell surfaces and the extracted soluble components, the soluble extract were directly added to the cell culture in a 24-well plate. The cells and extracted components were examined by light microscopy during the cell growth. The soluble extract was found to form clusters in the cell culture media, possibly due to aggregation, clustering itself or interactions with constituents from cell culture medium (Figure 10). A closer look at the clusters formed in the two types of examined cells indicated a difference in clustering between the HeLa and MC3T3 cells. It was observed that most of the visible clusters stuck to the growing HeLa cells, as shown by black arrows in Figure 10C. However, no similar pattern was observed in the soluble extract

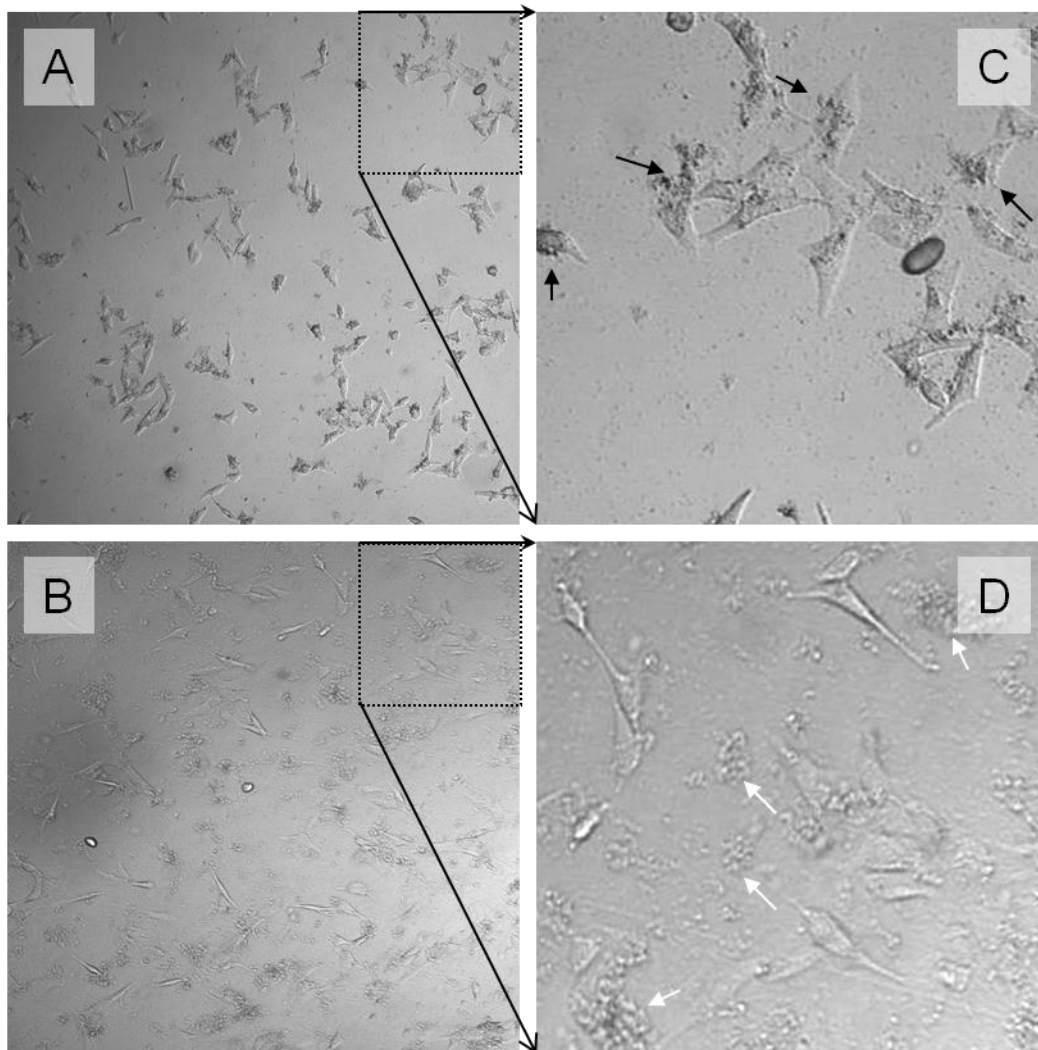


Figure 10 Interaction of soluble extract with HeLa and MC3T3 cells.

(A, C) The soluble extract in cluster or dot forms were observed mainly on the HeLa cell surface or surrounding area. (B, D) The soluble extract in cluster or dot forms was observed in random positions in related to growing MC3T3 cells.

incubated with MC3T3 cells (white arrows in Figure 10D). These observations indicated that the soluble components have a higher binding affinity to the HeLa cell surfaces, which may explain why more HeLa cells attached to the scaffold from the soluble extract compared to MC3T3 cells.

Biomolecules in soluble extract

Previous studies have found that nanofibers formed from plant adhesives were mainly composed of polysaccharides secreted from the surface of the plant [95]. To determine if a similar phenomenon occurred with the soluble extract from the Chinese yam, the coated surfaces were stained with Alcian blue. The Alcian blue staining revealed that the fibrous structure of the deposited extract contains a large amount of polysaccharide. The dimethylmethylene blue assay revealed that the soluble extract contained 198 µg/ml of polysaccharide. The protein content of the soluble extract was also examined with the BCA assay, indicating a concentration of 20.5 mg/ml in the soluble extract. The high concentration of both protein and polysaccharide confirms the rich existence of mucoprotein or proteoglycan, which might explain the “sticky” nature of the nanofiber scaffold that contributes to the ability of the cells to adhere to this scaffold, like vitronectins or other extracellular glycoprotein. Polysaccharide-containing scaffolds have shown great promise for the generation of scaffolds for tissue engineering, both synthetic and natural [101-104]. Likely mechanisms include the interaction of polysaccharide with cell adhesion molecules, such as selectin, which allows retaining of cells on the scaffold surface [105]. The existence of

selectin has been reported on HeLa cell surface but not on MC3T3 cells in previous studies, which might help explain the higher binding affinity of soluble components to the HeLa cells displayed in Figure 10 [106]. This binding will likely initiate the cell attachment and spreading on the scaffold, while the nano-network structure permits the diffusion of nutrients and facilitate further cell spreading and proliferation.

Conclusions

In this study, soluble and insoluble components were extracted from the sticky excretion of *Dioscorea opposita*, and were evaluated for the potential applications in tissue engineering. The identification of a nanofibrillar structure from the soluble extract and its ability to support cell attachment makes it a promising candidate for further investigation into tissue engineering. Previous studies have discovered that the main soluble components from the *Dioscorea opposita* were polysaccharides and adhesive proteins, the two main constituents discovered in extracellular matrix. This study further confirmed the ability of the soluble extract to mimic the extracellular matrix structurally by forming a nanofiber-based scaffold. It was found that scaffold from the soluble extract provided an excellent platform for HeLa cells attachment and proliferation. Similar results for MC3T3 were also observed, although to a lesser content. The higher binding affinity to the HeLa cell surface, but not to MC3T3 cells, might help to explain the preferential attachment and proliferation of HeLa cells on the scaffold from the soluble extract. Continued studies will focus on the underlying

mechanisms that allow this naturally occurring nanomaterial to promote cell growth, and expand onto more advanced applications for tissue engineering.

**CHAPTER IV. NANOFIBERS AND NANOPARTICLES
FROM THE INSECT-CAPTURING ADHESIVE OF THE
SUNDEW (DROSERA) FOR CELL ATTACHMENT**

A version of this chapter was originally published by Mingjun Zhang, Scott C. Lenaghan, Lijin Xia, Lixin Dong, Wei He, William R Henson, and Xudong Fan:

Mingjun Zhang, Scott C. Lenaghan, Lijin Xia, Lixin Dong, Wei He, William R. Henson, and Xudong Fan. “Nanofibers and nanoparticles from the insect-capturing adhesive of the sundew (*Drosera*) for cell attachment.” *Journal of Nanobiotechnology* 8 (2010): 20

Dr. Mingjun Zhang initiated, manipulated and supported the whole project including the cooperation with the external resources. Lijin Xia identified the nanoparticle and nanofiber, the major part of the work, and provided the materials for external cooperation. Scott C. Lenaghan provided professional advice of the project and finished cell study part of the project. William R. Henson and Xudong Fan helped with part of experiments. Dr. Lixin Dong and Dr. Wei He gave profession advice on this study.

Introduction

For centuries, carnivorous plants have fascinated researchers and stimulated the minds of many scholars, including Charles Darwin. One of the carnivorous plants that interested Darwin was the sundew (*Drosera*). The sundew relies on complex trapping mechanisms to capture insects, which provide increased nitrogen levels that give it a competitive advantage over non-carnivorous plants [107]. Each of the sundew tentacles secretes a small “bubble” of adhesive that fully covers its head (Figure 11). When an insect becomes stuck to the adhesive

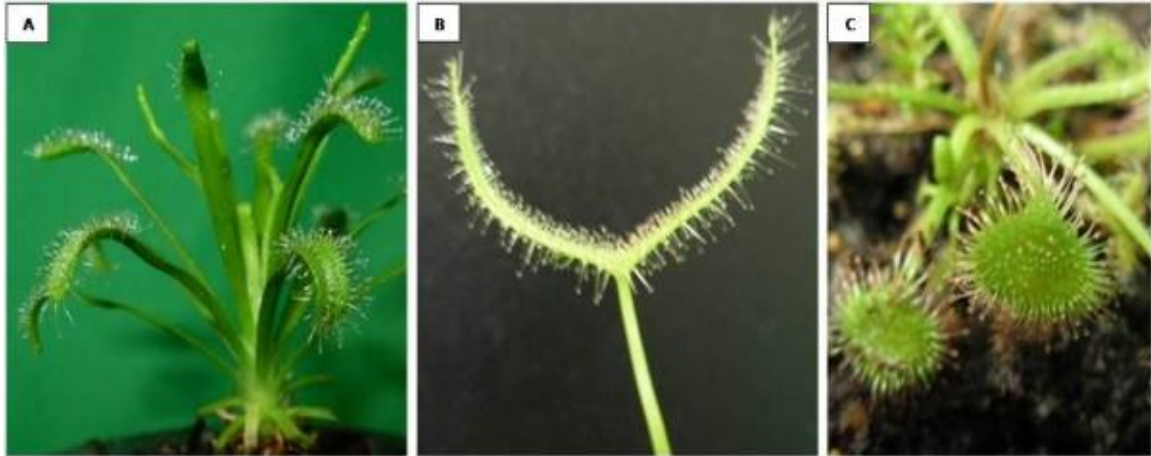


Figure 11 Pictures of three species of the sundew.

(A) *D. capensis*. (B) *D. binata*. (C) *D. spatulata*. The leaves of each species are covered by small tentacles that generate the adhesive. This adhesive is secreted externally, allowing for easy collection.

bubble, the movement of the insect generates a series of action potentials along with the tentacles, which trigger the tentacles to bend inward [108, 109]. The bending brings the insect into a closer contact with other tentacles, including shorter specialized tentacles that further triggers the leaf to secrete digestive enzymes [110-115]. Digestion serves as a signal to release hormones that allow the leaf blade to curl tightly around the prey for complete digestion and absorption of nutrients [116]. This complex trapping mechanism uses the unique properties of the adhesive for insect capturing.

One of the unique properties of the sundew adhesive is its highly elastic nature that allows it to be drawn into threads up to one meter in length [117]. Early studies confirmed that the chemical structure of the adhesive was an acid polysaccharide containing various concentrations of sugars and acids, depending on the species [117, 118]. Isolation of *D. capensis* adhesive through gel filtration, cellulose acetate filtration, ion-exchange chromatography, and ultracentrifugation yielded one macromolecule with a molecular weight of 2×10^6 Daltons [117]. It was discovered that the adhesive is composed of xylose, mannose, galactose, glucuronic acid, and ester sulfate in the ratio of 1:6:6:6:1 [117]. In other species, the acid polysaccharide was found to have different ratios of monosaccharides. *D. binata* was reported to contain arabinose, xylose, galactose, mannose, and glucuronic acid in a ratio of 8:1:10:18:17 [118]. Further analysis also found that these polysaccharides consisted of an abundance of metal cations, including 22 mM Ca^{++} , 19 mM Mg^{++} , 0.9 mM K^+ , and 0.2 mM Na^+ in *D. capensis*. The *D.*

capensis adhesive was composed of water (96%) and acid polysaccharide (4%) [117]. The ratio of polysaccharide to water has proven to be crucial in the formation of the unique elastic properties of the adhesive, as seen with other polymers [119-123]. Due to the difference in chemical composition, varying material properties were expected for different sundew species. Environmental factors and prey availability could have imparted selection pressure that influenced the development of the adhesives over the course of evolution.

In addition to chemical composition, nanoscale morphology also contributes to the physical properties of materials. Preliminary studies on structural properties of polysaccharide-based adhesives have been conducted [124, 125]. However, the relationship of the nanoscale morphology to the physical properties of adhesives remains largely unexplored. In this study, a discovery of the nanofiber and nanoparticle-based network from the sundew adhesive was reported, and the potential of its applications was addressed.

Materials and Methods

Plants

The sundew species (*D. binata*, *D. capensis*, and *D. spatulata*) were purchased from the Carnivorous Plant Nursery (Derwood, MD) and maintained in mineral depleted soil with distilled water. The sundew are sensitive to high concentrations of minerals, and thus it was necessary to ensure that tap water was not given to the plants. The plants were exposed to direct sunlight for 12 hour periods, and

maintained at a constant temperature of 21°C. After a period of one week, all plants began to produce adhesive on the tentacle heads. It should be noted that there is no variation in the chemical composition of the adhesive from tentacle to tentacle within a species [117, 118].

Sample preparation

As shown in Figure 11, a small amount of adhesive forms on the head of each tentacle on the leaf surface. To coat a surface with this adhesive, the sample (silicon wafer, glass coverslip, and mica) was held with sterile forceps and gently brushed against the tentacle heads, allowing the adhesive to be transferred to the sample. Using this method, a different pattern of coating was achieved with each treatment. Due to the non-uniformity of the coating method, over six replicates for each species and substrate were examined. After applying the adhesive to the substrate, the samples were allowed to dry for 24 hours under a bio-safety cabinet.

Due to the large surface area of the 25 mm² coverslips, for cell attachment studies, the coverslips were cut to 5 mm² with a diamond etched pen. These smaller coverslips were then cleaned by sonication in acetone, ethanol and deionized water. Using these smaller coverslips, it was possible to more easily coat the entire surface area. To ensure that the coating covered the entire surface, an Alcian Blue pH 2.5 Periodic Acid Schiff Stain was applied to all coated samples per the manufacturer's instructions. With this staining procedure, acid polysaccharide stains bright blue and neutral muco-substances stain pink.

Upon completion of staining, the samples were imaged using an Olympus Fluoview 1000 microscope to visualize the stained adhesive.

In addition to the stained experimental samples, control samples were prepared for the cell attachment experiments using uncoated coverslips, and 0.1% poly-L-lysine (Electron Microscopy Sciences, Hatfield, PA) coated coverslips. PC12 and primary nerve cells have been shown to strongly attach to poly-L-lysine coated surfaces, but not to bare glass, so these uncoated and poly-L-lysine coated samples served as positive and negative controls. After the coverslips were coated with the adhesive, the samples were UV sterilized while submerged in Hank's Balanced Salt Solution, Formula III (Electron Microscopy Sciences) for 15 minutes in a biosafety cabinet. Upon sterilization, the samples were seeded with PC12 cells in F12-K medium supplemented with 15% horse serum and 2.5% fetal bovine serum at a density of 5×10^4 cells/cm². The cells were then incubated on the samples for 24 hours in a 37°C incubator with 5% CO₂ to allow for attachment. After 24 hours, the samples were gently washed with sterile Milonig's Phosphate Buffer (Electron Microscopy Sciences®) warmed to 37°C. This prevented detachment due to temperature induced stress. Cells were then stained for 30 minutes with a live/dead viability dye containing calcein AM and ethidium homodimer-1 from Invitrogen (catalog number #L3224), in which live cells stained green and dead cells stained red. The samples were then washed and visualized using the fluorescent microscopy. Four fields of view under (0.0391 mm²) were used to determine the number of attached cells on

each sample. The number of viable cells was determined by counting 100 cells at random and scoring as either alive or dead using the viability dye.

Atomic force microscopy

AFM imaging was conducted using both an Agilent 5500 AFM and an Agilent 6000 ILM/AFM. The purpose of using both systems was to control for potential artifacts, and to allow for microscopic imaging of the samples to determine the targeted scanning areas. In addition, all samples were examined by two independent investigators who prepared their samples separately to further eliminate the possibility of artifactual data. All imaging for both systems was conducted in air in AC mode. Both systems were equipped with intermittent contact mode tips, Budget Sensors® Tap150AL-G, with aluminum reflex coating. The tips had a resonant frequency of 150 kHz and a force constant of 5 N/m. Due to tip variation, manual sweeps were conducted on all tips prior to scanning to determine the actual frequency of the tip. Prior to scanning, a calibration grid was used to assure that the distance measurements of the Picoview® software were accurate. Publication quality scans were conducted at a scan speed of less than 1 ln/s and a resolution of 1024x1024 pixels.

Transmission electron microscopy

Transmission electron microscopy (TEM) imaging and energy-dispersive X-ray spectroscopy (EDS) were conducted using a JEOL 2200 FS TEM with attached EDS at the Advanced Microscopy Center of Michigan State University. Copper

grids were coated with ultra thin carbon films. By using the thin film copper grids, the sundew could be deposited on the film, instead of falling through the mesh of the grid. Grids were then coated with the sundew adhesive in the same manner using the technique described earlier. Briefly, the copper grids were grasped using sharp electron microscopic forceps and gently brushed against the tentacles of the sundew. After coating with the adhesive, the samples were dried overnight for subsequent analysis.

Results and Discussion

Nanostructure of the sundew adhesives

The first stage of this study focused on determining the nanoscale structure of the dried adhesive on a variety of substrates. By determining the nanostructure of the adhesive, the potential uses for this material can then be evaluated. Three sundew species, *D. binata*, *D. capensis*, and *D. spatulata*, were chosen for this study. Adhesive from the tentacles from the three species were streaked onto silicon wafers, mica, and glass coverslips. After the samples were allowed to dry overnight in a biosafety cabinet, the samples were scanned using AFM.

Based on the AFM analysis, it was determined that a complex network of nanofibers of varying lengths and thicknesses were deposited on the coated substrates, as shown in Figure 12. A network of nanofibers was formed from the deposition of the adhesive in all examined species (Figure 12A-C). The networks had gaps ranging from 500 nm to several microns between the nanofibers, which

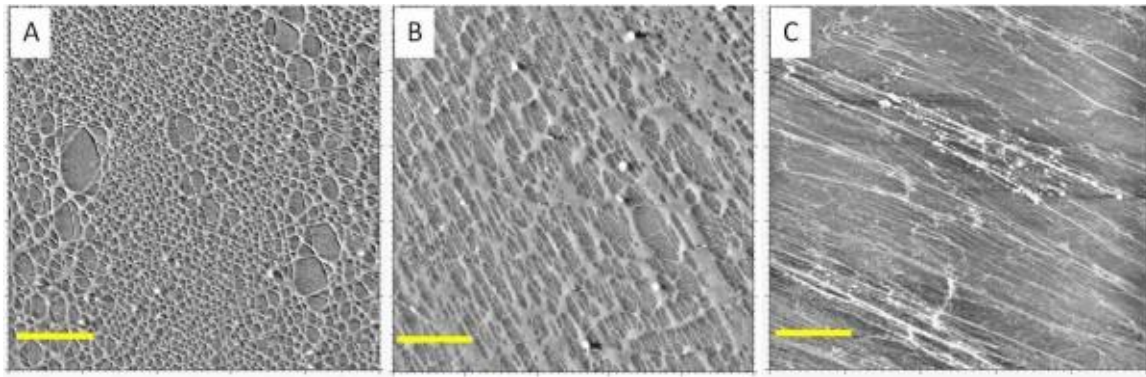


Figure 12 AFM images of the sundew adhesive for three sundew species.

AFM scans of different species of sundew, *D. binata* (A), *D. capensis* (B), and *D. spatulata* (C). All scans are 10×10 μm. Scale bar = 2 μm.

provided an ideal morphology for the attachment of cells. The adhesive from all species was capable of forming the observed networks on all of the tested substrates, despite their varying surface properties. From this evidence, it was determined that a complex network of nanofibers was created by streaking the adhesive from all tested sundew species onto a variety of surfaces.

Polysaccharides in the nanostructured sundew adhesives

In order to determine if the network observed by AFM was, in fact, due to the polysaccharide component of the adhesive, a staining procedure was used to correlate the stained polysaccharide to the imaged network of nanofibers. The surface of tentacle streaked coverslips was stained with Alcian blue, pH 2.5, and Schiff reagent. This staining procedure stains acid polysaccharides blue, and neutral polysaccharides pink [126]. Using the Picoview® software package, the images obtained from a large scan of the network structure was over-laid onto a light micrograph. Using this technique, it was confirmed that the network of nanofibers from the AFM scans matched the pattern of staining for the acid polysaccharide (Figure 13). From this experiment, it was clear that the networks observed in the AFM scans were the dried polysaccharide from the streaked tentacles. Using this technique, it was not possible to compare individual nanofibers, since these fibers cannot be imaged by light microscopy. However, bundled fibers were clearly correlated with the polysaccharide stain. In addition to nanofibers, nanoparticles were also observed from the AFM images.

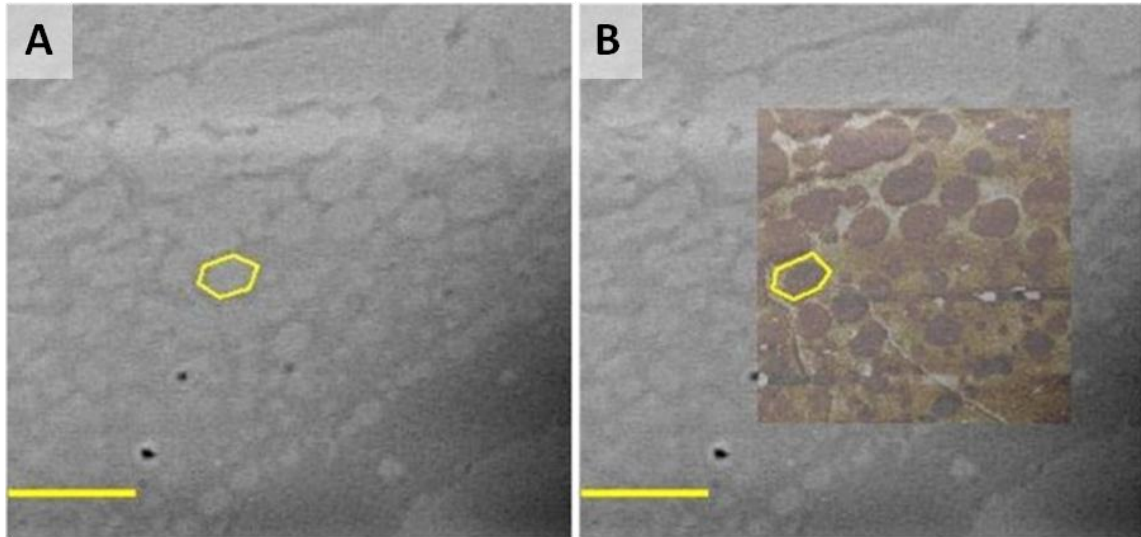


Figure 13 AFM overlay of Alcian Blue stained sundew adhesive.

(A) An Alcian blue stained sample showing the pattern of the deposited sundew adhesive. (B) An AFM scan overlaid onto the stained micrograph. An area of interest has been outlined to demonstrate the overlap between the Alcian blue stain and the topography image from the AFM. Scale bar = 20 μm .

Nanoparticles in the fibrous adhesives

Smaller scan regions revealed that the nanofibers were composed of individual nanoparticles as shown in Figure 14. Nanoparticles were found in close contact with one another and were associated with the polysaccharide nanofibers. Vertical cross-sections through individual nanofibers confirmed that the nanoparticles were of a uniform size and shape with diameters in the range of 50-70 nm. In other natural systems, such as ivy, mussels, and barnacles, nanoparticles have proven to be an important component of adhesives [18, 127]. It is believed that these nanoparticles are a crucial component to the generation of the material properties observed in these adhesives. The discovery of nanoparticles within the sundew adhesive provides another example of the conserved approach used by natural systems to create nanocomposite adhesives.

Chemical characterization of metal components in adhesives

In order to determine if the nanoparticles were metallic, the adhesive from each of the sundew species was further analyzed using high resolution transmission electron microscopy (HRTEM) (JEOL 2200FS, 200kV). If the nanoparticles were metallic, then when imaged by HRTEM, chains of nanoparticles would be observed that would correlate with the observed fibers seen by AFM. By using HRTEM, the polysaccharide would not be visualized, along with any organic nanoparticles because they are not electron dense and would be broken down by the high energy beam. After imaging of multiple samples it could be concluded

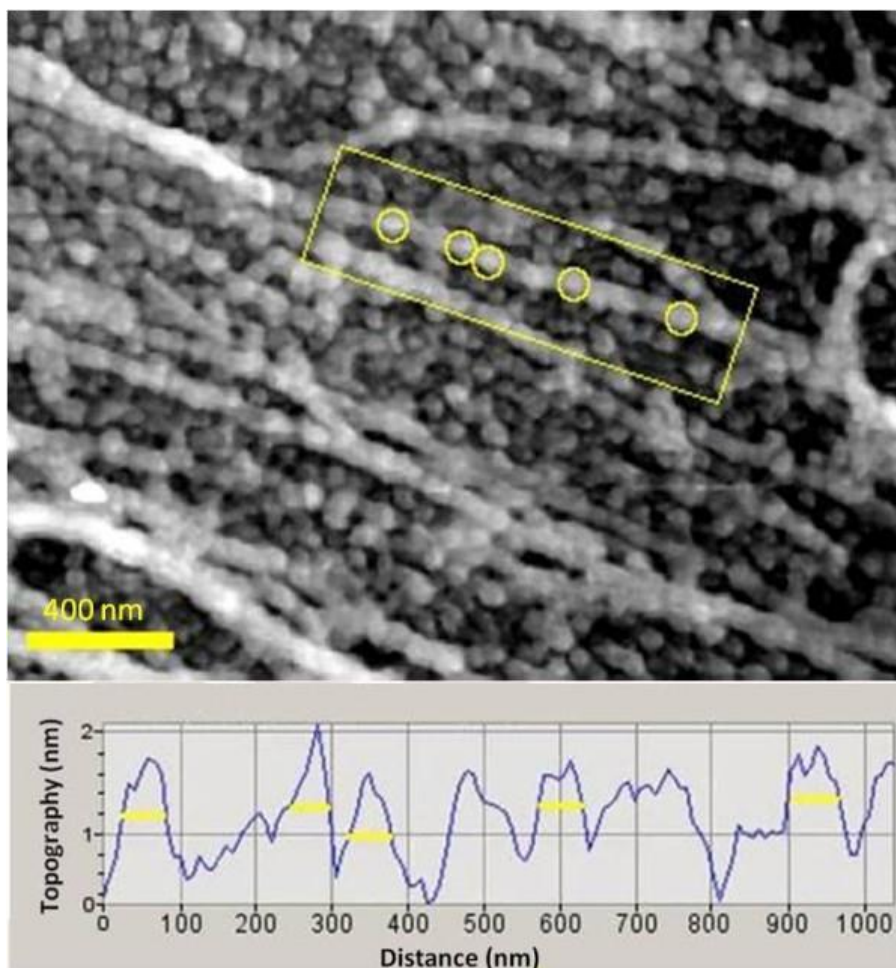


Figure 14 Nanoparticle size characterization.

Top, an AFM image of the sun dew adhesive. Individual nanoparticles corresponding to peaks observed in the vertical cross-section are identified by yellow circles. Bottom, a vertical cross-section through the nanofiber outlined by the yellow box at the top image. Diameters of the nanoparticles were calculated based on the diameter of the observed peaks using the Picoview® software package. Broader peaks indicate a group of nanoparticles that could not be individually resolved with AFM. All nanoparticles were in the range of 50-70 nm.

that the nanoparticles observed from the AFM imaging experiments were organic and not metallic. There were no chains of nanoparticles similar to what was observed in the AFM scans. Diffuse crystalline nanoparticles were observed in several of the samples, but these nanoparticles were in a low abundance and tended to agglomerate (Figure 15). Figure 15A-C shows HRTEM images of solid nanoparticles, where the quasi-single crystalline structures of the nanoparticles can be clearly identified. Figure 15A shows several nanoparticles in the range of 25-44 nm from *D. spatulata*. The size range of these particles was below that observed for the nanoparticles imaged by AFM, 50-70 nm. By examining a single nanoparticle at high magnification, it was possible to observe the crystalline structure of the nanoparticle (Figure 15C). Since no staining was conducted on the specimen, the crystal structures observed from the nanoparticles were believed to be from the secreted adhesive. Each sample was prepared and analyzed in triplicate to rule out the possibility of environmental contamination. After identifying these diffuse crystalline nanoparticles on the grids, the next step is to determine the chemical components of these nanoparticles, in order to determine their function in the adhesive. To achieve this goal, EDS, a technique to determine the chemical component of samples in electron microscopy has been applied [128-130]. Analysis revealed mainly Ca and Cl in relatively high abundance from the solid crystalline nanoparticles. The solid nanoparticles were likely the result of calcium chloride, a common salt, excreted by the sundew into the adhesive. For comparison, an EDS spectrum of a region that had no

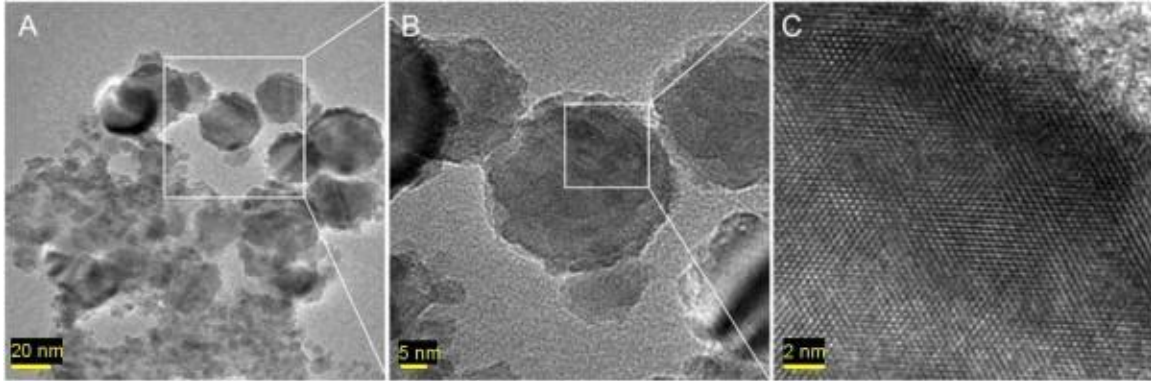


Figure 15 TEM images showing the crystalline structure of the nanoparticles.

(A) Agglomerations of nanoparticles with typical diameters around 35 nm (25 to 44 nm). (B) The particle in the center of the image was 38 nm in diameter. (C) Higher magnification demonstrating the crystalline structure of the previous nanoparticle.

nanoparticles present was obtained as shown in Figure 16. Chemical components of this region included C, Cu, and a small amount of O and Si, where Cu is from the grid, C is mainly from the carbon film on the grid, while O and Si are from the dried solution. EDS of the crystalline nanoparticles revealed mainly Ca, Mg, and Cl, which could be indicative of biological salts present in the adhesive (Figure 16).

From earlier studies on the isolation of the sundew polysaccharides, it was known that Ca, Mg, and Cl could be isolated from the adhesive in millimolar concentrations [117]. Our findings through HRTEM analysis revealed similar results through identification of crystalline nanoparticles that correlated to Ca and Mg salts. The concentration of salts present within each adhesive is crucial to the cross-linking potential of the polysaccharides, and contributes to the unique material properties.

Mechanical properties of sundew adhesives

After determining the basic structural components of the adhesive, it was necessary to determine the material properties of the adhesive. The first material property tested was the elasticity of the liquid adhesive. An AFM was employed in acoustic mode (AC) with a stop at 85% to land the tip of the cantilever on the surface of the adhesive without indenting into the adhesive. Once on the surface, force spectroscopy was employed to gently indent into the liquid adhesive in nanometer increments. After indenting less than 20 nm into the adhesive, the cantilever tip was unable to withdraw from the adhesive, due to a limited vertical

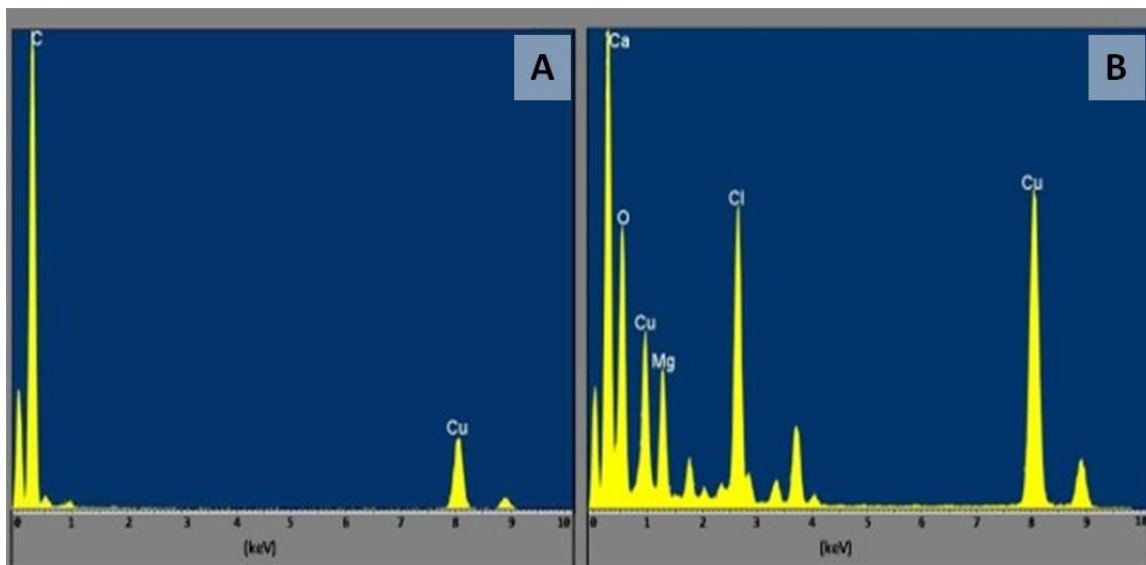


Figure 16 EDS spectra of control and nanoparticle samples.

(A) EDS spectrum of a control region with no nanoparticles. Chemical components include C, Cu, and small amounts of O and Si. Both Cu and C are from the grid and grid coating respectively. (B) EDS spectrum of a nanoparticle. Chemical components include Ca, Mg, O, and Cl. The presence of high amounts of Ca, Mg, and Cl, along with the crystalline structure of the nanoparticles indicates that the nanoparticles are the results of salts in the adhesive.

withdraw distance of 3 μm . As shown in Figure 17A-B, the cantilever had to be manually moved in the horizontal direction to break the cantilever-adhesive interaction. In fact, the adhesive was stretched 246 μm before breaking off from the tip. Considering that the contact area between the tip and the adhesive was less than 78.5 nm^2 , the elasticity of the sundew adhesive is quite large. Since the maximum vertical withdraw distance setting for the AFM used in this study was only 3 μm , it was not possible to generate force curves from the fresh liquid adhesive due to its high elasticity. Therefore, the elastic properties of the dried adhesive applied to a surface were investigated.

To investigate whether the elastic properties were maintained from the liquid to the dried adhesive, force versus distance curves were generated on the dried adhesive. Since the adhesive was completely dried before conducting the AFM studies, there was no adhesive force observed from the network of nanofibers when compared to the bare silicon surface. However, as seen in Figures 17C-D, there was a significant increase in extension length. The extension from the dried adhesive was 320.6 nm, while the extension from the bare silicon surface was less than 49.2 nm. Similarly, the adhesive showed significant deformation compared to the bare silicon wafer. It is important to point out that the AFM experiments indicated that the dried adhesive adhered to the silicon wafer, and could not be removed using sharp probes in contact mode with fast scanning speeds ($> 3 \text{ ln/s}$) and a negative set point. It is believed that a curing process takes place during drying that forms a strong bond between the

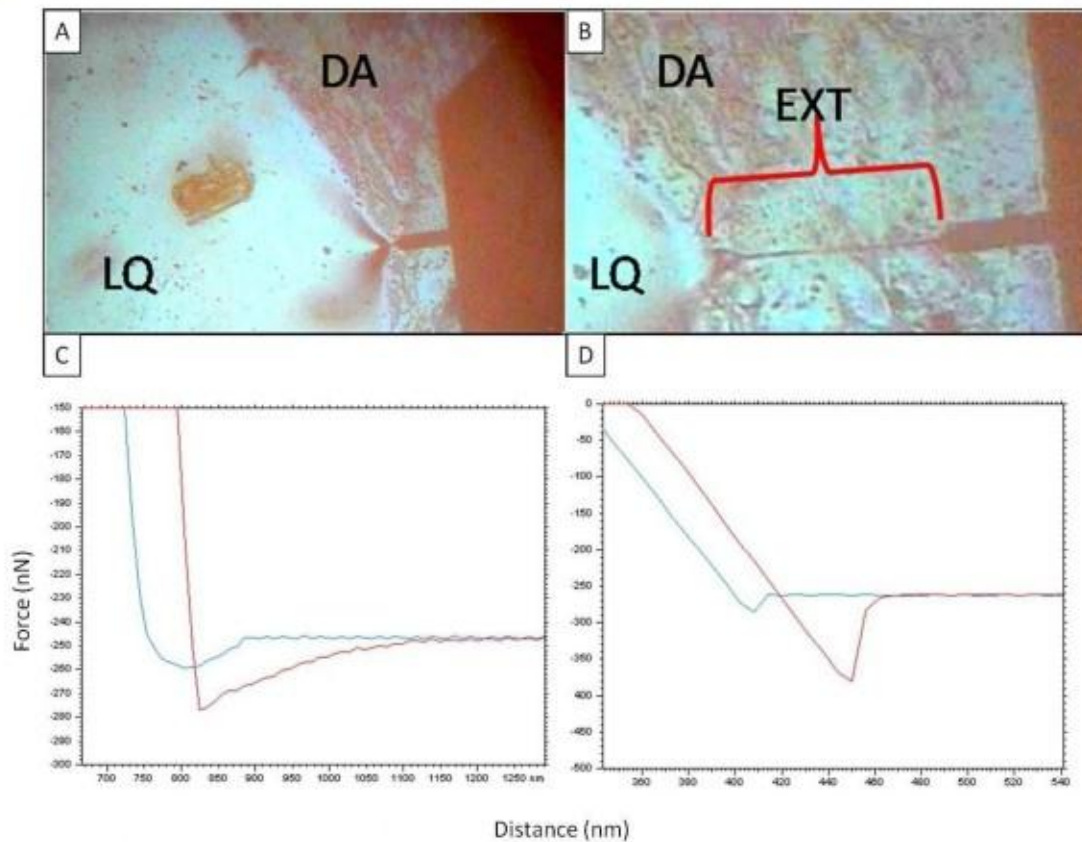


Figure 17 Measurements of extension from the liquid and dried sundew adhesives.

(A) Attachment of the cantilever to the surface of the liquid adhesive. (B) Horizontal extension of the liquid adhesive achieved by manually moving the cantilever in the X-direction with the stage controls. (C) Force curve generated on a bare silicon wafer with an extension of 49.2 nm. In both force curves, the blue line is the approach curve, while the red line is the retraction curve. (D) Force curve from the sundew scaffold shows the extension length of 320.6 nm.

adhesive and the substrate surface. This phenomenon is common for many epoxies, glues, and adhesives, where drying or chemical modification of a liquid adhesive often leads to the formation of tight bonding between the dried adhesive and the contact surface [131-135].

Neuron cell response to the nanostructured sundew adhesives

The stability of the dried adhesive on the surface, combined with the non-toxic components of the adhesive (salts, polysaccharide, and organic nanoparticles), and the porous network structure of the nanofibers, led to the hypothesis that the network could be used for applications in tissue engineering and wound healing. To validate this hypothesis, it was essential to demonstrate that the sundew network was capable of supporting cell growth. To test this ability, PC12 cells were chosen as a model system for nerve cell growth. PC12 cells were derived from a pheochromocytoma of the rat adrenal medulla [136], and are typically used as a model system for nerve cell growth and differentiation [137-139]. Three treatments were tested to determine if the network of nanofibers was capable of supporting cell attachment. Since PC12 cells do not attach to bare glass, this sample was used as a negative control. A positive poly-L-lysine coated control was used to determine the maximum number of cells that could attach on an ideal substrate. The third sample was a sundew adhesive coated glass coverslip, stained with Alcian Blue to visualize the pattern of staining. Viability was determined by using a calcein/ethidium bromide live/dead assay and all samples were imaged using an Olympus Fluoview 1000 confocal microscope.

All experimental studies consistently confirmed that the negative control had an average of 6 ± 1.3 cells attached per field of view, which was much less than the poly-L-lysine coated control that had 66 ± 4 cells attached per field of view. The sundew adhesive coated sample had 49 ± 6 cells attached per field, significantly more than the untreated control (Figure 18). Student's *t* test conducted on the data showed a significant difference between all samples with *p* values < 0.01 . Calculating the number of attached cells per mm^2 yielded 147 cells/ mm^2 for the negative control, 1681 cells/ mm^2 for the positive control, and 1253 cells/ mm^2 for the sundew adhesive coated surface. Due to the non-uniformity in the coating of the sundew samples, there was not as much surface area available for attachment compared to the positive control. This could lead to a bias in number of attached cells counted between these two samples. Little difference was observed, however, in the viability of the cells that attached in all samples. 92% of attached cells were viable in the negative control with 100% and 98% viable in the positive control and sundew adhesive coated sample respectively. For all samples, the majority of cells displayed a round morphology and similar size. Without the addition of nerve growth factor, more cells appeared to take on a polar shape in the positive control and the sundew adhesive coated surface, whereas no polar cells were observed in the negative control. As demonstrated in the Alcian Blue samples, PC12 cells attached to the sundew adhesive coated surface and were most tightly associated with the stained scaffold (Figure 18C-D). The cells attached to the sundew adhesive coated

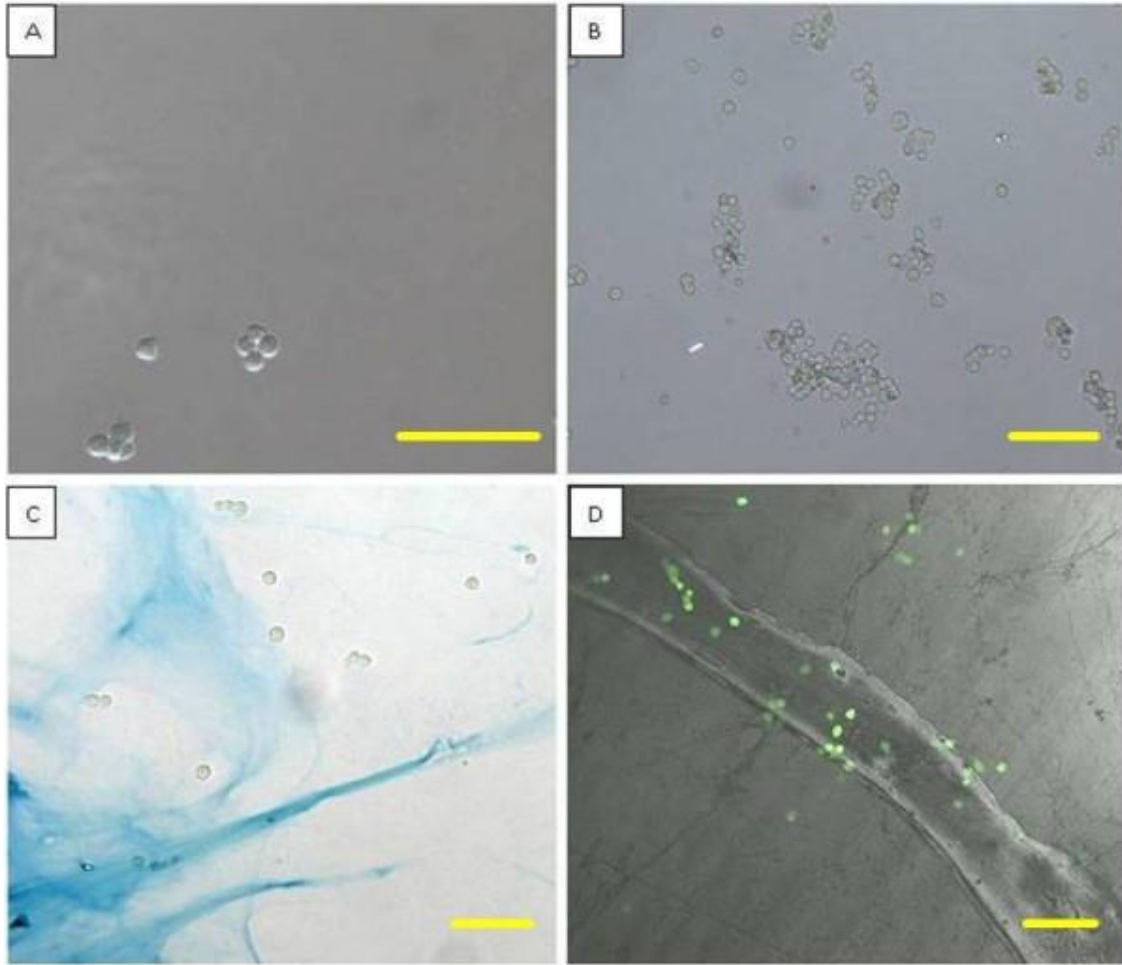


Figure 18 Light and confocal micrographs of PC12 cells attached to various substrate surfaces.

(A) Negative control sample with PC12 cells loosely attached to a bare glass surface. (B) Positive poly-L-lysine coated glass surface, with numerous attached PC12 cells. (C) Light micrograph showing PC12 cells attached to a glass coverslip coated with sundew adhesive. (D) Confocal micrograph displaying a thick area of sundew adhesive, and the thinner networks branching off from the thickly coated area. Scale bar = 25 μm .

surface were subjected to vigorous rinsing to attempt to dislodge the cells, but the cells remained attached through this process indicating a stable attachment. The results from these experiments demonstrated the potential for the sundew adhesive to be used for cell attachment in the field of tissue engineering. Based on the images obtained from these experiments, it appears that the PC12 cells favored areas with thinner coatings of the scaffold, as confirmed by both AFM imaging and the staining pattern of Alcian Blue coated surfaces. The cells generally attached to areas where the Alcian Blue staining was barely visible, which corresponded to thin layers (< 80 nm) of the nanonetwork. In the same manner, by being able to deposit a uniform pattern of coating, it may be possible to direct the growth of neurites into differentiated neurons. In essence, this study has demonstrated the potential for a novel material identified from nature to be used in the complex field of tissue engineering.

Conclusions

Through this study, the nanoscale structure of the adhesive generated from the sundew was systematically examined, and the potential of this material to be used for tissue engineering was evaluated. It was determined that the adhesive is a nanocomposite composed of water, nanoparticles, polysaccharide, and salts. This nanocomposite was observed in three species of sundew, and was shown to form a network of nanofibers independent of the surface. When dried, this adhesive serves as a suitable substrate to promote the attachment of PC12 neuron-like cells, and may be used for a variety of other cell types. Further study

into the role of the nanoparticles within the nanocomposite will lead to a better understanding of how nanoparticles can be used in adhesives. Experimentally, nanoparticles have been shown to help increase adhesion of epoxy adhesives [140]. The presence of nanoparticles in the sundew adhesive may increase surface contact and generate larger force for initial binding to insects. Another possibility is that the nanoparticles may provide a mechanical support that allows the liquid polysaccharide to stretch beyond what has previously been observed. This could explain the high elasticity observed in the liquid adhesive. Moreover, the potential uses of composite materials from biological organisms show promises for a wide variety of applications [140]. A sundew adhesive inspired biomaterial can be proposed for a wide range of biomedical applications. In addition to tissue engineering, it may be used for biological treatment of wounds, regenerative medicine, or helping enhance synthetic adhesives. Further studies will be extended to evaluate the additional potential for this material to be used in biomedical applications.

**CHAPTER V. NATURALLY OCCURRING
NANOPARTICLES FROM ENGLISH IVY: AN
ALTERNATIVE TO METAL-BASED NANOPARTICLES
FOR UV PROTECTION**

A version of this chapter was originally published by Lijin Xia, Scott C. Lenaghan, Mingjun Zhang, Zhili Zhang and Quanshui Li:

Lijin Xia, Scott C. Lenaghan, Mingjun Zhang, Zhili Zhang and Quanshui Li. “Naturally occurring nanoparticles from English ivy: an alternative to metal-based nanoparticles for UV protection.” *Journal of Nanobiotechnology* 8 (2010): 12.

Dr. Mingjun Zhang initiated, manipulated and supported the whole project. Lijin Xia performed the major part of the work. Scott C. Lenaghan provided professional advice of the project and finished digestion part of the study. Zhili Zhang provided professional advice on the project. Quanshui Li provided ultraviolet absorbance analysis.

Introduction

Ultraviolet (UV) radiation is highly energetic electromagnetic radiation from light waves below that of the visible light spectrum. The wavelengths for UV radiation range from 100-400 nm, including UV-A (315-400 nm), UV-B (280-315 nm), and UV-C (100-280 nm) [141]. While the earth’s ozone layer blocks 98.7% of UV radiation from penetrating through the atmosphere, a small percentage of UV, comprising UV-A and some UV-B, can still reach the planet, which can cause harmful effects to humans [142]. UV-C does not typically reach the surface of the planet, but due to its ability to cause DNA damage it is often used as a model for UV study in the laboratory. Depending on the time of exposure to sunlight, the harmful UV-A/UV-B effects include immediate distresses like blistering sunburns,

and long term problems like skin cancer, melanoma, cataracts, and immune suppression [143, 144]. The underlying mechanism for UV-A damage involves oxidative stress and protein denaturation, while short wavelength UV-B radiation causes predominantly DNA damage in the form of pyrimidine dimers and 6,4-photoproducts [145]. UV radiation induced DNA mutation is one of the leading causes of skin cancer, with more than one million cases diagnosed annually resulting in 11,590 deaths in the U.S. [146].

The demand for skin protection agents against the harmful influence of UV solar radiation has become increasingly important in light of the depletion of the ozone layer [147, 148]. Sunscreens, which work by combining organic and inorganic ingredients to reflect, scatter or absorb UV radiation, provide significant protection against the damage from solar UV. Early sunscreens developed with inorganic UV filters, such as titanium dioxide (TiO_2) and zinc oxide (ZnO) particles, were often opaque giving the skin a white tinge, which made them unappealing to consumers [149]. With enhanced UV protection and low opacity, nanosize metal oxide particles have been introduced into cosmetics products in recent years and thousands of tons of nanomaterials are currently applied onto the faces and hands of hundreds of millions of people every year [150]. With increased popularity, the safety of these metal-based nanoparticles and potential toxicity is under significant debate. Many studies indicated that when applied to skin for less than 8 hours, inorganic nanoparticle filters do not penetrate through the stratum corneum (SC) layer of the skin [151-154]. However, these studies

typically examine the effects of nanoparticles greater than 20 nm, and always use healthy skin samples. Studies evaluating the penetration of ultrafine nanoparticles found that TiO₂, maghemite, and iron nanoparticles less than 15 nm are capable of penetrating through the SC [155, 156]. Other studies have also observed penetration of 4 nm and 60 nm TiO₂ particles through healthy skin in hairless mice after prolonged exposure from 30-60 days [157]. This penetration leads to increased aging of skin, pathological effects in the liver, and particle accumulation in the brain. Studies like these have raised significant concerns about the prolonged use of these metal oxide nanoparticles for cosmetic applications which lead to investigation of alternative organic filters.

The properties of materials at the nanoscale differ significantly from those at a larger scale, and safety claims by cosmetics manufacturers based on their bulk properties pose great risk without proper federal regulation of their applications [158]. When decreasing size to the nanoscale, materials alter many of their physical and chemical properties, including but not limited to color, solubility, material strength, electrical conductivity, magnetic behavior, mobility (within the environment and within the human body), chemical and biological activities [159]. The increased surface to volume ratio also enhances chemical activity, which can result in the increased production of reactive oxygen species (ROS) [160]. ROS production, which has been found in metal oxide nanoparticles, carbon nanotubes, and fullerenes, is the leading force of oxidative stress, inflammation, and consequent damage to DNA, proteins and membranes

[160]. Further concern for these nanomaterials in applications is their photoactivity when exposed to UV light, which results in greater ROS and free radical production [161]. TiO₂ nanoparticles have been shown to cause far greater damage to DNA than does TiO₂ of larger particle size [162]. While 500 nm TiO₂ particles have some ability to cause DNA strand breakage, 20 nm TiO₂ nanoparticles are capable of causing complete destruction of super-coiled DNA, as demonstrated in a plasmid DNA assay, even at lower doses and without exposure to UV. In addition to the increased potential for DNA damage from engineered metal oxide nanoparticles, another concern for their application in cosmetics is the potential for inhalation, ingestion, and penetration through the skin. Once in the blood stream, nanomaterials can be circulated inside the body and are taken up by organs and tissues such as the brain, liver, spleen, kidney, heart, bone marrow, and nervous system [159]. With their stability, the damage of these nanoparticles to human tissues and organs can occur through a traditional ROS pathway, or through accumulation that can impair their normal functions. *In vitro* studies on BRL 3A rat liver cells exposed to 100–250 µg/ml of Fe₃O₄, Al, MoO₃ and TiO₂ nanoparticles revealed significant damage from ROS in these cells [163]. Carbon nanotubes have also been shown to be toxic to kidney cells and inhibit cell growth [164]. The stability of nanomaterials in the environment has also been linked to brain damage and mortality in several aquatic species [165, 166].

Due to the potential toxicity associated with prolonged use of metal oxide nanoparticle sunscreens, it is crucial to search for alternative ingredients that are non-toxic and effective at blocking UV. It is highly expected that these ingredients should be biodegradable, and less toxic to mammalian cells than metal oxide nanoparticles. The recent discovery of ivy and other naturally occurring nanoparticles provides a promising alternative to engineered metal oxide nanomaterials for cosmetics applications [18]. To explore the possibility of using ivy nanoparticles for sunscreen, the UV protection properties of ivy nanoparticles were investigated in this study. In addition, skin penetration, cytotoxicity, and environmental risks of ivy nanoparticles have also been investigated in this study.

Materials and Methods

Ivy nanoparticle isolation

Juvenile *Hedera helix* shoots were grown in a greenhouse. The plant was originally taken naturally on the University of Tennessee, Knoxville campus that was transplanted to a pot in a greenhouse. Leaves were removed from the shoots and shoots were trimmed to 6 cm in length. Shoots were sterilized using 1.23% sodium hypochlorite (20% (v/v) commercial bleach) plus 0.05% Tween 20, shaken at 200 rpm for 20 min, and followed by washing three times with sterile water. Sterile shoots were then placed upright into Magenta GA7 boxes containing Murashige and Skoog (MS) medium and were grown at 24°C at 16:8 h photoperiod under $82 \mu\text{mol m}^{-2} \text{s}^{-1}$ irradiance. Aerial roots (rootlets) were

produced after ca. 2 days, which were allowed to grow for an additional 2 days in MS medium to reach approximately 3 cm in length. Aerial roots were then excised from source plants and were transferred to Petri dishes containing MS medium until analysis was performed (between 3 days and 2 weeks). To isolate ivy nanoparticles, the tips of rootlets were homogenized in deionized distilled water. After centrifugation to remove tissue residuals, the solution was dialyzed overnight, then was loaded the BioSep-SEC-S 4000 size exclusion chromatography column and the elution fractions were collected for further analysis.

Atomic force microscopy

The isolated ivy nanoparticle fractions were first air-dried overnight. The air-dried ivy samples were scanned for the existence of nanoparticles using an Agilent 5500 atomic force microscope (AFM) system (Agilent Technologies). The samples were imaged at room temperature (20°C) using Picoview® in tapping mode, which minimizes sample distortion due to mechanical interactions between AFM tip and the surface. To further optimize imaging, the set point amplitude and the amplitude of the oscillating cantilever were adjusted to avoid excessive loading force applied to the samples. In this way, three-dimensional imaging of the surface morphology with very high lateral and vertical resolution has been obtained. The used tips are commercially available silicon probes TAP300AI® (Budget Sensors, Sofia, Bulgaria) with a spring constant of 20-75

N/m, a resonant frequency of 300 ± 100 kHz, and a radius of curvature in less than 10 nm.

Sample preparation

The calculation of isolated ivy nanoparticles was based on the number of the particles on the AFM images and the used volume to obtain these nanoparticles. To prepare the same concentration of TiO₂ suspension, TiO₂ particles with a diameter of 50 nm (99% purity) were purchased from Nanostructured & Amorphous Materials Inc. (Houston, TX). The particles were first ultrasonically dispersed in water at 5 W for 30 min, then were used for later UV/Vis study and cytotoxicity study.

UV/Vis extinction

The UV/Vis extinction (absorption and scattering) spectra were measured using a Thermo Scientific Evolution 600 UV/Visible spectrophotometer (Thermo Fisher Scientific, Waltham, MA). The optical length of the quartz cuvette was 10 mm. The wavelength of the light started at 250 nm and stopped at 800 nm. Ivy nanoparticles at 4.92 µg/ml were measured for UV/Vis. The same concentration of TiO₂ nanoparticles was measured for UV/Vis under the same conditions.

Cytotoxicity study

HeLa cells were cultured in a DMEM (Mediatech Inc, Manassas, VA) solution supplemented with 10% heat-inactivated fetal bovine serum in a humidified incubator with an atmosphere of 5% CO₂ in air at 37°C. The TiO₂ or ivy

nanoparticle aqueous suspension was added to DMEM solution supplemented with 10% fetal bovine serum to prepare a DMEM solution containing nanoparticles, which was used to investigate the cytotoxicity against HeLa cells. Negative controls consisted of DMEM with 10% fetal bovine serum, without the presence of nanoparticles. For apoptosis analysis, the cells were harvested 24 hours after addition of nanoparticles, fixed and stained with propidium iodide, then were analyzed using Bechman Coulter Episc XL (Bechman Coulter, Brea, CA) with a 488 nm argon laser.

Nanoparticle degradation

Purified nanoparticles were sonicated at 5 W for 20 minutes to physically disperse the nanoparticles so that individual ones that could be analyzed. SDS was then added to the nanoparticle solution to make a final concentration of 0.5%. To the following, 50 µg/ml of Proteinase K was added. The solution was then incubated at 37°C from 15 minutes to 4 hours. Upon completion of the digestion, the sample was air-dried and imaged using AFM to determine if the nanoparticles were degraded. The control sample was prepared in the same way except that the Proteinase K was not added before incubation. In addition to examining enzymatic digestion with Proteinase K, the effects of varying temperatures were examined by incubation of the nanoparticles from 4-37°C. Similarly, the nanoparticles were added to cell culture medium for 24 hours to determine their stability in a typical cell culture media. All samples were then air-dried and imaged by AFM.

Statistical analysis

To determine if there were significant differences in cytotoxicity among HeLa cells incubated without or with different nanoparticles, a Student's *t* test for comparisons of each pair with 95% confidence was carried out using JMP 8 statistical software.

Results and Discussion

Ivy nanoparticle isolation and topographic characterization

The first stage in assessing the UV protective abilities of the nanoparticles required isolation and purification of the nanoparticles from the aerial rootlets. In order to facilitate easier collection of rootlets, a tissue culture method was developed for the aerial rootlets that allowed them to grow on culture plates in a nutrient agar. Another advantage of this technique is that the aerial rootlets grown in this culture system are sterile, and free from any environmental contaminants. AFM studies were conducted on the cultured rootlets, and their wild counterparts. Similar nanoparticles were observed as originally discovered in wild ivy [18]. In order to generate bulk preparations of nanoparticles, the aerial rootlets from culture plates were harvested and homogenized in a microfuge tube with heat sterilized forceps. To remove the large debris, the homogenate was centrifuged at 9,000 x g for 10 minutes. This separated large cellular debris from the much smaller nanoparticles. The supernatant was then filtered through a 200 nm filter and dialyzed overnight to remove compounds with a molecular weight

less than 12,000 Daltons. The dialyzed solution was then loaded to a BioSep-SEC-S 4000 column developed by Phenomenex (Phoenix, AZ), with a flow rate of 0.5 ml/min, and all fractions were collected during the first 60 minutes. These fractions were then air-dried and analyzed by AFM for the existence of expected ivy nanoparticles. From Figure 19, it was found that the isolated ivy nanoparticles had a diameter of 65.3 ± 8.04 nm, based on measurements of 30 randomly counted nanoparticles that were not dominated by other particles. Large agglomerates of nanoparticles ranging from 100-200 nm were ignored from the particle size determination.

UV extinction of ivy nanoparticles

To demonstrate the ability of ivy nanoparticles for UV protection, the optical extinction spectra of these nanoparticles was measured using an ultraviolet and visible wavelength (UV/Vis) spectrophotometer. From the experimental data, it was found that the ivy nanoparticles, at a concentration 4.92 $\mu\text{g/ml}$, had a significant extinction in the ultraviolet region, while having little extinction at the visible and near infrared regions. This indicated that ivy nanoparticles would effectively block UV radiation without the opacity observed in other metal-based nanoparticles.

Comparison of the UV blockage with TiO_2 nanoparticles at the same concentration indicated that the total extinction of the ivy nanoparticles from 280 nm to 400 nm was much better than that of the TiO_2 nanoparticles (Figure 20).

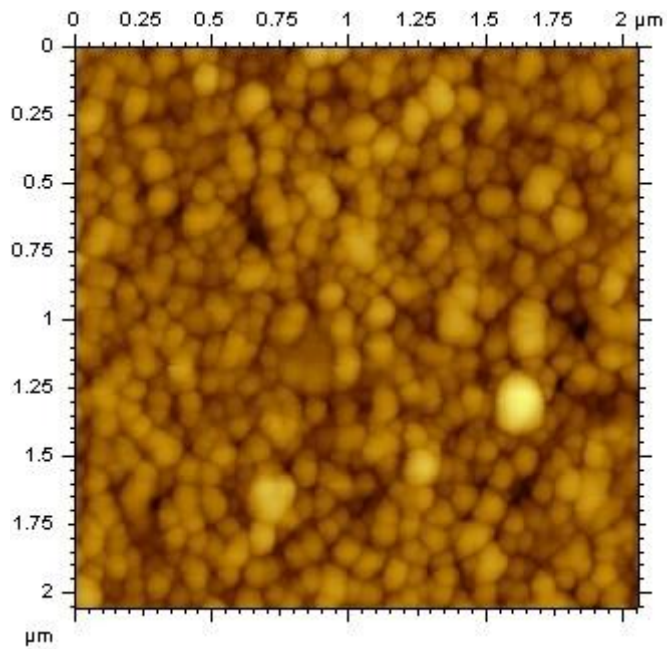


Figure 19 AFM characterization of ivy nanoparticles.

The image shows a 2.05×2.05 μm AFM view of isolated nanoparticles from cultured ivy rootlets, which indicated a high abundance of nanoparticles with an average diameter of 65.3 ± 8.04 nm.

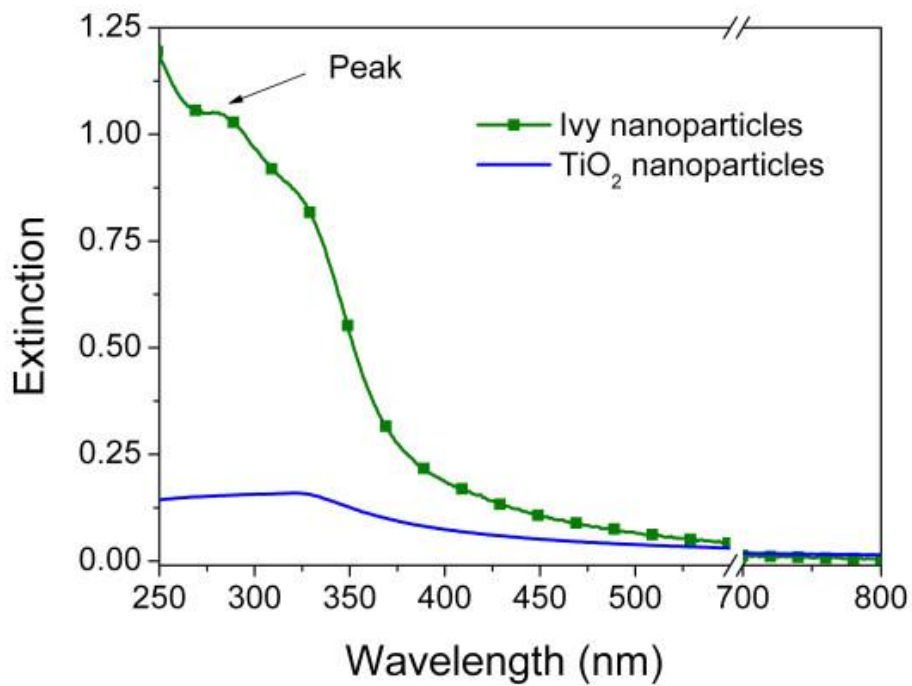


Figure 20 UV extinction spectra.

Spectral profiles represent the UV extinction of the 4.92 $\mu\text{g/ml}$ ivy and TiO₂ nanoparticles. The green line corresponds to the ivy nanoparticles, while the blue line corresponds to the TiO₂ nanoparticles.

The extinction of the ivy nanoparticles decreased sharply after the UV region, which makes ivy nanoparticles more effective in the UV-A/UV-B region and gives them high transmittance in the visible region making them virtually “invisible”.

Our previous studies have confirmed that ivy nanoparticles are organic and have unique adhesive properties [18]. The adhesive effect of these nanoparticles will allow the ivy nanoparticles to remain on the skin for a longer period of time, and thus enhance their UV protective effect. The combination of these unique factors makes the ivy nanoparticles an appealing candidate for the development of a novel sunscreen product.

Cytotoxicity

Although nanoparticles greater than 20 nm in diameter have not been reported to permeate through human skin, this data was obtained using healthy individuals in an optimal setting [155]. In specific cases, the skin structure can be changed to allow the penetration of large particles into the blood system, which has been demonstrated by the ability of 1,000 nm particles to access the dermis when intact skin is flexed [167]. More frequently, however, when skin is damaged, as in the case of people with sunburn, blemished skin, frequent shaving, or massages, there will be an increased risk of penetration [168-170]. A recent report by the US-based Environmental Working Group on the health risks of commercially available cosmetics and personal care products found that more than half of all cosmetics contained ingredients that act as “penetration enhancers” [171]. This raises further concerns for the safety of applied nanoparticles for personal care

and cosmetics, since these agents will presumably increase the penetration potential of nanoparticles. As such, the cytotoxicity of nanoparticles should be thoroughly tested before their application in sunscreens.

Due to the increased toxicity associated with internalized nanoparticles, it is thus essential to examine the cytotoxicity of ivy nanoparticles. HeLa cells, a mammalian endothelial cell line commonly used for testing the toxicity and trafficking of nanoparticles, were thus selected [172-174]. In the experimental study, 1 $\mu\text{g/ml}$ ivy nanoparticles were incubated with HeLa cells for 24 hours to test the cytotoxicity of these ivy nanoparticles. The toxicity was determined using propidium iodide staining and was examined by flow cytometry. No toxicity was observed compared to the control upon incubation with the ivy nanoparticles. However, in the same study, the same concentration of TiO_2 nanoparticles exhibited significant toxicity to HeLa cells. In a standard flow cytometry experiment (Figure 21A), Gate C in each plot was defined for the cell population with less DNA, and thus represented the cells experiencing apoptosis. Gate B from the plots was the HeLa cells with more DNA, which indicated replicating cells at differing growth stages. Statistical analysis concluded that there was no significant difference in the percentage of cells experiencing apoptosis between the control cell population ($13.5\% \pm 1.27\%$) and cells incubated with ivy nanoparticles ($11.5\% \pm 1.06\%$) (Figure 21B). However, in the cells incubated with TiO_2 , $24.3\% \pm 0.7\%$ of cells were experiencing apoptosis, which was significantly higher than the control cell population ($p = 0.011$) and the cells incubated with ivy

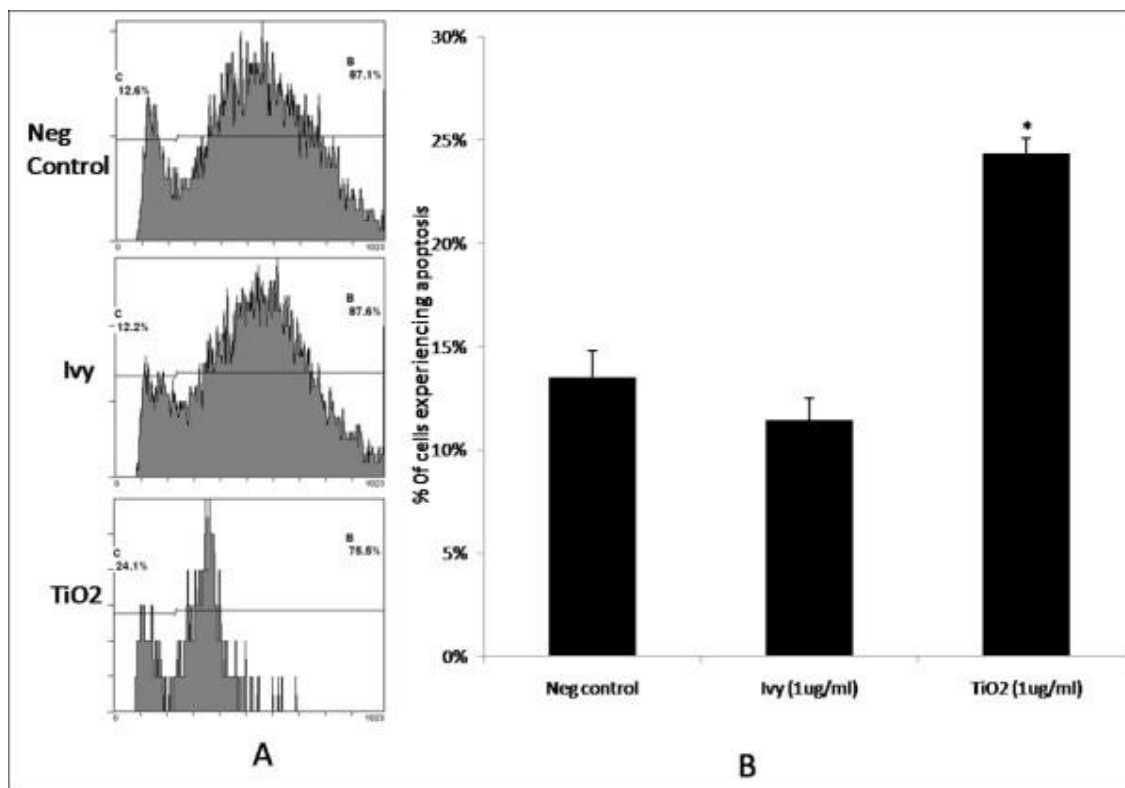


Figure 21 Cytotoxicity analysis.

HeLa cells were incubated with or without nanoparticles for 24 hours and stained with propidium iodide. The cell apoptosis was then determined by detection of fluorescence using flow cytometry. (A) Representative flow cytometry plots for each of the three samples: negative control (Neg control), ivy nanoparticle (Ivy), TiO₂ nanoparticle (TiO₂). (B) Cells experiencing apoptosis in the three samples. Each point represents an average of 3 samples from one of three experiments. * denotes significant difference based on the Student's *t* test ($p < 0.05$).

nanoparticles ($p = 0.007$).

Degradation

Although no cytotoxicity of ivy nanoparticles was found in the HeLa cell line, the possibility of these ivy nanoparticles exhibiting toxicity in the body may still exist. There have been observations with gold-dendrimer nanoparticles accumulating in the liver that might damage normal liver function [175]. To address this concern for ivy nanoparticles, the ability of the nanoparticles to be degraded was tested in case they pass through the skin or mucous membranes. If the ivy nanoparticles were degradable, then they would be digested after their penetration through the skin and lose their normal nano-structure and thus any toxicity based on the nano-morphology of the particles. The degradability of nanomaterial is also beneficial to the environment when considering reports that nanomaterials have been linked to damage in fish, mortality in water fleas, and have bactericidal properties that can impact ecosystems [154, 159]. Thus, the biodegradability of these ivy nanoparticles was also investigated in this study.

Our experimental studies indicated that at temperatures from 4-37°C, the ivy nanoparticles were stable and could be readily imaged by AFM. In addition, sonication from 5-9 W was not effective at destroying the particle structure, but did serve to disperse the particles and prevent the formation of large agglomerates. Incubation of the ivy nanoparticles in RPMI, a common cell culture media, at 37°C for up to 24 hours did not result in digestion of the nanoparticles as assessed by AFM. To test the ability for the particles to be broken down by

enzymatic digestion, Proteinase K was used in an attempt to digest the nanoparticles. Digestion was carried out from 15 minutes to 4 hours, to determine if the extent of incubation affected the digestion of the particles. After incubation with Proteinase K for 30 min, it was no longer possible to image the nanoparticles with AFM. As shown in Figure 22, after enzymatic digestion, the ivy nanoparticles were degraded and lost their normal structure. This enzymatic digestion by a common proteinase could further reduce the risk to the environment and human tissues and organs. This gives organic nanoparticles a definitive advantage over metal oxide nanoparticles, since these particles resist breakdown by biological organisms and remain in the body or environment for prolonged periods of time. It should be pointed out that the above nanoparticles used for the Proteinase K digestion were collected based on size which also matched well with the UV 280 nm detection. As expected, they have been totally degraded. However, the possibility could not be eliminated whether there might be other type/size of nanoparticles that had not been detected by UV detector, and as a result, were not collected for the Proteinase K digestion. The long-term objective of this study is to propose protein-based ivy nanoparticles for UV protection.

Skin penetration

Another major concern of ivy nanoparticles in cosmetic is their probability to penetrate through the skin into the circulatory system [176, 177]. The development of proper markers for the detection of ivy nanoparticles in the skin

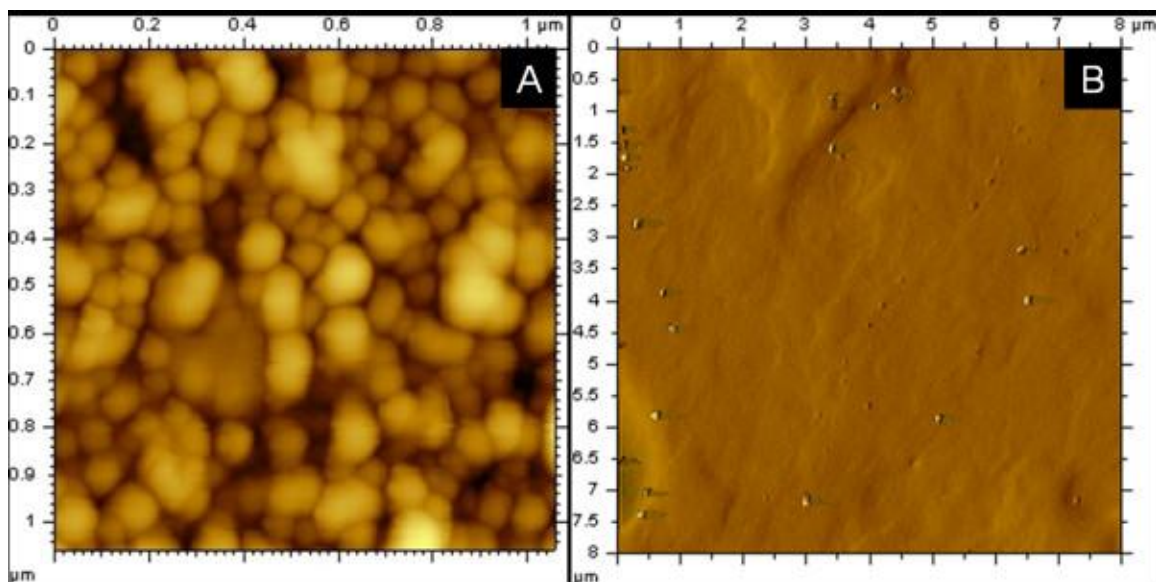


Figure 22 Biodegradability of ivy nanoparticles.

The isolated ivy nanoparticles were incubated without (A) or with (B) Proteinase K at 37°C for 30 min. The structure of the samples was then analyzed with AFM using tapping mode.

takes considerable time, however, a simple mathematical modeling and computational approach may allow rapid analysis for the potential of ivy nanoparticles to penetrate through skin.

Skin structure, is composed of the protective outer SC layer and a viable epidermis and dermis layer with other accessory glands [178]. The penetration of particles in the skin can occur through pilosebaceous pores (diameter: 10-70 μm), sweat gland pores (diameter: 60-80 μm) and lipid matrix that fills a gap of 75 nm between dead corneocytes in the SC [178-180]. As the intact skin has more than one layer in humans, it is expected that ivy nanoparticles will have different diffusion activities in different layers. *Ex vivo* and *in vivo* experimental data supported that the SC has the most packaged properties and is not permeable to many chemicals and drugs [181]. A skin diffusion study indicated that the SC has a diffusion coefficient 10^3 times lower than the deeper viable layer for the same chemical [182]. Another study for nanoparticles in human skin also indicated that nanoparticles with a size of more than 20 nm rarely have a chance to penetrate through the SC layer [183]. Therefore, to understand ivy nanoparticle diffusion and penetration in human skin, it is essential to understand the diffusion process of these nanoparticles in the SC.

There are many papers dealing with the transport of nanoparticles through the SC layer of the skin in the current literature [155, 170, 184-187]. While the data vary depending on the experimental setup, it is generally agreed that the depth of penetration varies with the material properties of the nanoparticles, the

size of individual particles, their shape, and other physicochemical factors [184]. Studies have suggested that sunscreens composed of TiO₂ and ZnO nanoparticles do not pass into the upper layers of the SC. However, as mentioned earlier, these studies have only examined healthy adult skin models [151, 154, 188]. More realistically the skin to which the sunscreen will be applied has been damaged, either by prior sun exposure, or by a variety of other factors that damage the skin. Previous discussion has been addressed on how damage to the skin and small particle size increase the depth to which nanoparticles will penetrate [155, 156, 168-170].

Despite the heterogeneous structure of the SC layer, in cases where penetration is concerned, the skin behaves as a homogeneous membrane and the diffusion law still holds [189-192]. To understand the dynamic activities of the ivy nanoparticles applied to the skin, Fick's Second Law is applied and described as the follows: $(\partial\Phi/\partial t) = D(\partial^2\Phi/\partial x^2)$. The determination factor is the diffusion coefficient (D). This D is normally defined to be: $D=k_B T/6\pi\eta R$. In the case of ivy nanoparticles, R is radius of ivy nanoparticles and is set at the value of 32.65 nm, η is the viscosity of the SC lipid matrix (0.02 kg/m s), k_B is the Boltzmann constant ($1.38 \times 10^{-23} \text{ m}^2 \text{ kg s}^{-2} \text{ K}^{-1}$), and T is the absolute temperature for human skin (310.15 K). In this simplified model the surface properties of varying nanoparticles are ignored and only the radius of the nanoparticles effects diffusion. The SC layer, which is 20 μm deep, is lipophilic and acidic with variations in gender, anatomical sites, and environmental settings [193].

Based on the model and obtained parameters, the dynamics of nanoparticle diffusion in the SC layer of the skin was simulated. In Figure 23, the predicted distribution of different-sizes of nanoparticles after 8 and 20 hours of application is shown. While nanoparticles with a diameter less than 10 nm have a chance to reach into the bottom of the SC layer (Figure 23), nanoparticles over 40 nm can only reach 5-8 μm into the SC layer after 8 hours of application and 8-13 μm after 20 hours, as displayed in Figure 23. This agrees well with previous experimental studies about other nanoparticles within the same size range [194]. Considering the normal period of exposure to sunlight in humans is less than 8 hours, and the diameter of the ivy nanoparticles is 65.3 nm, it is expected that ivy nanoparticles can be used in cosmetics applications without a risk of penetration.

Conclusions

The concern for the biosafety and health risk for the metal-based and engineered nanoparticles in sunscreens has led to the search for alternative replacement nanoparticles. In this study, naturally occurring ivy nanoparticles were investigated to replace TiO_2 and ZnO that are currently widely used in sunscreen products. Based on experimental data, ivy nanoparticles have been demonstrated to have the potential levels of UV protection necessary to warrant further investigation for uses in cosmetics. The cell toxicity of ivy nanoparticles was next tested and it was determined that ivy nanoparticles exhibited much less toxicity than widely used TiO_2 nanoparticles. Without obtaining the proper marker

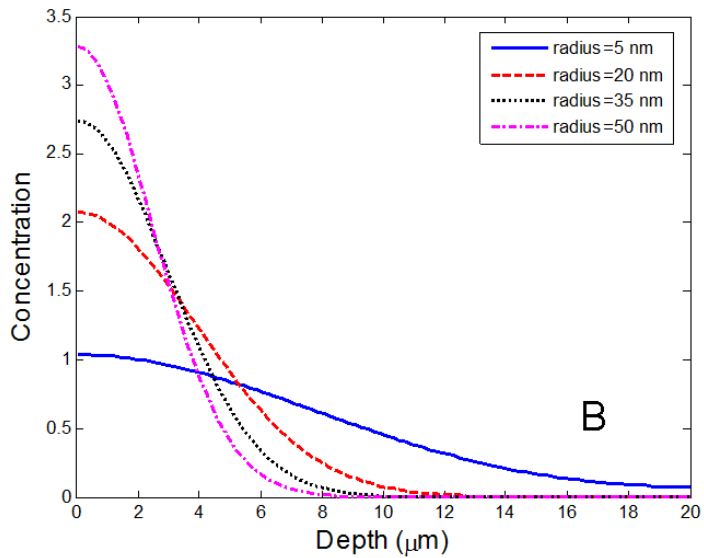
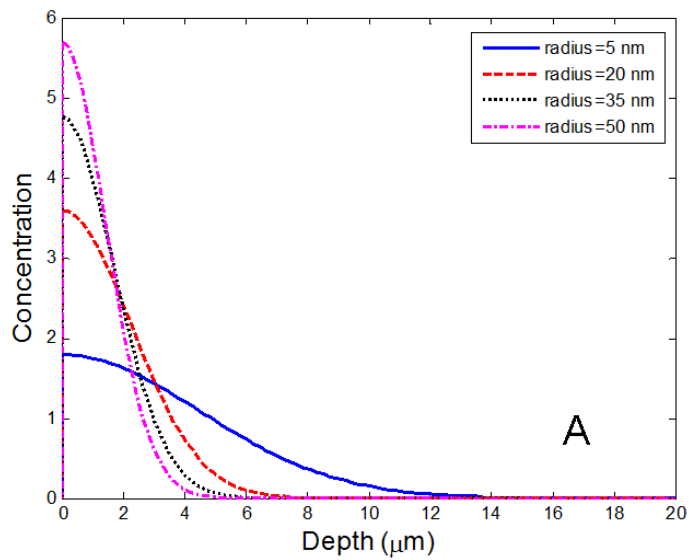


Figure 23 Distribution of nanoparticles in SC layer of skin.

Computational simulation results for the distribution of nanoparticles in the SC layer of human skin 8 hours (A) and 20 hours (B) after application to the surface of the skin.

for experimental determination, a mathematical model was used to analyze the diffusion dynamics in the human skin, especially in the SC layer. Through this analysis, ivy nanoparticles with a diameter of 65.3 nm are believed not to reach the bottom of SC layer in normal conditions for short periods of time after application. The biodegradability of these ivy nanoparticles further eliminates concerns regarding environmental contamination and in the case of entry into the body. All of the above studies demonstrated that naturally occurring ivy nanoparticles could be a promising alternative for UV protection in cosmetics, especially with concerns regarding the safety of metal-based nanoparticles. With increased dangers associated with more UV passing through the atmosphere [195], the need to protect human from skin cancer elicits the need for safe and effective UV protective agents. The promising application of these ivy nanoparticles thus provides a better chance to help protect people from UV radiation.

**CHAPTER VI. CHARACTERIZATION OF ENGLISH IVY
(HEDERA HELIX) ADHESION FORCE AND IMAGING
USING ATOMIC FORCE MICROSCOPY**

A version of this chapter was originally published by Lijin Xia, Scott C. Lenaghan, Mingjun Zhang, Yu Wu, Xiaopeng Zhao, Jason N. Burriss and C. Neal Stewart:

Lijin Xia, Scott C. Lenaghan, Mingjun Zhang, Yu Wu, Xiaopeng Zhao, Jason N. Burriss and C. Neal Stewart. "Characterization of English ivy (*Hedera helix*) adhesion force and imaging using atomic force microscopy." *Journal of Nanoparticle Research* 13 (2011):1029-1037.

Dr. Mingjun Zhang initiated, manipulated and supported the whole project. Lijin Xia performed the major part of the work. Dr Xiaopeng Zhao, Dr. C. Neal Stewart and Scott C. Lenaghan provided professional advice of the project. Scott C. Lenaghan helped with AFM. Yu Wu helped with simulation study, Jason N. Burriss and C. Neal Stewart helped with cultured ivy rootlets.

Introduction

Hedera, or ivy, is a genus containing approximately 16 species of climbing or ground-creeping evergreen plants [196]. On suitable surfaces, such as trees and rock faces, ivy has the ability to climb 25-30 meters above the ground and hold fast to vertical surfaces. This unique ability to climb has drawn great interest from scientists as early as the 1800s. Charles Darwin first observed that the aerial rootlets produced on creeping and climbing stems "secreted a *little yellowish matter*" upon first contact with an attaching surface [197]. Little progress has been made in determining the structure and composition of this yellowish

adhesive since the initial observation from Darwin. In the mid 1970s, Endress and Thomson investigated the adhesive of Boston ivy (*Parthenocissus tricuspidata*), using transmission electron microscopy (TEM) [198, 199]. Their studies provided in-depth details about the structure of attaching Boston ivy tendrils, but limited information about the nature of the secreted adhesive. Other studies have focused on the morphology of the rootlets using light and scanning electron microscopy, but have not provided information on the structure and composition of the adhesive [200, 201]. In 2008, Zhang et al. conducted one of the first studies focused on identifying the structural components of the adhesive secreted from naturally growing ivy rootlets. Using atomic force microscopy (AFM) they observed a high abundance of uniform nanoparticles deposited onto the attaching surface. These nanoparticles were about 70 nm in diameter, and were observed on a variety of surfaces including mica, silicon wafer, and glass [18]. From the discovery, it is hypothesized that nanoparticles are the key component that generates the strong adhesion used by ivy to climb vertical surfaces.

Intense research has been conducted over the last decade on the contribution of nanostructures to surface adhesion. One of the most celebrated examples is the discovery of nanofibers on the footpads of gecko. The existence of these abundant and deformable nanofibers maximizes the intimate contact area between the toes of gecko and the climbing surfaces. This intimate contact facilitates inter-molecular interactions through van der Waals force [202, 203].

Similar attachment mechanisms have been observed in flies, beetles, and lizards [204]. Although these studies have focused exclusively on dry adhesion and on fibrillar structures from the micro- to nano-scale, shape-insensitive optimal adhesion has been studied in mathematic models [205]. From these models it was predicted that for nano-sized structures, shape is not as important as the size of the structure in relation to generating adhesive strength. Following this principle, it is expected that nanoparticles offer the same potential for surface adhesion due to their size scale.

A theoretical model was recently developed by our group to evaluate the impact of van der Waals interactions between ivy nanoparticles and solid substrates. From the model, it was confirmed that van der Waals force alone was significant to account for the strength of attachment of ivy [206]. Experimentally, various nanoparticles have been tested to enhance adhesive strength or as filler to polymeric adhesives [207, 208]. Although it is not clear whether the nanoparticles contribute directly or indirectly to the strength of adhesion, a recent study has provided firm evidence of the adhesion ability of polystyrene nanoparticles [209].

The existence of adhesive nanoparticles will prompt their potential applications in a variety of fields. Nanoparticles have already been explored as fillers in the glue industry. Adherent nanoparticles also hold a significant promise to future research in drug delivery. Biodegradable nanoparticles provide controllable, sustained drug delivery *in vitro* [210]. *In vivo* studies, however, have

shown that nanoparticles are not effective at adhering to vascular walls under shear stress. Adherent nanoparticles may overcome this deficiency, allowing the lingering of nanoparticles in activated or inflammatory endothelial cells under fluid shear stress thus improving the cell uptake of drug-carrying nanoparticles. An additional advantage of ivy nanoparticles is their natural origin and biocompatibility which provide them extra potential use in medical and bioengineering fields. Ivy nanoparticles have recently been proposed to be a prospective candidate to replace metal-based nanoparticles for sunscreens [92]. Biocompatibility combined with strong adhesion ability will make ivy nanoparticles an ideal active component in the design of bioglue, surgical suture, or other wound healing materials.

Before taking significant steps in the direction of proposed applications, it is essential to first understand the strength of the adhesive, as well as the principles involved in generating the attachment strength. In an effort to understand how nanoparticles contribute to the attachment strength, accurate measurement of the adhesive force at proper scale was necessary. AFM is a fundamental tool used to determine nanoscale forces, and is accurate even when measuring intermolecular forces in piconewtons [211]. AFM can also be used to monitor the fundamental mechanical properties of materials such as adhesive strength, compressibility, and elasticity [209, 212-214]. Small non-covalent interactions, such as van der Waals force, hydrophobic and electrostatic interactions, and protein folding can also be determined using AFM [215, 216].

As such, AFM-based approach has been applied to examine the nanoscale material properties of the nanocomposite adhesive secreted from English ivy.

In this study, a method was first developed for growing English ivy rootlets in tissue culture, to eliminate concern of contamination and control the growth stages of ivy rootlets. The adhesive of tissue-cultured rootlets was then compared to naturally grown rootlets for their nanostructures. Both were found to contain nanoparticles with similar shape and size. After confirmation of the existence of nanocomposite adhesive, its strength was further determined using force versus distance curves generated by AFM during the 24-hour study. At the same time, the elasticity and extension length of the secreted adhesive was monitored, to collect useful data for analyzing and understanding the adhesive hardening process.

Materials and Methods

Sample preparation

Juvenile *Hedera helix* shoots, cut from a naturalized source on the University of Tennessee, Knoxville campus, were grown in a greenhouse under controlled temperature, humidity, and light availability. Leaves were removed from the shoots and shoots were trimmed to 6 cm. Shoots were then sterilized using 1.23% sodium hypochlorite (20% (v/v) commercial bleach) plus 0.05% Tween 20, shaken at 200 rpm for 20 min, and subsequently washed with sterile water three times. Sterile shoots were then placed upright into Magenta GA7 boxes

containing MS medium and were grown at 24°C at 16:8 h photoperiod under 82 $\mu\text{mol m}^{-2} \text{s}^{-1}$ irradiance [217]. Aerial roots were produced after ca. 2 days and were allowed to grow for an additional 2 days in MS media. Aerial roots were excised from source plants and were approximately 3 cm in length. These were transferred to Petri dishes containing MS medium until analysis was performed (between 3 days and 2 weeks). In preparation for adhesive analysis, the tip of rootlets was gently cut under a bio-safety cabinet and touched on the silicon wafer surface to release the content. Samples were then either processed immediately, or allowed to air-dry in a bio-safety cabinet for at least 5 hours.

AFM imaging

The freshly prepared or air-dried ivy adhesive samples were scanned for the existence of nanoparticles using an Agilent 5500 AFM system (Agilent Technologies). The samples were imaged at room temperature (20°C) using Picoview® in AC mode, which minimizes sample distortion due to mechanical interactions between the AFM tip and the surface. To further optimize imaging, both the integral and proportional gains were adjusted to avoid excessive loading force applied to the samples. Using this system, three-dimensional imaging of the surface morphology with very high lateral and vertical resolution could be obtained. The probes used were commercially available silicon probes TAP300Al® (Budget Sensors, Sofia, Bulgaria) with a spring constant of 20-75 N/m, a resonant frequency of 300 ± 100 kHz, and a radius of curvature of less than 10 nm.

Adhesion force measurement

To measure the adhesive properties of the ivy secretion, force vs. distance curves were generated using an Agilent 5500 AFM system. The AFM probe was first calibrated with bare silicon wafer as a substrate to obtain a deflection sensitivity of 33.5 nm/V and a force constant of 4.33 N/m for the TAP150AI-G® (Budget Sensors, Sofia, Bulgaria) cantilever probes. The location of the adhesive was verified with a CCD camera mounted to a 10X objective, and the cantilever was moved over the center of the adhesive. Once the location had been established, approach of the tip was initiated and the tip was allowed to contact the sample surface for 2 s so that the probe and adhesive formed a complex. The tip was then withdrawn from the adhesive and the deflection of the cantilever was measured. A series of 30 force curves exhibiting adhesion events was taken for each time point during the curing process. The mean and standard deviations were calculated using Microsoft Excel®. To calculate Young's modulus, the slope of the approach line for each force curve was obtained using Picoimage® and was then applied to equation $E = (F/dL) \cdot (L/A)$. In this equation, E is the Young's modulus, F/dL is the slope of the approaching curve, L is height of the material, and A is the contact area. The height of the material, L, was determined by imaging the adhesive and obtaining a vertical profile from the topography scan in Picoimage®. The area of contact, A, was calculated based on the diameter of the tip according to the manufacturer's specifications.

Results and Discussion

Nanoparticles produced from in vitro ivy rootlets

Because of instrument limitation, a real-time monitoring of attachment process of ivy in nanoscale in the fields becomes difficult. Also, concerns emerge for the contamination of environmental nanoparticles in the open air and for growth stage difference of ivy rootlets in natural conditions. Thus, a method was first developed to grow English ivy rootlets *in vitro*. This method allowed us to have an opportunity to investigate the adhesive properties in different stages. For topographical characterization of the adhesives from cultured ivy rootlets, the rootlets were washed with 20-nm-filtered water and cut at the tips to release adhesive. Freshly samples were extremely soft and prone to smearing by the AFM tip during the scanning. After 5 hours of settlement, however, the adhesive could be clearly imaged. As shown in Figure 24, the nanocomposite was mainly composed of nanoparticles 60-85 nm in diameter. The average diameter for the nanoparticles was 70 ± 6.5 nm, which was comparable to the previous report [18].

This observation confirmed the previous report of nanoparticles in ivy adhesive. Nanoparticles embedded in a polymeric matrix are not unique to ivy adhesive. The existence of similar types of nanocomposites has been confirmed in the secretions of a variety of marine species, including polychaetes, mussels, barnacles, and sea stars [231-233]. The size of spherical particles in these adhesives is in the same range as those found in the ivy secretions, 60 nm for

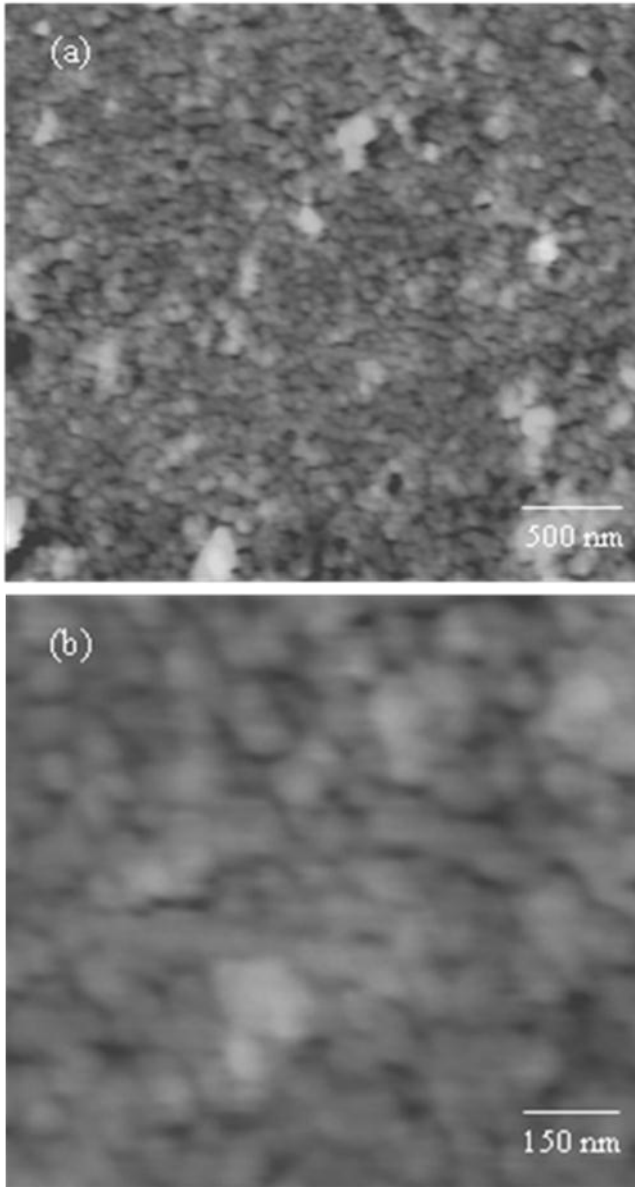


Figure 24 Nanoparticles released from the in vitro grown ivy rootlets.

AFM tapping-mode images of content from the tips of cultured ivy rootlets after 5 hours of settlement. (a) 3.3x3.3 μm scanning window. (b) 1.0x1.0 μm scanning window.

mussel, 80 nm for barnacles, and 50-100 nm for polychaetes and sea stars [218]. The fact that these nanoparticles can be observed in a variety of species indicates a conserved approach to generating adhesive materials. Most reported marine adhesives consist of protein complexes dispersed in a polysaccharide matrix [218], probably due to the multi-functionality and diversity of protein. A study done by Callow et al. showed that algal spores become less sensitive to detachment after treatment with proteolytic enzymes [219], indicating the key role of proteins in attachment. Some proteins in adhesive have important biochemical characteristics, such as being rich in polar and charged residues, which presents a significant number of functional groups for cross-linking and adhesion. A recently identified barnacle cement protein is a surface-coupling protein (Mr_{cp}-19k) which could efficiently adsorb to surfaces with various characteristics, regardless of charge and hydrophobicity [220].

High adhesion strength of ivy nanoparticles

As observed in the above biological adhesives, the existence of a large amount of proteins in the form of nanoparticles implies that they play an important role in attachment. However, direct evidence for the adhesion ability of these nanoparticle-dominated adhesives has not been obtained. After confirmation of the existence of nanoparticles from cultured ivy rootlets, its adhesion force was studied for the first time using AFM. Following calibration and determination of the deflection sensitivity and force constant of the AFM tip, force vs. distance curves were performed to measure the “pull-off” force generated from the

interaction between the tip and the adhesive. Thirty successful approach-retract curves of freshly-prepared ivy adhesive samples were conducted to determine the optimal adhesive force. Out of these curves, the values of pull-off force ranged from 274 to 307 nN, with an average value of 298 ± 8.34 nN. A typical force curve exhibited a single pull-off event during measurement (Figure 25a), even though saw-toothed curves were observed occasionally (Figure 25b). The saw-toothed pull-off is typical of polymer based materials, and indicated that the tip was interacting with multiple components of the nanocomposite adhesive.

The nanoscale adhesion force for freshly-released ivy adhesive averaged 298 nN, which is 4 times greater than what could be measured for the adhesive from algal spores using AFM [219]. However, the readings are close to a recent study of adhesion force between polystyrene a nanoparticle and nanofiber in the range of 159.5 – 384.9 nN [209]. Also, to ensure that the measured force was not due to the tip contamination, the tip was frequently moved to a bare silicon surface to calibrate the pull-off force. The force measured on the bare silicon wafer surface was around 30 nN, which is comparable to previous reports [221].

High elasticity of ivy nanoparticles

The addition of filler materials to adhesives normally strengthens the adhesive, but reduces the tack which is a required character for permanent attachment. The addition of a nanomaterial, however, showed different behavior, exhibiting an increase in both strength and tack [222], which might explain the advantage of nanoparticles for strong attachment. Tackiness theory predicts that as the elastic

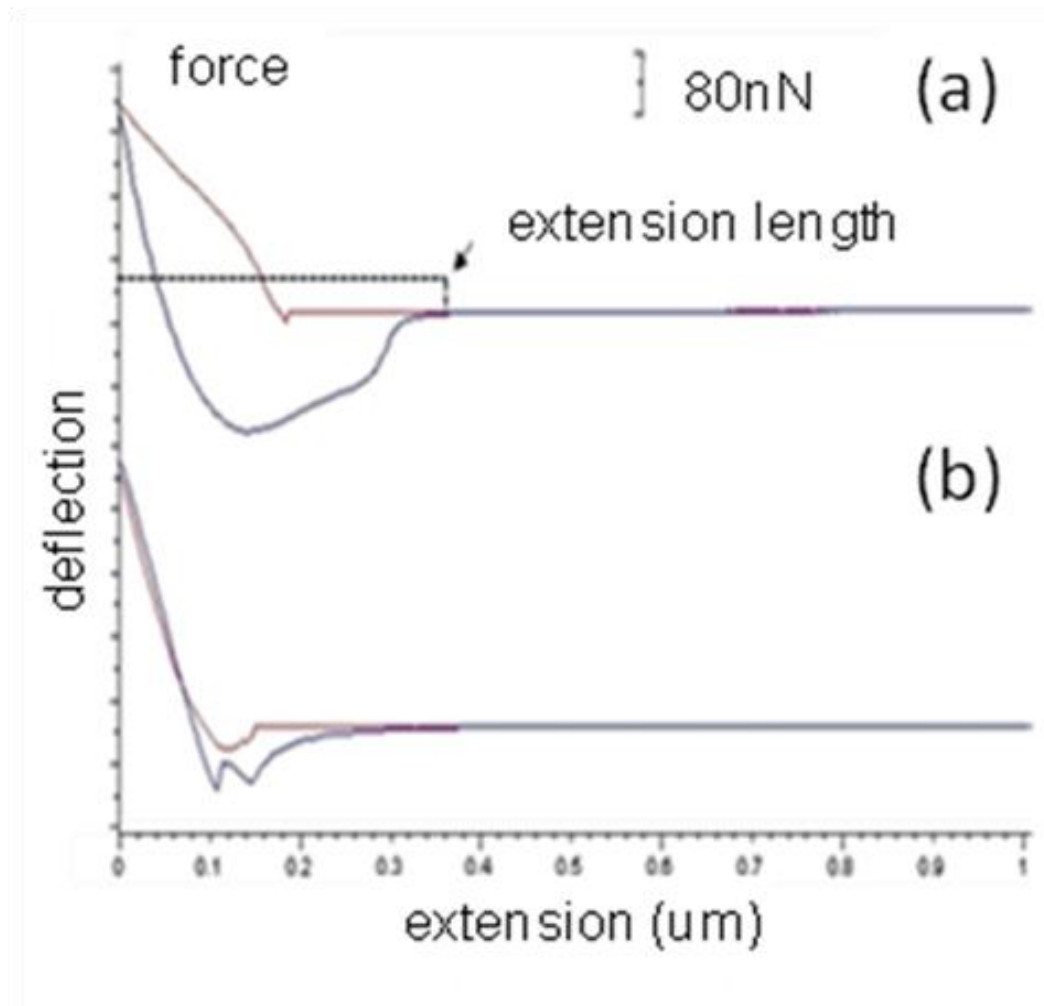


Figure 25 Adhesion force of ivy adhesive measured by AFM.

A typical approach-retract cycle illustrates the adhesion profile and other mechanical properties of ivy nanoparticles examined under AFM in (a). Saw-toothed curves were occasionally observed in (b). The red line represents the approaching process and the dark blue line represents the withdrawal process.

modulus of the coating increases, the tack energy decreases [223]. The different tack performance from nanomaterial fillers might be due to their unusual interactions with polymeric matrix, which increases the elastic modulus of the composite adhesive. For this purpose, the elasticity of the ivy adhesive was examined. In this study, the slope of the approach curve was used to calculate Young's modulus. The obtained Young's modulus through this method ranged from 1.035 to 1.297 GPa for the ivy adhesive, and was much greater than what was calculated for algal spores. Young's modulus of the dried adhesive was comparable to a hard material such as rubber, nylon, and some plastics. High elasticity of the ivy nanocomposite could attribute in part to the Hall-Petch effect - when grain size decreases into the nanometer range, stiffness increases due to increased trapping of dislocations at interfaces [224].

Time-based loss of adhesion

The time from initial secretion of the adhesive to permanent attachment is a slow process that involves corresponding changes in the adhesive. These changes could be due to water evaporation after secretion, or chemical changes due to polymerization. Ultimately the changes will be reflected in the hardening of the adhesive, which are believed to correspond to the formation of strong permanent attachment. To follow the change in adhesive properties over time, force vs. distance curves were taken over the course of 24 hours. The time-course of adhesion revealed a slow reduction in the first 8.5 h from 298 nN to 202 nN, followed by a constant level after 24 hours (Figure 26). A 30.2% decrease of

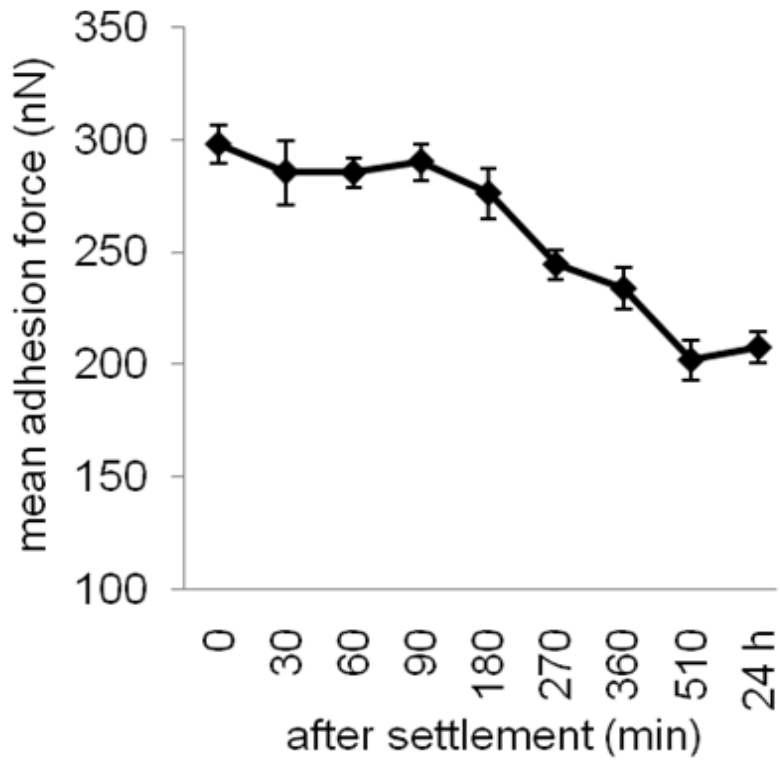


Figure 26 Change of adhesion force within 24 hours.

The force was measured at various time points after deposition. Each point represents an average of 30 retraction curves \pm 95% confidence limits.

adhesion force was observed over a curing period of 8.5 hours. This change was not as great when compared to a 65% decrease observed during the first hour of settlement in the adhesive secreted from *Enteromorpha*, an algae [219]. One explanation for the decreased adhesive force was the hardening of the limited amount of polymer matrix material in the ivy adhesive. As observed with many polymer glues, the hydrated form has a high adhesive strength, whereas the dried form lacks any adhesion. This is due to a change in conformation of the material and the gradual formation of a solid upon drying. Another explanation includes the loss of capillary forces due to the decreased water content during drying process. Capillary forces play a significant role in the adhesive force of the gecko and decreased relative humidity has been related to decreased adhesion force [225]. The freshly-released adhesive contains a significant percentage of water which is lost as the sample dries. The capillary forces associated with the water in the hydrated state would become smaller during drying process, leading to the decreased adhesion force.

Limited change in extension length and Young's modulus

The decreased force over time can be due to the existence of polymeric matrix and be related to changes of elasticity and extension length as observed in previous studies [219], which is also a typical response for liquid adhesives during the hardening process. Because of the existence of a small amount of polymeric matrix in ivy adhesive, it is expected similar change exist during hardening process of ivy adhesive. For this purpose, elasticity and extension

length for the ivy adhesive were also investigated over the 24-hour time course. From Figures 27 and 28, the curing profiles of the ivy adhesive were found to consistent with the pattern observed from the adhesive of the algae *Enteromorpha* [219], but at a much less degree. The extension length (interpreted in Figure 25a) show a limited decrease over 24 hours, indicating a minimal hardening over the time-course. Correspondingly, Young's modulus increased by 20.2% over 6 hours, much less than normally found in liquid or soft polymer adhesives [219]. This observed difference in extension length and Young's modulus change over time was most likely due to the low percentage of polymeric matrix. The existence of a large amount of nanoparticles, on the other hand, does not change in elasticity and extension length during hardening process. The fact that polymeric adhesives, such as tape, are soft and deformable allows for intimate contact over a relatively large surface area making these adhesives optimal to explore the sub-atomic distance of van der Waals force [223]. The strong curing process in normal liquid adhesives works well when contact surfaces are smooth. However, as in the case of ivy, the attaching surfaces for these plants are extremely hard, rough and in irregular shapes. The strong curing process in the contact areas will lead to the notably decreased volume thus the decreased contact area of the rootlets with attaching surfaces. The limited curing process in ivy adhesive thus works to maintain the maximal contact areas through nanoparticle part, and facilitate intimate contact and van der Waals force interactions through deformable matrix part.

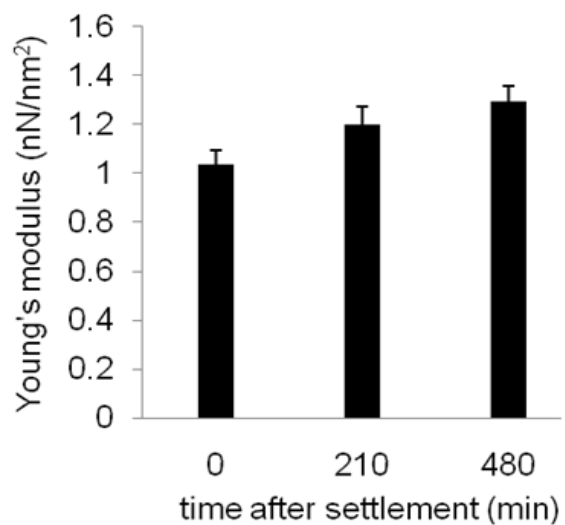


Figure 27 Increased Young's modulus with time for ivy nanoparticles.

Each point represents an average of 30 approach curves \pm 95% confidence limits.

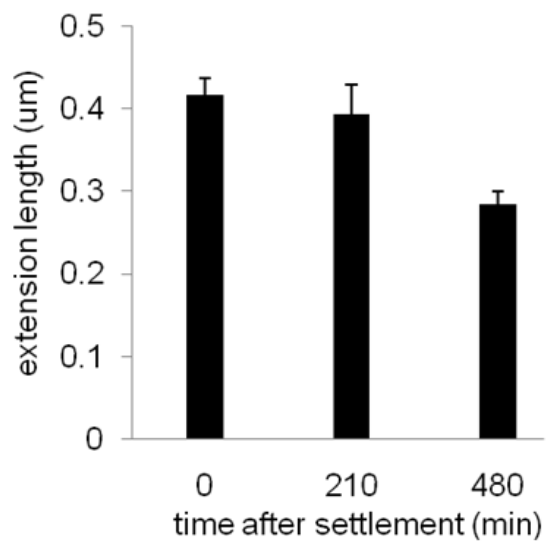


Figure 28 Decreased extension length with time for ivy nanoparticles.

Each point represents an average of 30 retraction curves \pm 95% confidence limits.

Mechanics model of ivy nanoparticle adhesion

Although matrix is deformable, its small amount in ivy adhesive implied they mostly facilitate nanoparticle contact with attaching surfaces because of abundance of nanoparticles in adhesive. As studied in marine adhesives, different mechanisms might exist for strong attachment of nanoparticle components. Because of its strong attachment to surfaces of different physical and chemical properties, van der Waals force is of priority to be investigated. A recent study proposed three mechanical models to explain the strong adhesion of ivy nanoparticles to a rigid substrate based on van der Waals force [206]. The selection of a specific model depends on the contact angle and mechanical properties, especially Young's modulus, of the nanoparticles. Based on the Young's modulus obtained from this study, the Johnson-Kendall-Robert (JKR) model was selected. Johnson-Kendall-Robert (JKR) theory was created to characterize the adhesive contact between elastic spheres based on van der Waals forces, and is applicable to large, soft, and compliant materials with high surface energy [226]. The theory can be applied to various conditions occurring between the ivy nanoparticles and substrate surfaces. Equation (1), based on JKR theory, describes the method to calculate the pull-off force of an elastic sphere in contact with a rigid substrate; essentially a model for the contact between an ivy nanoparticle and a solid surface.

$$F_p = \sqrt{8\pi E^* \omega R^3 \sin^3 \alpha} \quad (1)$$

In Equation (1), E^* is the effective Young's modulus, R is the radius of the particles and α is the contact angle. ω is the work of adhesion, and can be calculated as:

$$\omega = \gamma_1 + \gamma_2 - \gamma_{12} \quad (2)$$

where γ_1 and γ_2 represent the surface energy of the two surfaces, and γ_{12} is the interface energy between the two materials. The value of ω is set here as 0.025J/m^2 as previously discussed [206].

Based on these equations, the adhesion force for spherical nanoparticles with different effective Young's moduli was calculated at two different contact angles of 30 and 45 degrees. As shown in Figure 29, a larger contact angle translates to a larger contact area, which provides a stronger adhesion force for each individual nanoparticle. Similarly, for material with a large Young's modulus, there are stronger van der Waals forces formed between nanoparticles and the surface. From the calculated value of Young's modulus for ivy nanoparticles, between 1.035 and 1.297 nN/nm^2 (GPa), this model indicates that van der Waals force alone could provide forces in the range of 55 nN to 110 nN , depending on actual value for Young's modulus and the contact angle of these nanoparticles to the surface.

The exact chemical composition of the ivy nanoparticles is currently under investigation, and the mechanism that contributes to the strong adhesion will be more accurately interpreted and investigated upon collecting this data. However, calculations based on JKR theory indicated that van der Waals forces alone

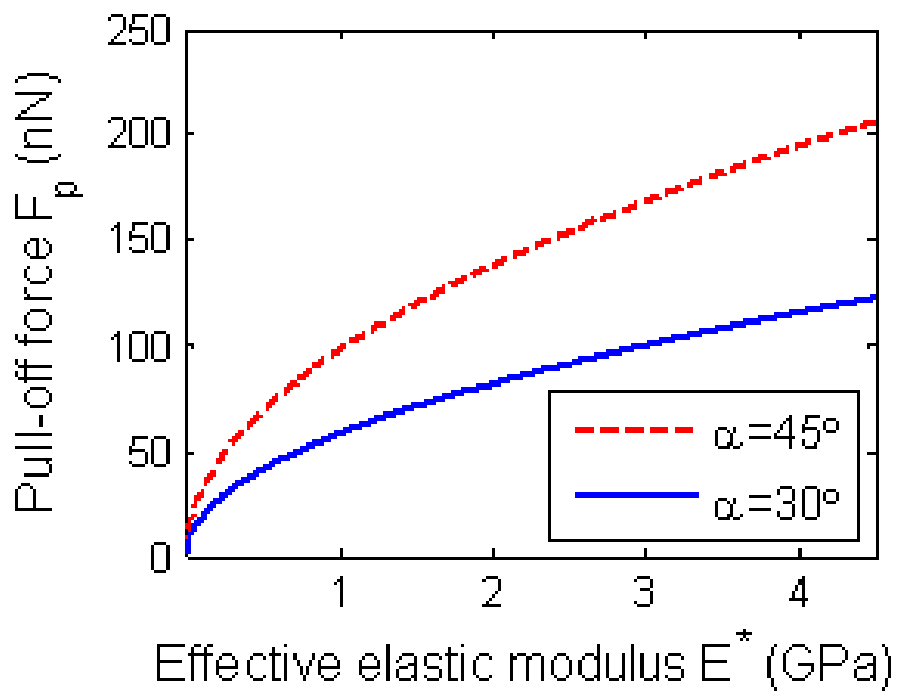


Figure 29 The relationship of pull-off force and effective elastic modulus of nanoparticles.

Curves from the mechanics model of adhesion force between nanoparticles and the substrate for materials with different Young's modulus and at two contact angle of 30 (blue line) and 45 degrees (red line).

would provide ~100 nN of force for the nanoparticles, which is 1/3 of what was measured using AFM. This difference indicates that chemical or mechanical interactions other than van der Waals force are involved in ivy adhesion. These possible interactions include capillary forces, hydrogen bonding, electronic forces, or even cross-linking of the matrix with attaching surfaces [227].

Conclusions

This study used AFM to characterize the structural and mechanical properties of the nanocomposite adhesive from cultured ivy rootlets. The adhesive from cultured rootlets was examined and found to maintain the similar structure of nanocomposite as the naturally grown ivy rootlets. The nanocomposite adhesive was then examined for adhesion strength using AFM. The average force for the fresh adhesive was found to be 298 nN. This force was comparable to other reports of nanoparticle-nanofiber adhesion, but 4 times larger than the adhesive strength of algal adhesives. The mechanical properties of the ivy adhesive were also investigated and a large value of Young's modulus was observed for the nanocomposite adhesive, explaining the strong tackiness of the ivy adhesive. In addition, the curing process of the ivy adhesive was tracked over 24-hours. The limited curing process of the ivy adhesive helps fill gaps in the attaching surface, leading to more intimate contact and increased van der Waals interactions with the surface. A theoretical study based on van der Waals force of ivy nanoparticles was performed, and it was found that other forces exist that contribute to the strong attachment of ivy rootlets except van der Waals force.

This study has provided first-hand experimental data to display and analyze one of the strongest adhesives in nature. Future work will focus on understanding interactions of ivy nanoparticles each other and with the adhesive matrix using functionalized AFM tips. The identified underlying mechanisms that control the strong adhesion of ivy nanoparticles will provide inputs for better design of biocompatible adhesive towards medical applications.

**CHAPTER VII. LIVE SUNDEW PLANT OR EXTRACTS
FROM IVY ROOTLETS FOR METAL NANOPARTICLE
SYNTHESIS**

Introduction

While plant-inherent nanomaterials show advantages compared to synthetic nanomaterials, they have their own limitations. They show limited functionalities themselves, and might require extra care in the applications due to their gentle nature. They might display variety towards applications, are low in yield, and can easily lose their natural functionalities during processing and transportation. To get a large amount of stable nanomaterials with medical effects from plant will be rewarding but may face extreme challenges. It may also require consistent effort to go through a large reservoir of candidate plants if there is no clear clue or implication which plants might have expected nanomaterials.

Towards green manufacturing, an alternative strategy would be to utilize plants to synthesize non-inherent nanomaterials that they naturally don't produce during their native life cycles. Through this strategy, the disadvantages of inherent nanomaterials from plants might be overcome due to the chemical difference of the synthesized nanomaterials. More importantly, the limited types of nanomaterials acquired from plants could be greatly expanded through this process, towards real green manufacturing of desired nanomaterials.

Using plant as a carrier for metal nanoparticle production has been confirmed in intensive studies in recent years. A pilot study was introduced in 2002 using live alfalfa plants to synthesize different shape and size of gold nanoparticles [228]. Following that discovery, many live plants or plant extracts have been reported to allow the synthesis of silver, gold or other metal

nanoparticles [229-231]. These gold and silver nanoparticles exist in different shape and size from the current literature. Protein, polysaccharide, phytochemicals all have been suggested to play a role in gold or silver nanoparticle synthesis [232, 233].

However, towards actual applications, the synthesized metal nanoparticles from live plants must be extracted which normally requires the sacrifice of the live plants. Using plant extracts for the synthesis of metal nanoparticles also requires the sacrifice of plants. The requirement to sacrifice plants and the low yield in bio-synthesis of metal nanoparticles make this strategy actually less sustainable in green manufacturing although principally attractive. Also, the isolation and purification of the metal nanoparticles from plants and their extracts might be a challenge due to the complicated compounds in the original plant tissues or plant extracts [234]. Ideal strategies in the green manufacturing of nanomaterials from plants would be to minimize the above disadvantages. Secretion of nanomaterials directly from plants after their synthesis by plants doesn't require the sacrifice of the plants. Through continuous feeding the precursors and direct collection of secreted nano end-products from plants, some disadvantages of current plant-based methods might be avoided. This sustainable strategy would fit exactly the objective thus represents the direction of real green manufacturing.

In this study, two plants with secretion capacity were investigated towards this purpose. English ivy shows strong upward climbing and attachment to the solid surfaces of trees and walls of the buildings. And the secreted adhesive from

ivy rootlets contributes to this unique capacity based on the studies as early as 1876 by Charles Darwin [197], which also gets confirmed by latest nanotechnology by Zhang et al [18]. With its secretion capacity, ivy rootlet is a probable candidate towards our objective of real green manufacturing of nanomaterials. Due to the large size of English ivy in the wild fields, experiments were performed first to ensure that ivy rootlets would allow the growth of metal nanoparticles at this stage. The use of sundew plant for nanomaterial production is mainly attributed to its small size and unique secretion capacity. Sundew plant is known for its capacity of secreting adhesive on its tentacle surface, and the adhesive composition is pretty simple and clear, containing 96% of water and 4% polysaccharides or digestion enzyme [117]. Thus, synthesis followed by direct secretion of nanoparticles from sundew adhesive would be an ideal example of the nanomaterial “green-manufacturing”.

Materials and Methods

Chemicals and plants

Silver nitrate (AgNO_3) and hydrogen tetrachloroaurate ($\text{HAuCl}_4 \cdot 3\text{H}_2\text{O}$) were purchased from Acros Organics (New Jersey). Sundew plants were purchased from Black Jungle Terrarium Supply (Turner Falls, MA). English ivy rootlets were provided by David Gilmore. Dialysis membrane (molecular weight cutoff (MWCO): 300,000 Dalton) was purchased from Spectrum Laboratories, Inc

(Rancho Dominguez, CA). Qtracker 565 non-targeted quantum dots were purchased from Invitrogen (Eugene, OR).

Preparation of ivy rootlet extract solutions

English ivy rootlets were collected from the ivy farm owned by David Gilmore and shipped by flight to the University of Tennessee, Knoxville campus. The received ivy rootlets were washed three times with deionized water to remove contaminations during growth, collection and transportation. The rootlets with residual water were then smashed with clean tweezers with hard push for 3-5 min. The brown solution was then collected and centrifuged at 4,400 rpm for 5 min to remove tissue residuals. The light brown supernatant was transferred to a dialysis bag and dialyzed overnight in deionized water. The water from the outside bag was collected and labeled as solution I. The solution inside dialysis bag was labeled as solution II. To remove proteins from the solution after dialysis, the solution II was further added trichloroacetic acid (TCA) at a ratio of 1:4 (v/v), and incubated at 4°C for 10 min. Following incubation, the solution was centrifuged at 14,000 rpm for 5 min. The supernatant was collected and was labeled as solution III. The prepared solutions (I-III) were stored in a refrigerator at 4°C for further studies.

Biosynthesis of gold crystals from ivy rootlet extracts

To synthesize gold crystals from ivy rootlet extract solutions, 500 µl of each solution (I-III) was transferred into a clean eppendorf tube. 2.5 µl 100 mM

HAuCl₄·3H₂O solution was added to the tubes and mixed by brief vortexing. The solutions were then remained overnight at ambient temperature. The solutions were first examined under UV/Vis spectroscopy for the detection of gold crystal synthesis. To check the morphology of the synthesized gold crystals, the solutions were then centrifuged at 14,000 rpm for 5 min. The supernatants were removed and the pellets were washed with 1 ml deionized water. The supernatant was dumped and the pellets with residual water were dispersed by flapping the tube with fingers. 10 µl of each solution were then deposited onto clean silicon wafer surface and dried overnight under a clean-air chamber.

UV/Vis spectroscopy study

UV/Vis spectroscopic measurement of the synthesized gold crystals was carried out on a Thermo Scientific Evolution 600 UV/Vis spectrophotometer operated at a resolution of 1 nm.

DLS analysis of gold crystals

To examine the size distribution of gold nanoparticles synthesized from ivy rootlet extract solutions, the synthesized gold nanoparticles were centrifuged at 14,000 rpm for 5 min, then resuspended in 1 ml deionized distilled water. The size distribution of the synthesized gold crystals was measured with 12 repeats in each cycle using a Malvern Zetasizer® Nano ZS (Worcestershire, UK) dynamic light scattering (DLS) system with the Zetasizer® software.

Biosynthesis of silver nanoparticles in live sundew plant

For the biosynthesis of silver nanoparticles, 10 ml 200 ppm AgNO_3 was fed to the live sundew plant every 24 hours for 6 days. The sundew plant was grown under normal conditions without special care. For comparison, another sundew plant fed with deionized water was placed side-by-side. After 6 days, the sundew adhesives were sampled by gentle touching with small pieces of clean silicon wafer. The plants were then plugged out of the pots and their roots were washed to remove soil. Different parts of plants including root, stem and leaf were then cut into ~1 mm thin pieces with clean razors. Some tentacles were also transferred to clean silicon wafer surface. The as-prepared samples were then allowed to dry in a clean-air chamber for at least 24 hours prior to further analysis.

Tracking of fluorescent quantum dots in live sundew plant

To track the transportation of nanoparticles inside sundew live plant, 10 ml 2 nM fluorescent quantum dots were fed to the plant every 24 hours for 6 continuous days. The sundew plants were grown under normal conditions without special care. For comparison, another sundew plant fed with the same volume of deionized water was placed side-by-side. After 6 days, the sundew adhesives were sampled by gentle touching with transparent coverslips. The plants were then plugged out of the pots and their roots were washed to remove soil. Different parts of plants including root, stem and leaf were then cut into ~1 mm thin pieces with clean razors. Some tentacles were also transferred to clean

coverslips. The as-prepared samples were then examined for the presence of fluorescence using an Olympus Fluoview 1000 confocal microscope.

SEM analysis of gold or silver particle structure

To examine the gold crystals synthesized from ivy rootlet extract solutions, the samples prepared on silicon wafer were directly examined using LEO 1525 high resolution FE-SEM system equipped with an energy dispersive X-ray spectrometer (EDS) for elemental microanalysis. To examine the silver nanoparticles from live sundew plant, the prepared sundew samples were examined under the same system. The EDS elemental analysis was also performed to confirm that the detected particles were actually gold or silver.

Results and Discussion

UV/Vis spectroscopy of gold crystals from ivy rootlet extracts

Ivy rootlets can produce a large amount of nanoparticles for attachment. They may also be intentionally utilized towards the synthesis of metal nanoparticles. As reported previously, ivy rootlets contain a large amount of polyphenol [198, 199]. Polyphenol has excellent reducing ability and been reported to facilitate the synthesis of silver and gold nanoparticles through an energy-free route [234]. It is thus expected that polyphenol-containing extracts from ivy rootlets own the same capacity to synthesis gold or silver nanoparticles, which was tested first in this study.

Addition of $\text{HAuCl}_4 \cdot 3\text{H}_2\text{O}$ solution to the ivy rootlet extract solutions (I-III) led to the original brown color darker or turn to reddish after overnight incubation. This normally indicates the formation of gold crystals. The UV/Vis absorption spectra were measured and the characteristic surface plasmon resonance (SPR) band of gold crystals with λ_{max} at around 500-600 nm was observed in all three solutions (Figure 30). The observed spectra from solutions I and II concluded that the solutions from both inside and outside dialysis bags could allow the synthesis of gold crystals. Since dialysis bag has a MWCO value of 300,000 Dalton, different size of biomolecules might thus be responsible for the gold crystal synthesis in each solution. The observed spectra from solution II might also be attributed to a trace amount of small biomolecules that remained inside the bag after dialysis. The solution III after TCA precipitation also showed the success of gold crystal synthesis. This means that protein removal didn't affect ivy rootlet extract solutions to synthesize gold crystals, indicating that molecules other than proteins might be involved in the synthesis of gold crystals.

Structures of gold crystals from ivy rootlet extracts

To determine the structures of synthesized gold crystals, the samples were drop-deposited onto clean silicon wafer surface, air-dried overnight, and followed by the SEM examination. In the SEM images, gold micro- or nano- crystals were found from all three samples (Figure 31). These gold crystals showed different shape and size in each sample. In the sample from ivy rootlet extract Solution I, the binominal distribution of the gold crystal size could be clearly observed

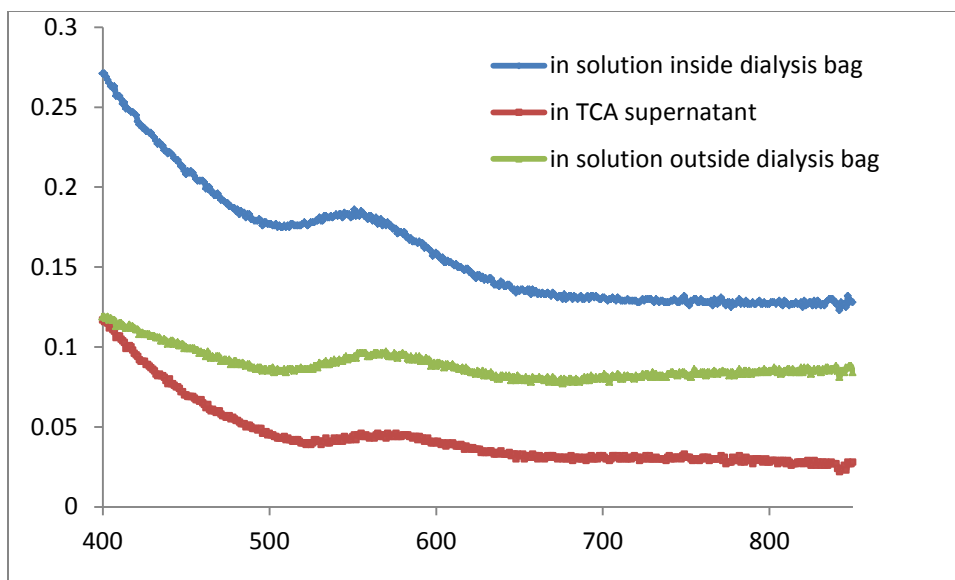


Figure 30 UV/Vis spectra of gold crystals from ivy rootlet extracts.

(Figure 31a and 31b). More crystals with size over 200 nm were observed at a large scale (Figure 31a), while a closer look at a small scale indicated the existence of particles smaller than 100 nm (Figure 31b). Size distribution of gold crystals from DLS measurements agreed well with the observations from SEM detection (Figure 32a). In the sample from ivy rootlet extract solution II, crystals with size over 200 nm were observed in less density, and more small gold nanoparticles (AuNPs) were detected (Figure 31c and 31d). The DLS data also demonstrated a higher density of smaller AuNPs in solution II (Figure 32b). In the sample from ivy rootlet extract solution III, clear difference could be observed in the SEM micrographs compared to the other two samples. More nanoplates in triangle or hexagon shapes with diameters over 100 nm were observed, coexisting with other regular shapes of crystals over 100 nm, such as pentagon or cubic crystals (Figure 31e and 31f). Compared to the other two samples, much less spherical AuNPs could be observed in the SEM images. And the DLS data also suggested that bigger sizes of the crystals in the solution III (Figure 32c).

The mechanism that controls the observed different structure of gold crystals is not clear at this moment, and different theories might offer assistance with the explanation of the observed phenomena. Since the shape and structure of gold crystals are related to the reducing potential of the reagents [235], it is believed that there are different molecules existing in the extract solutions that allow the formation of different type of gold micro- and nano-crystals. Another possible explanation is that the same chemical might be responsible for the

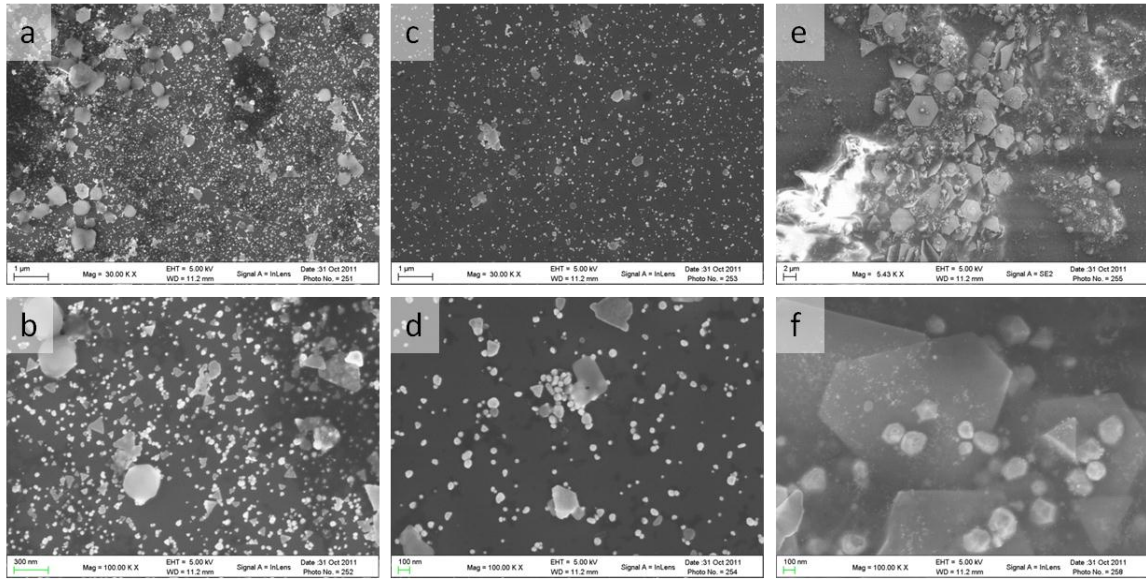


Figure 31 SEM images for the gold crystals from ivy rootlet extract solutions.

Gold crystals synthesized from solution I (a, b), II (c, d) and III (e, f).

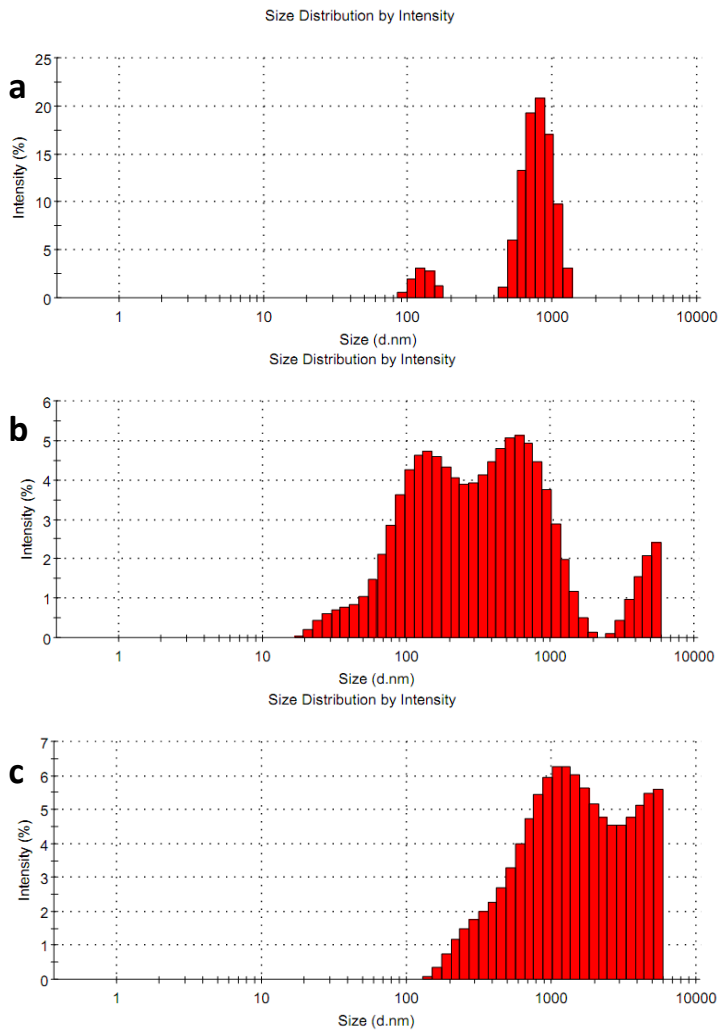


Figure 32 Size distribution of gold crystals synthesized by ivy rootlet extracts.

(a) DLS data of the gold crystals by the ivy rootlet extract solution I. (b) DLS data of the gold crystals by the ivy rootlet extract solution II. (c) DLS data of the gold crystals by the ivy rootlet extract solution III.

synthesis of gold crystals. However, due to its different concentrations among the three prepared solutions, the dynamic process of the gold crystal synthesis thus caused the formation of different crystals [236]. The third possibility is that different pH of the solution III might affect the synthesis of Au crystals [237].

Silver nanoparticle production from live sundew plant

To synthesize silver nanoparticles in live sundew plant, the precursor chemical silver nitrate (AgNO_3) was fed to the sundew plant for over 6 days. Different parts of the sundew plant were then examined for the silver nanoparticle production, especially the adhesive secreted from the tentacles of the plant. As shown in the SEM micrograph in Figure 33a, silver nanoparticles could be detected in the stem of the sundew plant. However, in other parts of the sacrificed sundew plant, no obvious metal nanoparticles could be observed, including the secreted adhesive or secreting tentacles. To further confirm that the observed nanoparticles were silver nanoparticles but not other plant organelles or tissue structures, EDS analysis was performed in the examined nanoparticles. As shown in Figure 33b, Ag peak emerged in the spectra from EDS analysis, while C and O peaks were also observed. The observed carbon and oxygen likely came from the fibers of the plant tissue in the examination. In other parts of the plant where no metal nanoparticles were detected, no obvious Ag peak was observed in the DES spectra, further suggesting that the detected nanoparticles in the stem were truly silver nanoparticles. These observations support that the live sundew plant could serve a source for silver nanoparticle production.

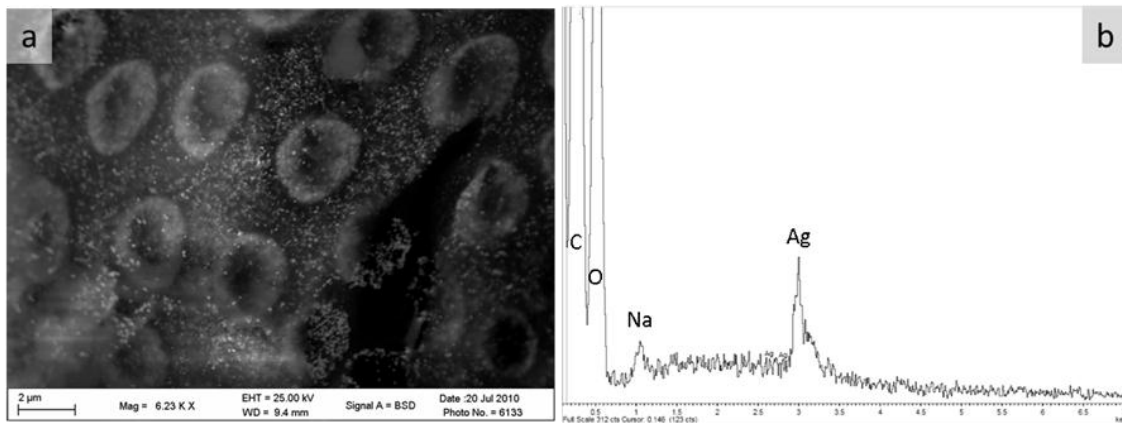


Figure 33 Confirmation of silver nanoparticle synthesis in sundew stem.

(a) SEM micrograph of the synthesized silver nanoparticles. (b) EDS spectra of the silver from the sundew stem.

Tracking of nanoparticle translocation in sundew plant

Silver nanoparticles existed in the stem but no other parts of the sundew plant suggested that silver nanoparticles could be synthesized in the stem, but not in other parts of the sundew plant. However, the observation also indicates limited transportation of silver nanoparticles inside sundew plant. Although one study from maize reported no obvious translocation of cerium dioxide nanoparticles inside the plants [238], the studies from other plants support that once nanoparticles entered into the vascular cylinder, they could move smoothly to the end of the vascular bundle along with the water flow inside plant [239, 240]. To track actual nanoparticle translocation and spreading throughout the sundew plant, fluorescent quantum dots were used to track the distribution of nanoparticles inside sundew plant. 15 nm fluorescent quantum dots were fed to the soil in the pot for 6 days, then the presence of fluorescent quantum dots were examined using laser scanning confocal microscopy. As shown in Figure 34, fluorescence was clearly observed in the stem but no other parts of the plant. The accumulation of nanoparticles in sundew stem suggested an existence of different tissue structure in sundew stem that might block the transportation of nanoparticles to other parts of plant. The limited translocation of nanoparticles in sundew plant thus prevented the movement and direct secretion of the synthesized silver nanoparticles through its tentacles. Although no expected results were obtained to use sundew plant as the green manufacturing factory in this study, our recent progress in cultured ivy shoots suggested an alternative

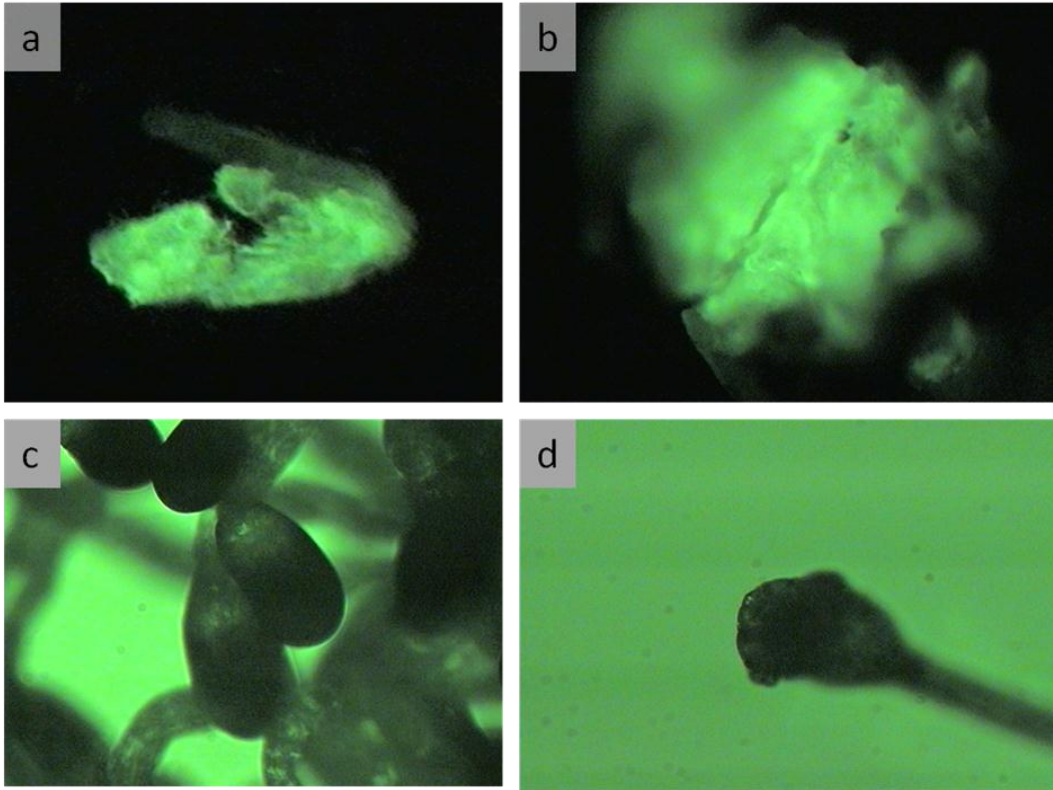


Figure 34 Confocal microscopy images of stem and tentacles of sundew plant fed with fluorescent quantum dots.

(a, b) Fluorescence images of stem pieces. (c, d) Fluorescence images of tentacles.

strategy to synthesize metal nanoparticles without the sacrifice of the live plants. Also, other plants with liquid-secreting capacity are being searched and investigated towards the goal of “synthesis-secretion” strategy.

Conclusions

In this study, the methods towards biosynthesis of metal nanoparticles from live plant or plant extracts were investigated. It was found that ivy rootlet extract solutions with or without further treatments allowed the formation of gold micro- and nano-crystals in different shape and size. Nanoplates were also synthesized in the extract solution after dialysis and TCA precipitation treatments. Except ivy rootlet extracts, live sundew plant was also investigated in the synthesis of metal nanoparticles. Silver nanoparticles could be synthesized in the stem but no other parts of live sundew plant. In addition, the synthesized silver nanoparticles were restricted to the stem, and couldn't be translocated to other parts of the plant. The limited transportation of nanoparticles in live sundew plant was further confirmed by tracking fluorescent quantum dot distribution inside plant. Overall, the successful synthesis of gold and silver nanoparticles from ivy rootlet extracts and live sundew plant suggests plants can play an active role in the green manufacturing of nanomaterials.

**CHAPTER VIII. ONE-STEP SIZE-CONTROLLED
SYNTHESIS OF GOLD NANOPARTICLES WITH
SURFACTANT-MODIFIED SURFACE PROPERTIES**

Introduction

Gold nanoparticles (AuNPs) have attracted great attention in the past decades due to their unique electronic, optical, thermal, and catalytic properties and their potential applications in the fields of physics, biology, chemistry and medicine including imaging, diagnosis, drug delivery and photo-thermal therapies [241-243]. To accommodate these applications, the research has been focused on the synthesis of different shape, size of nanoparticles with or without further conjugation of functional molecules. One example is to coat the synthesized AuNPs with modified polyethylene glycol (PEG) to enhance the biocompatibility of the AuNPs. Another example is to use different membrane structure to form various shape and size of nanoparticles [235]. However, these methods normally require the complicated design and separate seeding and growth steps under different conditions. More importantly, these newly-developed methods still rely on the two basic approaches, Turkevich-Frens and Brust-Schiffrin methods [244, 245]. In the Brust-Schiffrin method, AuCl_4^- is transferred into toluene or chloroform using tetraalkylammonium bromide and reduced with sodium borohydride (NaBH_4) in the presence of alkylthiols. The synthesized nanoparticles through this method are relatively small, normally less than 10 nm, and these AuNPs are covered with strongly bound ligands that render them difficulty to disperse in water and hinder further modification and functionalization for practice applications. Turkevich-Frens method uses citrate and ascorbic acid as reducers to synthesize nanoparticles, and the synthesized nanoparticles are

typically larger, from 9 to 120 nm. However, the initiation of reduction requires assistance of externally supplied energy, such as photo-irradiation, ultrasound irradiation, or heating [246-249]. A simple and versatile procedure for the preparation of wide range size and shape of AuNPs under ambient temperature would be a challenging but intellectually rewarding task.

One of the efforts in recent years is the utilization of green synthetic strategies to produce AuNPs, and many naturally existing materials have been employed to synthesize “green” AuNPs. Polysaccharide, e.g. chitosan and sucrose, have reported to be utilized as reducing and stabilizing agents for the synthesis of AuNPs [250, 251]. However, the synthesized AuNPs normally have a high variety in shape and size in the mixture. Due to the gentle nature of the chemicals in these green manufacturing, harsh chemical treatment to control size and shape of the synthesized nanoparticles becomes challenge, which makes this strategy less attractive. Thus, it is desirable to search for proper reducing and capping agents that can synthesize AuNPs with wide range of size and shape under mild conditions, especially when the method is simple while the synthesized AuNPs still show homogeneous structures with expected functions.

One of possible candidates is the (co-)polymer which has already showed multifunctionality in the control of AuNP synthesis, such as poly(ethylene oxide)-poly(propylene oxide) (PEO-PPO) block copolymer [252]. Surfactant is also a polymer that has been widely used as a capping agent to exert exquisite control over the nucleation and growth of gold nanocrystals [253]. One example is

cetyltrimethylammonium bromide (CTAB) as templating or structuring media in the synthesis of gold nanorods in the solution [254]. Another well-studied example is thiol-PEG, which has been exploited to increase biocompatibility and stability of the synthesized AuNPs in drug delivery [255]. Organosilicone surfactants, excellent penetrators widely used for herbicides, show very similar structures as PEG, thus have a potential to work as a capping agent in AuNP synthesis. More importantly, organosilicone surfactants have been reported as reducing agents for platinum and other metal production [256], but have not been utilized for the synthesis of metal nanoparticles. Thus, organosilicone has a potential to work as both reducing reagent and stabilizer simultaneously in the synthesis of AuNPs, which has not been reported in the open literature.

The use of organosilicone surfactants in the AuNP synthesis is not only principally feasible, but also attractive considering their unique properties. Due to their highly lipophilic property, organosilicone surfactants have been used as excellent additives in the drug delivery. The incorporation of the lipophilic organosilicone substituent into the drugs has been proved to enhance blood stability, increase cell penetration and improve pharmacokinetics [257]. The coating of AuNPs with organosilicone would be especially useful for *in vivo* applications since the administrated nanoparticles without proper surface modifications will be eliminated by the human reticulo-endothelial system within seconds to minutes [258]. The coating of organosilicone surfactants will likely afford long circulation property of the synthesized AuNPs by evading

macrophage-mediated uptake and removal from the systematic circulation, similar to the PEG-coated AuNPs from a recent report [259]. Silylation of drugs is also shown to increase the activity of the parent drug or prolong the duration of its action in the test. With these reasons, it is expected that the synthesized AuNPs coated with organosilicone surfactant possess some advantages in the *in vivo* transportation and stability.

Traditional methods to coat 'stealth-shielding' polymers on the AuNPs include covalent 'grafting from' (relying on polymerization), covalent 'grafting to' (using sulfur-containing polymers), physisorption and post-modification of preformed AuNPs [260]. Direct coating of the 'stealth-shielding' polymer layer during the AuNP synthesis will avoid these post modifications and the accompanying variations and chemical residuals, which will be extremely useful for *in vivo* applications. In this study, directly coating of "stealth-shielding" polymers onto AuNPs was assessed during their synthesis using organosilicone surfactant. It is the first time to exploit the capacity of organosilicone surfactant as a reducing and capping agent simultaneously in the AuNP synthesis. The results from the study confirmed the capacity of organosilicone surfactants to work as both reducing and capping agents in the synthesis of AuNPs. The present method offers obvious advantages of ambient conditions, fast completion, minimal number of reactants, being economical, and resulting in ready-to-use AuNPs with blood stability and excellent penetration capacity. Moreover, the size and shape of the formed AuNPs could be easily tuned by adding additional

reagents without changing the reaction temperature. This facile green manufacturing of biocompatible AuNPs with “steal-shielding” property make them attractive candidates in the *in vivo* applications in medicine.

Materials and Methods

Preparation of gold nanocrystals

Hydrogen tetrachloroaurate (III) ($\text{HAuCl}_4 \cdot 3\text{H}_2\text{O}$), sodium hydroxide (NaOH), silver nitrate (AgNO_3) at chemical analysis grade were purchased from Sigma-Aldrich. Silwet L-77 was acquired from Lehle Seeds. Deionized distilled water was used to prepare the proper concentration of each reagent. In a typical synthesis of gold nanocrystals, 2 ml of proper concentration of $\text{HAuCl}_4 \cdot 3\text{H}_2\text{O}$ solution was added to a 5 ml test tube, followed by the addition of 0-5 μl of Silwet L-77. For controlling the shape and size of the synthesized gold nanocrystals, NaOH and/or AgNO_3 will be added prior to the addition of Silwet L-77. After addition of each reagent to the tube, the solution was mixed immediately by vortexing. After final addition of Silwet L-77 and mixing, the tube was left on the bench for AuNP production.

Characterization

To confirm the success of gold nanocrystal synthesis, different techniques have been applied to characterize the AuNPs. The ultraviolet/visible (UV/Vis) absorbance was measured on the Thermo Scientific Evolution 600 UV/Vis Spectrophotometer (Waltham, WA). To determine the size of the synthesized AuNPs, the solution was directly measured in the Malvern Zetasizer® Nano ZS

(Malvern Instruments Ltd, Worcestershire, UK) system. To determine the morphology and structure of the synthesized AuNPs, 10 μl of solution was air-dried in a clean small piece of silicon wafer and scanned under the high resolution LEO 1525 FE-SEM equipped with a Gemini Emission Column. The energy-dispersive X-ray spectroscopy (EDS) of the detected gold nanocrystals was also measured simultaneously, to ensure the chemical properties of the detected nanocrystals. To perform Fourier transformed infrared spectroscopy (FTIR) analysis to characterize the chemical properties of the coated surface, AuNPs were washed with deionized water twice and air-dried. They were then mixed with potassium bromide, and transmission spectra were acquired with a Bruker Vertex 70 FTIR spectrometer (Bruker Optics Inc, Billerica MA), equipped with a deuterated triglycine sulfate detector and controlled by OPUS 6.5 software package. The evaluation of stability of AuNPs was performed by incubation of AuNPs with different solutions or culture media, followed by the examination of size distribution by DLS and UV/Vis spectroscopy. The endocytosis of the synthesized AuNPs was examined under the Nikon Eclipse E600 microscopy equipped with CytoVivaTM condenser, illuminated with an EXFO light source.

Results and Discussion

Facile synthesis of AuNPs in a single mixture

To test if nanoparticles could be formed using the proposed method, Silwet L-77 was added at a volume ratio of 1:1000 to 0.5 mM $\text{HAuCl}_4 \cdot 3\text{H}_2\text{O}$, a typical

concentration used for AuNP synthesis [252]. It is well known that AuNPs exhibit a characteristic Surface Plasmon Band (SPB) which appears colorful under proper media [261]. In this reaction, the solution changed from the yellow color of the $\text{HAuCl}_4 \cdot 3\text{H}_2\text{O}$ solution to a reddish color, visibly indicating the formation of nanoparticles. AuNP formation was further confirmed by analyzing the UV/Vis spectra, as shown in Figure 35a. In the figure, the UV/Vis absorption was measured every 2 min after mixing the Silwet L-77 and $\text{HAuCl}_4 \cdot 3\text{H}_2\text{O}$. Prior to mixing, no AuNP specific SPB was detected. However, after 4 min, an absorption peak with λ_{max} of 545 nm emerged, indicating the formation of nanoparticles. λ_{max} increased continually until reaching a maximum at 30 min, when one of the reactive components was consumed, and thus no further nanoparticle formation could be observed.

To examine the morphology of the synthesized AuNPs, the sample was drop-deposited onto cleaned fragments of silicon wafer and examined by scanning electron microscopy (SEM). In Figure 35c, many nanoparticles with different shapes and sizes were observed. Spherical nanoparticles were the dominant species formed, however, nano-triangles from 50-400 nm, and nano-rods with lengths from 100 to 600 nm, were also formed (Figure 35c). Since there is a one-to-one correlation between the initial seeds and final nanocrystal structures [262], the observed morphology suggests that different seeds formed at the initial stage of AuNP formation. To ensure that the nanoparticles formed were Au nanoparticles, and not the result of complexation of the Silwet L-77,

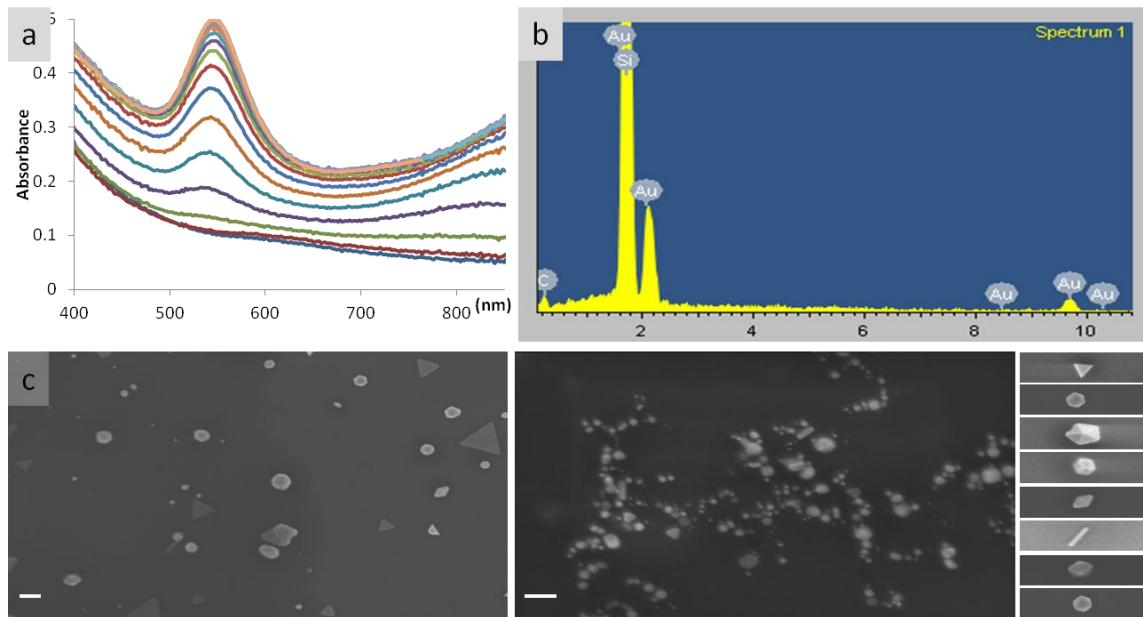


Figure 35 Confirmation of AuNP synthesis.

(a) UV/Vis absorbance during AuNP synthesis. The spectra were measured every 2 min with each line representing one measurement. (b) The EDS spectra of the AuNPs from the sample prepared on silicon wafer surface. (c) SEM images of AuNPs from different areas of the sample. Specific regular shapes of nanorod, spherical, triangular, prismatic and hexagonal shapes are shown on the right of the image. The scale bar is 200 nm.

elemental analysis of the nanoparticles was confirmed using EDS. The spectra in Figure 35b revealed that the nanoparticles were in fact Au, as demonstrated by the Au peaks. The other peaks in the EDS spectra include a major silicon peak coming from the silicon wafer substrate, and a small carbon peak, which is likely attributed to the carbon from the coated Silwet L-77.

Effect of AuCl₄⁻ and Silwet L-77 concentration on AuNP synthesis

In order to determine the dynamic response of the AuNP formation, a matrix was established to evaluate the reactions by varying concentrations. The matrix was established using Silwet L-77 at a final concentration of 0.005%, 0.025%, 0.05%, 0.1% and 0.25%, and HAuCl₄·3H₂O solution at concentrations of 0.05, 0.1, 0.2, 0.5, 1, 5 and 10 mM. After the solutions were mixed vigorously using a vortexer, they were analyzed by UV/Vis spectroscopy. It was found that the SPB band emerged most rapidly with the highest concentration of Silwet L-77 tested, 0.25% (Figure 36a). At this Silwet L-77 concentration, with the HAuCl₄·3H₂O concentration maintained at 0.5 mM, the λ_{\max} the AuNP SPB band reached an absorbance value of 1 in less than 5 minutes, while the lower concentrations tested, 0.05 and 0.025% did not reach this absorbance value during the 50-80 minute monitoring. Similarly, by maintaining the Silwet L-77 value at 0.1%, the SPB band emerged the fastest with a HAuCl₄·3H₂O concentration of 0.5 mM (Figure 36b). Interestingly, a threshold effect showed both slower emergence and decreased maximum absorbance from the SPB band at concentrations both below and above 0.5 mM (Figure 36b).

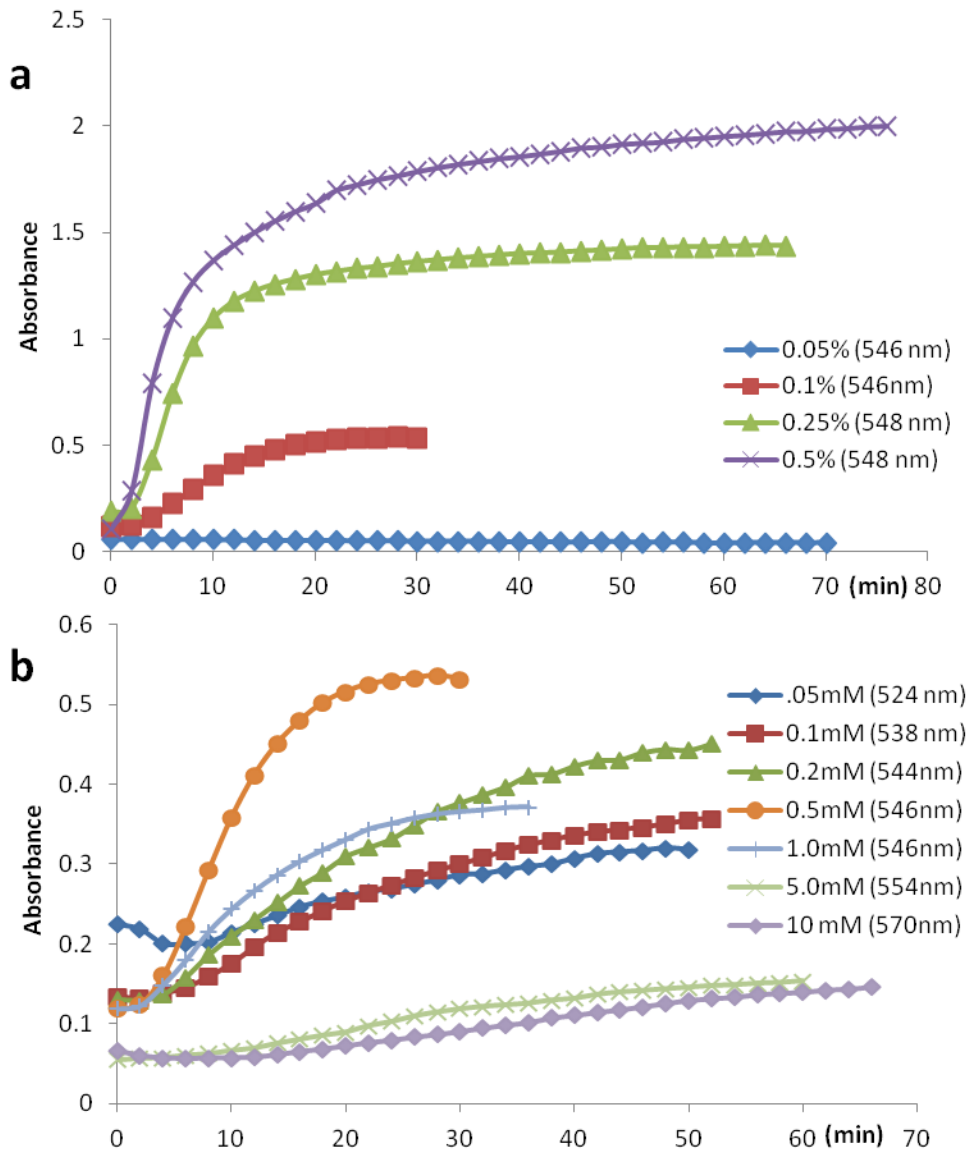


Figure 36 Tracking of λ_{\max} of AuNP SPB with time.

(a) The change of λ_{\max} with time for the samples under different concentration of Silwet L-77 with fixed concentration of 0.5 mM $\text{HAuCl}_4 \cdot 3\text{H}_2\text{O}$. (b) The change of λ_{\max} with time for the samples under different concentration of $\text{HAuCl}_4 \cdot 3\text{H}_2\text{O}$ with fixed concentration of 0.1% Silwet L-77. The value inside parenthesis represents the λ_{\max} under each condition.

To determine the effect of various concentrations of reagents on the size and stability of the synthesized AuNPs in solution, DLS and Zeta potential analysis were conducted for all samples within the matrix (Table 2). As the concentration of $\text{HAuCl}_4 \cdot 3\text{H}_2\text{O}$ increased, the size of the nanoparticles also increased. A similar trend was not observed when increasing the concentration of Silwet L-77. At the highest concentration (0.25%) of Silwet L-77 tested, the data was only valid for the 0.5 mM $\text{HAuCl}_4 \cdot 3\text{H}_2\text{O}$ sample, indicating either too few nanoparticles, or too polydisperse of AuNPs for analysis in the other samples. Similarly, for all the samples with $\text{HAuCl}_4 \cdot 3\text{H}_2\text{O}$ greater than 0.5 mM, no data could be obtained from the DLS due to the polydispersity of the samples. Based on the data obtained from the DLS and UV/Vis analysis, SEM was conducted to determine changes in the morphology of the nanoparticles with an increasing concentration of $\text{HAuCl}_4 \cdot 3\text{H}_2\text{O}$. A Silwet L-77 concentration of 0.1% was used to synthesize nanoparticles with increasing concentrations of $\text{HAuCl}_4 \cdot 3\text{H}_2\text{O}$. At low concentrations of $\text{HAuCl}_4 \cdot 3\text{H}_2\text{O}$ (0.05-0.3 mM), disperse nanoparticles could be observed, with a variety of sizes and morphology (Figure 37a-b). At a concentration of 0.5 mM, the concentration of nanoparticles seemed to increase, although the morphology of the nanoparticles was still highly variable (Figure 37c). At concentrations of 1 mM and above, the SEM analysis appeared more like a fibrous polymer and it was difficult to distinguish individual nanostructures (Figure 37d-e). This data is in accordance with the DLS data, where it was not possible to get reliable data above a $\text{HAuCl}_4 \cdot 3\text{H}_2\text{O}$ concentration of 1 mM. The

Table 2 Size of AuNPs measured by DLS.

| AuNP Size | | Concentration of AuCl ₄ ⁻ (mM) | | | | | | | |
|-----------------|--------------|--|------------|------------|------------|------------|----------|-----------|-----|
| (nm) | <u>0.05</u> | <u>0.1</u> | <u>0.2</u> | <u>0.3</u> | <u>0.4</u> | <u>0.5</u> | <u>2</u> | <u>10</u> | |
| Silwet L-77 (%) | <u>0.005</u> | 84.88 | 101.7 | 113.2 | 128.0 | 126.7 | N/A | N/A | N/A |
| | <u>0.025</u> | 86.95 | 86.37 | 125.6 | 147.7 | 148.5 | 143.8 | N/A | N/A |
| | <u>0.05</u> | N/A | 85.56 | 125.3 | 146.4 | 147.8 | 139.2 | N/A | N/A |
| | <u>0.1</u> | N/A | N/A | 101.9 | 130.7 | 146.1 | 137.2 | N/A | N/A |
| | <u>0.25</u> | N/A | N/A | N/A | N/A | N/A | 128.4 | N/A | N/A |

Note: N/A means no data reported during the DLS measurement due to too few or too polydisperse nanoparticles present in the sample.

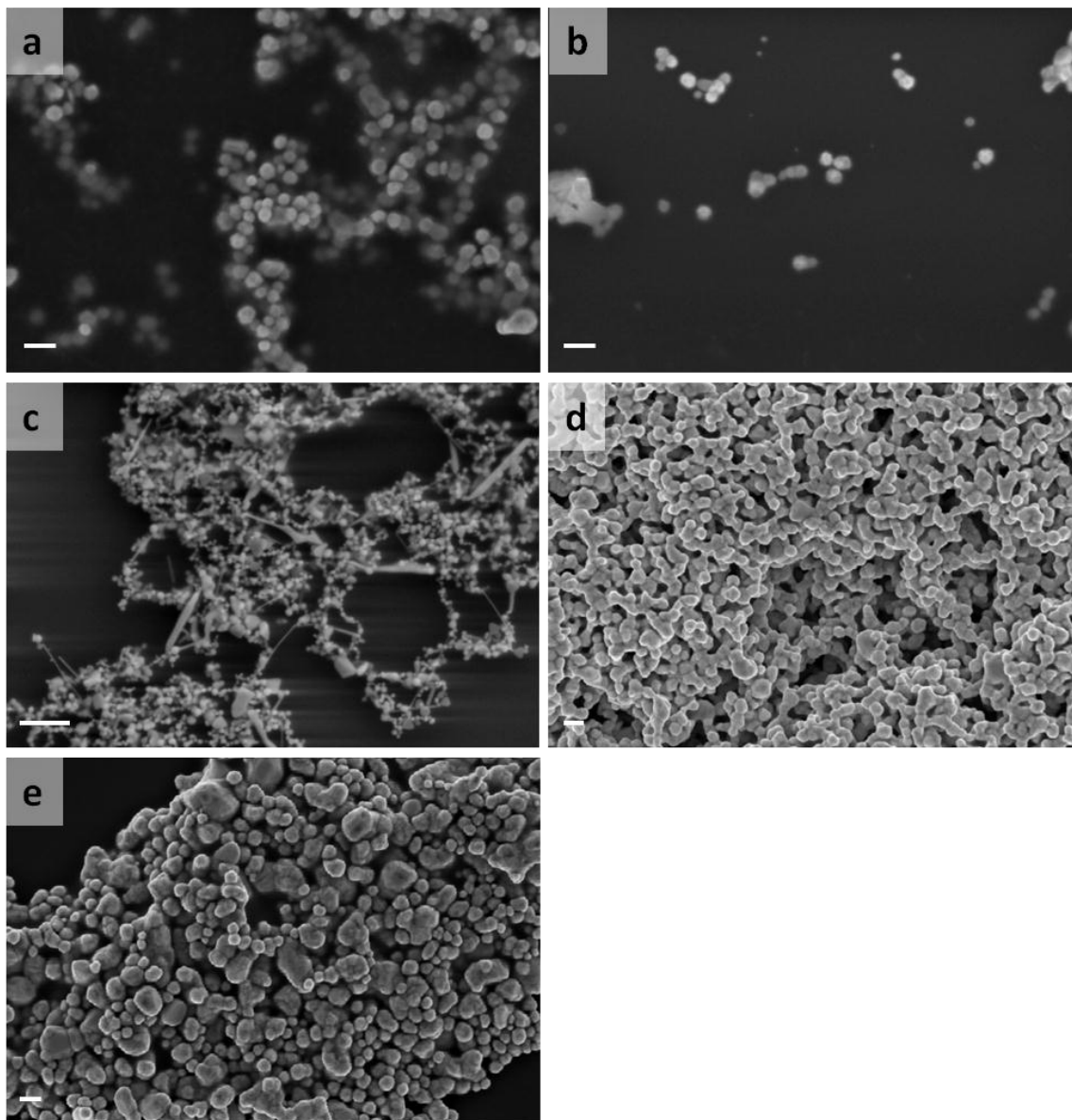


Figure 37 AuNPs under different concentration of HAuCl₄·3H₂O.

SEM micrographs for the AuNPs synthesized under 0.1% Silwet L-77 and an increased concentration of HAuCl₄·3H₂O at 0.1 mM (a), 0.3 mM (b), 0.5 mM (c), 2 mM (d), and 10 mM (e). Scale bar = 200 nm.

dense structure of this nanomaterial clearly contributed to the lack of reliable DLS data in these samples, and caused them to sediment more rapidly than the lower $\text{HAuCl}_4 \cdot 3\text{H}_2\text{O}$ concentrations.

Morphological control of AuNPs by NaOH

As the function of AuNPs depends on their shape and size, a mixture of AuNPs with different shapes and sizes formed from the proposed method is not desirable for most applications. Since the ratio of Silwet L-77 to $\text{HAuCl}_4 \cdot 3\text{H}_2\text{O}$ alone was not able to form homogeneous AuNPs, other factors were explored to control the shape and size of AuNPs. Previously, NaOH has been reported to assist with the synthesis of uniform AuNPs, and was tested in this study [263]. To determine the ability of NaOH to control the size and shape of AuNPs, NaOH was added to a final concentration of 3 mM in a solution of 0.1% Silwet L-77 and 0.5 mM $\text{HAuCl}_4 \cdot 3\text{H}_2\text{O}$. Figure 38a shows the real-time monitoring of UV/Vis absorption with or without NaOH. In Figure 38a, the black lines represent the absorption with NaOH, while the red lines represent the absorption without the addition of NaOH. It was found that the addition of NaOH greatly inhibited the speed of AuNP synthesis.

With the addition of NaOH and the decreased rate of AuNP synthesis, the size of the AuNPs became homogeneous, as demonstrated by SEM imaging. As shown in Figure 38, without NaOH, nanorods, cubic, triangular, or other nanoparticles were detected (Figure 38b). However, with the addition of NaOH, only homogeneous spherical nanoparticles were present (Figure 38c). The

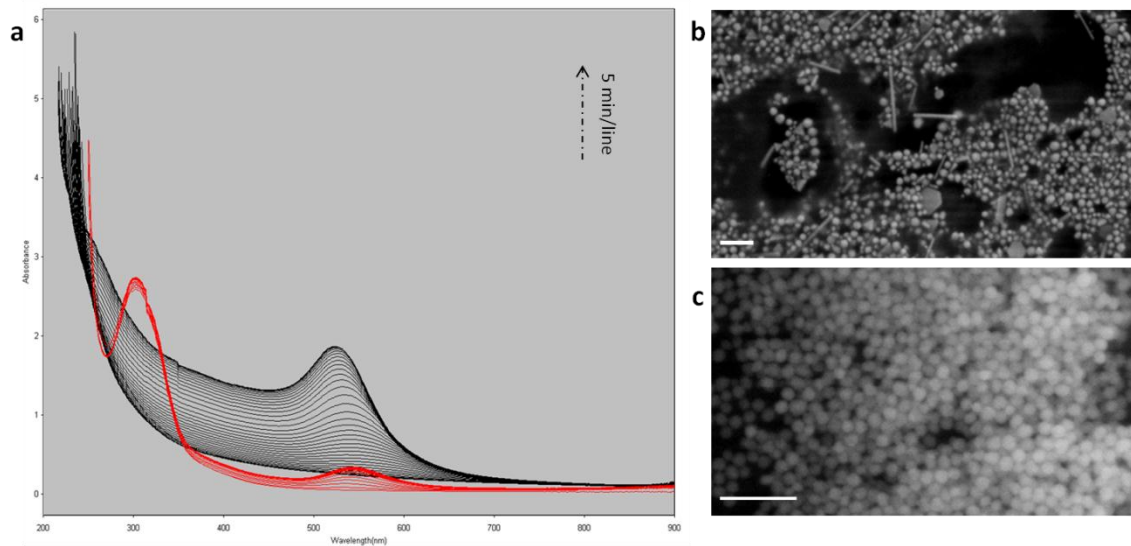


Figure 38 NaOH led to the homodispersion of AuNPs.

(a) Real-time monitoring of the AuNP synthesis without (red lines) or with (black lines) NaOH. (b, c) The SEM micrographs of the AuNPs without or with the addition of NaOH. Scale bar = 200 nm.

possible role of NaOH in the AuNP synthesis is due to its reactivity with Au complexes. As shown in Figure 38a, without addition of NaOH, an absorption peak at 310 nm could be clearly observed throughout the AuNP synthesis. However, after addition of NaOH, the absorption peak at 310 nm disappeared immediately, which suggests that a different form of Au complexes might be formed, but not reduced to Au⁰.

Size-controlled synthesis of AuNPs by AgNO₃

Silver nitrate has been reported to have a dramatic effect on the final shape and crystalline structure of synthesized AuNPs [264]. It has previously been used to tune the shape of polyhedral AuNPs without the need for seeds [265]. In this study, the role of AgNO₃ in controlling AuNP synthesis using the proposed method was investigated. As the addition of NaOH was found to aid in the synthesis of homogeneous AuNPs, AgNO₃ was added to the reaction solution containing NaOH. The addition of AgNO₃ to our reaction mixture did not tune the shape of AuNPs to nanorods or polyhedral particles as indicated in other reports, but rather further inhibited crystal growth and decreased the size of the synthesized AuNPs [264, 265]. The AuNP size further decreased with increasing concentrations of AgNO₃, as shown in Figure 39. When AgNO₃ was added to a final concentration of 0.5, 1 and 2 ppm, the size of AuNPs had a corresponding diameter of 54, 40 and 33 nm, determined by DLS (Figure 40). With an AgNO₃ concentration of 10 ppm, two peaks emerged by DLS, a small peak at 1.3 nm and a larger peak at 19 nm. These small AuNPs began to cluster, as shown in

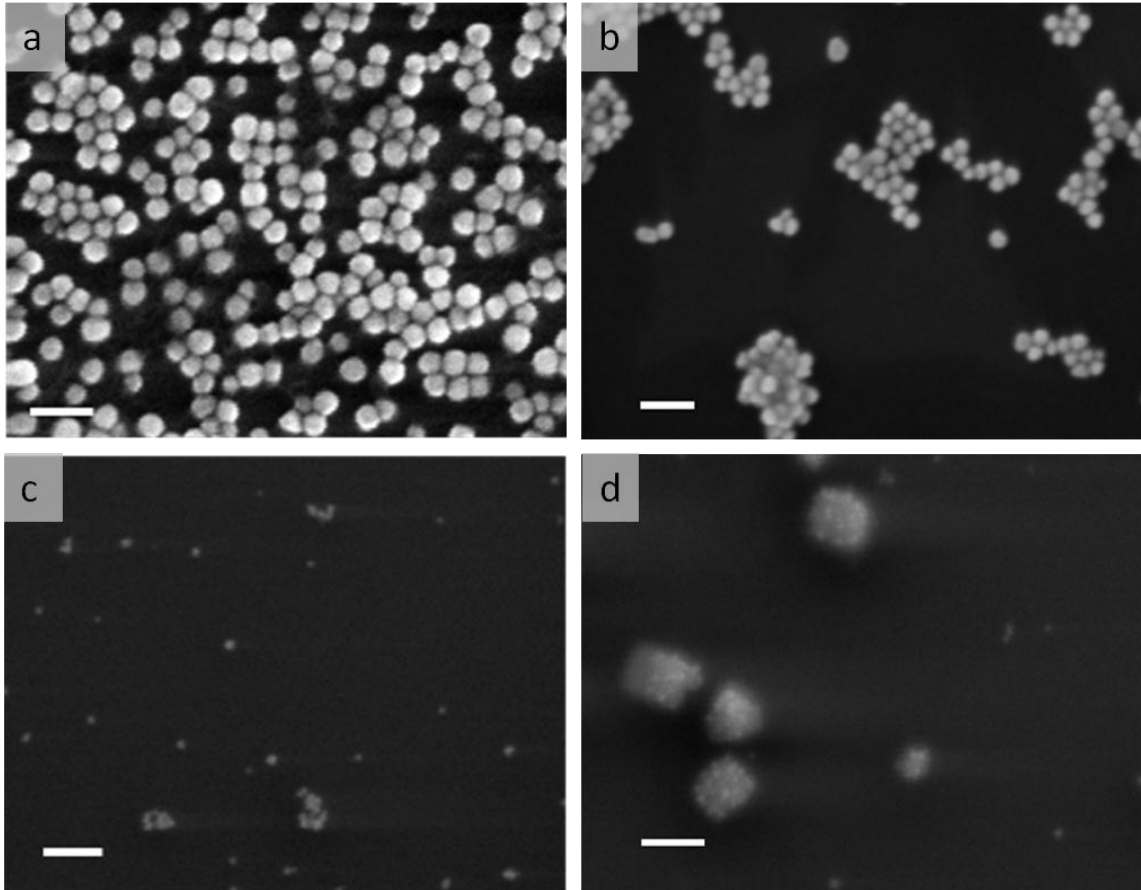


Figure 39 AgNO_3 led to the decreased size and increased clustering of AuNPs.

(a-d) SEM micrographs of AuNPs with AgNO_3 concentration of 0, 2, 10 and 40 ppm. Scale bar = 100 nm.

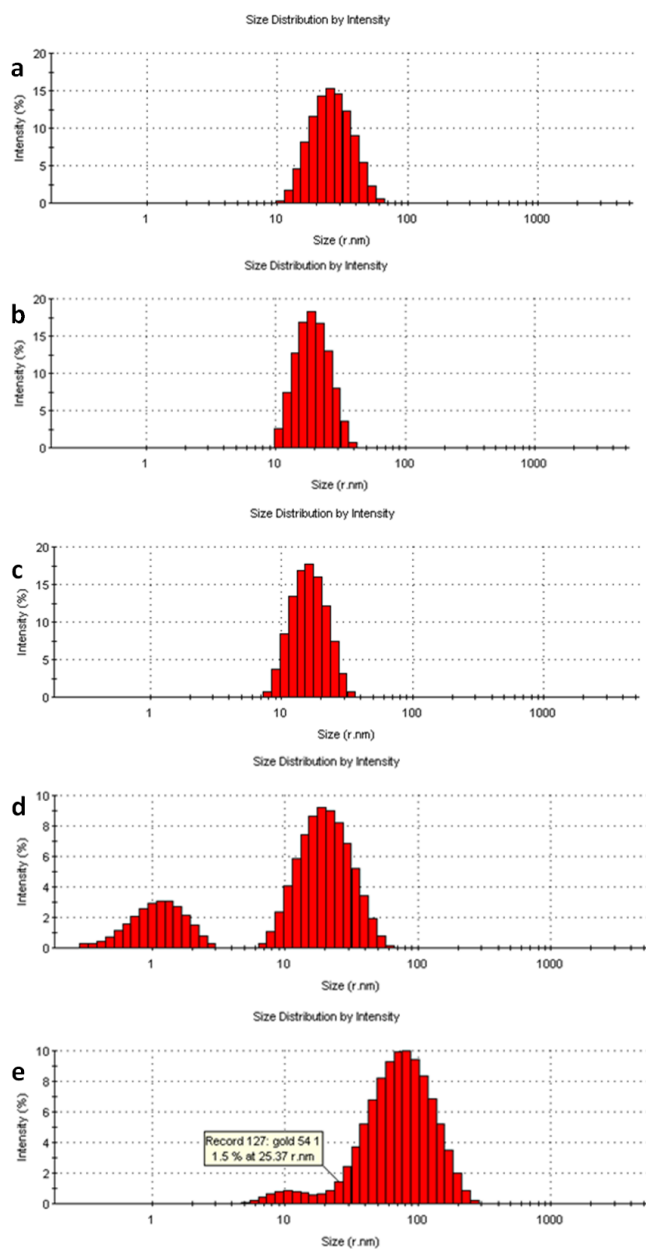


Figure 40 DLS data for the AuNPs under different concentration of AgNO₃.

DLS data for the samples with 0.1% Silwet L-77, 0.5 mM HAuCl₄·3H₂O, 3 mM NaOH and 0.5 ppm (a), 1 ppm (b), 2 ppm (c), 10 ppm (d) and 40 ppm (e) of AgNO₃.

Figure 39c-d and Figure 40d-e, and at an AgNO_3 concentration of 40 ppm, the clusters dominated and a major cluster peak of 78 nm with a left shoulder peak was observed by DLS. The mechanism used by AgNO_3 to decrease the size of AuNPs is likely due to its role as a stabilizer to slow down the growth of the gold nanostructures, as indicated in previous studies [266, 267].

FTIR analysis of AuNPs

To determine if the AuNPs were coated by Silwet L-77, FTIR was performed to analyze the chemical structure of the AuNP surface. Since the coated layer comprised only a small part of AuNPs, the signal was not strong and the absorption peaks were low, similar to the reports from other studies about the polymer structures coated on AuNP surfaces [268]. However, these peaks remained consistent during repeated measurements with various concentrations of AuNPs. Based on the spectra in Figure 41, multiple peaks were identified, including an absorption peak at 1090 nm which corresponds to the C-O bonds for Silwet L-77, a peak at 1400 nm indicating the $-\text{CH}_3$ group at the ends of the Silwet L-77, and a peak at 1640 nm indicating the acyclic C-C bonds for Silwet L-77. This data, combined with carbon peak from EDS study, confirms that the AuNPs were at least partially coated on the surface by the Silwet L-77 surfactant.

Stability and endocytosis of the AuNPs

The successful synthesis of different sized spherical AuNPs leads to their potential applications in medicine. Stability of AuNPs under physical conditions is

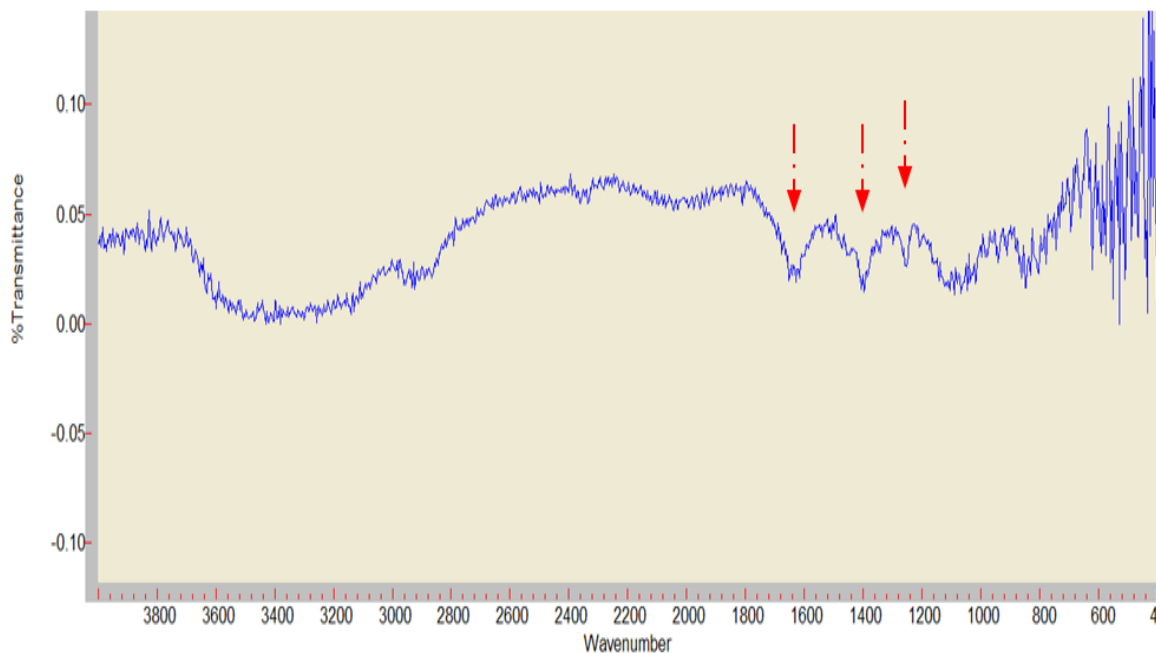


Figure 41 FTIR of AuNPs.

The red arrows point to the peaks of 1090, 1400 and 1640 nm which correspond to the C-O bond, -CH₃ group and C-C bond for Silwet L-77.

important if they are to be employed in biological and medical applications, because they are generally performed in the presence of buffering and serum solutions. UV/Vis spectroscopy was used to monitor the aggregation, precipitation and decomposition of AuNPs with changes in pH. Homogeneous AuNPs were incubated under different pH conditions or with phosphate buffered saline (PBS). These AuNPs showed excellent stability under the pH range of 4.8 to 12, the normal physiological pH values in cellular environment, although these AuNPs showed instability below pH 3 (Figure 42a). Similarly, almost no change was observed after the incubation of AuNPs with PBS, as shown in the UV/Vis spectra in Figure 42b.

To determine if the AuNPs were able to pass through cell membrane, the homogeneous AuNPs synthesized with NaOH but without AgNO_3 were incubated with the MC3T3 cell line. After incubating for 4 hours, the cells were washed 4 times with PBS and incubated in fresh media overnight. The cells were then examined for the endocytosis of AuNPs using dark-field light microscopy. Due to localized surface plasmon resonances, AuNPs have large optical scatterings at 500-600 nm wavelengths [269]. Using the CytoViva™ imaging system, AuNPs can be easily distinguished from cellular organelles [270]. As shown in Figures 43 and 44, a clear difference could be observed between cells incubated with or without AuNPs. In the cells incubated with AuNPs, bright spots were observed from the scattering of the AuNPs, which couldn't be observed in the control cells. Scanning over different cellular heights further confirmed that the AuNPs were

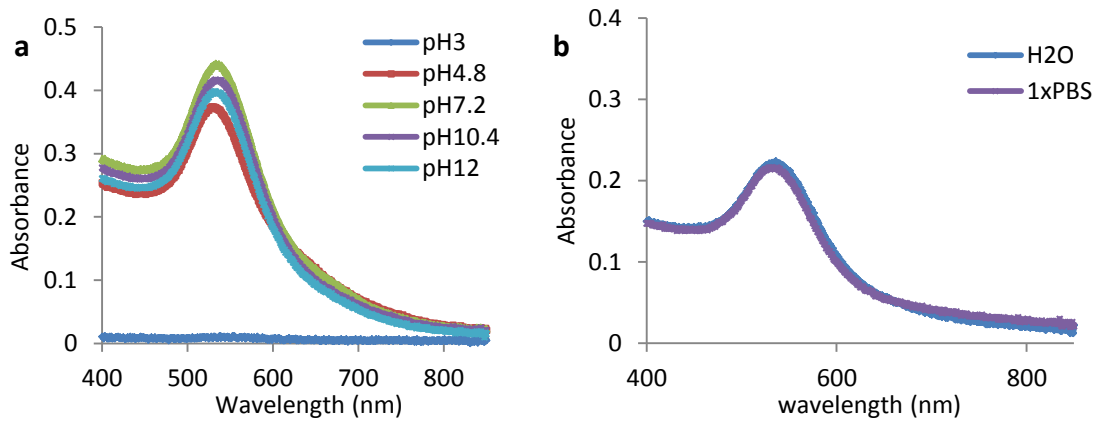


Figure 42 Stability of AuNPs.

(a) UV/Vis spectra of the AuNPs under different pH's. (b) UV/Vis spectra of the AuNPs resuspended in dH₂O and 1x PBS buffer.

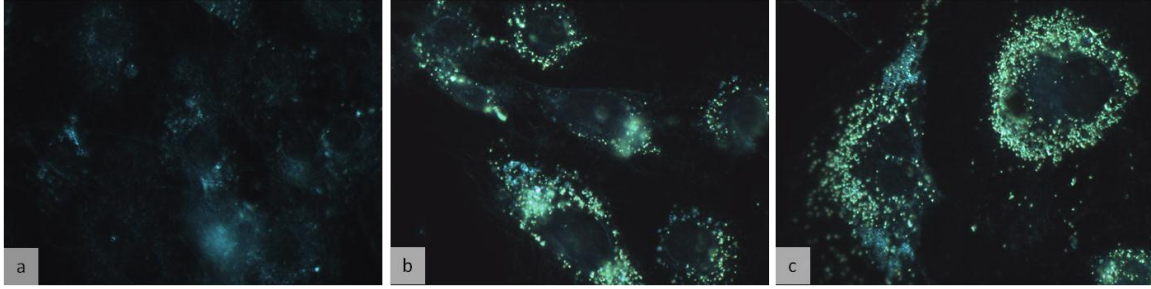


Figure 43 Endocytosis of AuNPs in MC3T3 cells.

(a) Dark-field image of MC3T3 cells without AuNPs. (b, c) Dark-field image of MC3T3 cells with AuNPs.

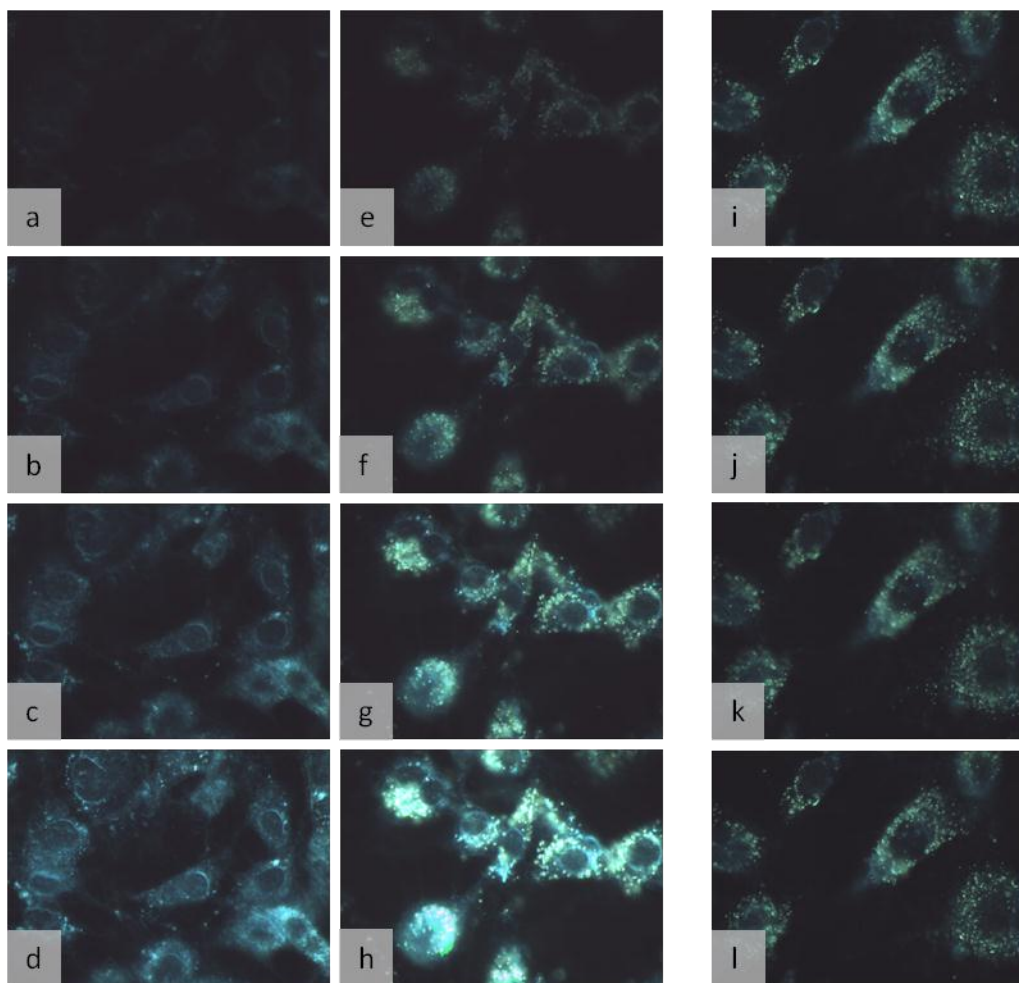


Figure 44 Dark-field light microscopy images of MC3T3 cells with or without AuNPs.

(a-d) MC3T3 cells without AuNPs at exposure time of 1.6, 5, 10 and 20 ms. (e-h) MC3T3 cells with AuNPs at exposure time of 1.6, 5, 10 and 20 ms. (i-l) MC3T3 cells with AuNPs at different cellular depth.

not bound to the exterior surface of the cell (Figure 44). Based on these images, the AuNPs seem to be concentrated in perinuclear areas of the cell and are not translocated to the nucleus. This microscopic analysis confirms that the AuNPs were successfully internalized into MC3T3 cells.

Conclusion

In summary, a new method has been developed to synthesize AuNPs through this study. The method used the organosilicone surfactant, Silwet L-77, as both a reducing and capping agent to rapidly synthesize different shapes and sizes of AuNPs. The AuNP synthesis was further tuned by addition of NaOH without or with AgNO₃ to control the size and morphology of the nanoparticles. These synthesized AuNPs were stable from pH's of 5-12, and easily passed through the cell membrane, as demonstrated using the MC3T3 cell line. The promising penetration capacity and simplicity of the synthesis method indicates a potential for the development of biomedically important AuNPs using this methodology. Since Silwet L-77 is an active reagent accompanying herbicides, the results from this study suggest that the chemicals applied to the plants might furnish them extra capacity in the bio-synthesis of metal and other nanoparticles.

CHAPTER IX. CONCLUSIONS AND RECOMMENDATIONS

Green nanofabrication has been actively pursued in recent years to meet the need for large quantities of highly purified, structurally well-defined and precisely functionalized nanomaterials. In the present study, the ability of plants to provide a large source of functional nanomaterials was investigated by the examination of plant-based materials. The findings from this study include: 1) the discovery of natural nanomaterials from live plants or plant-derived materials, 2) the potential of these nanomaterials for biomedical applications, and 3) the capacity of plants to function as factories for the production of metallic nanomaterials. Despite the progress was achieved during the course of this study, there are still considerable challenges remaining to obtain optimal performance and benefits from the use of these plant-based green nano-manufacturing systems. These include but are not limited to the following:

1. *Further demonstrate the potential for the plant-based nanomaterials to be used in biomedical applications.* While the nanofiber networks from the sundew and Chinese yam were evaluated for their potential applications in tissue engineering, these studies were only cursory to demonstrate the possibility of their use. The studies that were conducted were *in vitro* and limited based on the methods used to deposit and generate the nanofiber networks. More thorough analysis requires the development of fabrication procedures to generate a reproducible 2D coating, and the gradual transition to a robust 3D scaffold. The completion of an efficient and robust fabrication procedure and the *in vitro* and *in vivo* testing of these scaffolds would be more realistic for actual biomedical

applications, including the testing on the surfaces of implantable materials. Complete toxicity study and chemical composition analysis of these nanomaterials will be essential to gain more general acceptance.

2. Develop structure-activity relationships to predict the properties and functions of the identified nanomaterials. To tune and optimize the performance of the identified plant-based nanomaterials, it is necessary to understand the physical and chemical properties of these nanomaterials. In order to engineer plant-based nanomaterials, or to combine them with other materials, it is necessary to understand how the materials will interact within themselves or with other materials. This will allow prediction of binding, cross-linking, etc. that is crucial for modifying the nanomaterials to a specific purpose. As seen in the ivy nanoparticle-embedded adhesive, the understanding of how ivy nanoparticles interact with the surrounding polysaccharide matrix is crucial to understanding how the adhesive is functioning. Similarly, in the sundew adhesive, the nanofiber network created from different species varies, however, at present the factors affecting the formation of the nanofibers are not understood. Additionally, there is no quantitative analysis of the mechanical and physical properties of the nanofiber networks from different species. Previous studies have demonstrated that the elasticity of the adhesive species is highly variable. However, the structure-function relationship of the different adhesives has not been investigated. This kind of systematic evaluation and understanding is necessary if the ultimate goal is to evaluate and engineer advanced systems based on the

incorporation of the identified plant nanomaterials.

3. *Develop purification methods that preserve natural properties of the plant-based nanomaterials.* Nanomaterials identified in plants are typically not as resistant to harsh treatments as synthetic nanomaterials. Due to their fragile nature and the complicated chemical compositions accompanying their production, the purification or isolation of plant-based nanomaterials can be quite complex. Functionalities and efficacy could be easily lost during the isolation process through routine methods. Future efforts require us to understand the mechanisms or identify the components that control the growth of nanomaterials in plants. This then allows the application of genetic engineering approaches to produce natural nanomaterials if they own protein-based structures, or the use of bioreactors to synthesize nanoparticles if enzymes are involved in the synthesis process. The isolation process can then be simplified due to the less complicated starting materials for purification. Other alternative options that optimize the purification process include the selection and development of proper solvents that function well while preserving the natural nanomaterial structures, as well as the development of specific pore sizes of membranes and selection of proper materials of membranes for filtration and ultrafiltration.

4. *Fine control of the growth of nanomaterials in plants or natural systems.* This may be achieved in different ways. In the sundew adhesive, strength and structure of nanofiber networks formed from the adhesive might be controlled through the adjustment of nutrition and light exposure during plant

growth. While in plants for the synthesis of metal or other types of nanoparticles, non-toxic chemicals might be added to the plants to tune the reactions for the nanoparticle synthesis. As demonstrated by the roles of Silwet L-77 and other chemicals in the manufacturing of gold or silver nanoparticles, the addition of chemicals to plants might offer them extra nano-synthesis capacity that is not present in the native systems of plants. Future studies thus will be directed to test whether and how different non-toxic chemicals added to the plants could affect the capacity of nanoparticle productions by plants. Through these studies, the limitation to only a few types and sizes of metal nanoparticles synthesized currently from plants might be overcome through the addition of extra chemical components into plants. This, then, will greatly expand the capacity and strengthen the role of plants as a major manufacturing system in the biosynthesis of environment-beneficial nanomaterials.

LIST OF REFERENCES

1. Fan, Z.; Razavi, H.; Do, J.; Moriwaki, A.; Ergen, O., et al., Three-dimensional nanopillar-array photovoltaics on low-cost and flexible substrates. *Nat. Mater.* **2009**, 8, 648-653.
2. Byrne, J. D.; Betancourt, T.; Brannon-Peppas, L., Active targeting schemes for nanoparticle systems in cancer therapeutics. *Adv. Drug Delivery Rev.* **2008**, 60, 1615-1626.
3. Jiang, L.; Zhao, Y.; Zhai, J., A lotus-leaf-like superhydrophobic surface: A porous microsphere/nanofiber composite film prepared by electrohydrodynamics. *Angew. Chem., Int. Ed.* **2004**, 43, 4338-4341.
4. Feng, L.; Li, S.; Li, Y.; Li, H.; Zhang, L., et al., Super-hydrophobic surfaces: From natural to artificial. *Adv. Mater. (Weinheim, Ger.)* **2002**, 14, 1857-1860.
5. Alberts, B.; Johnson, A.; Lewis, J.; Raff, M.; Roberts, K., et al., *Molecular Biology of the Cell*. 4th ed.; Garland Science: New York, **2002**.
6. Schmid, T.; Burkhard, J.; Yeo, B. S.; Zhang, W.; Zenobi, R., Towards chemical analysis of nanostructures in biofilms I: Imaging of biological nanostructures. *Anal. Bioanal. Chem.* **2008**, 391, 1899-1905.
7. Bonser, R. H. C.; Dawson, C., The structural mechanical properties of down feathers and biomimicking natural insulation materials. *J. Mater. Sci. Lett.* **1999**, 18, 1769-1770.
8. Koch, K.; Dommissse, A.; Niemietz, A.; Barthlott, W.; Wandelt, K., Nanostructure of epicuticular plant waxes: Self-assembly of wax tubules. *Surf. Sci.* **2009**, 603, 1961-1968.
9. Weiss, J.; Takhistov, P.; McClements, D. J., Functional materials in food nanotechnology. *J. Food Sci.* **2006**, 71, R107-R116.
10. Sameoto, D.; Menon, C., Recent advances in the fabrication and adhesion testing of biomimetic dry adhesives. *Smart Mater. Struct.* **2010**, 19, 103001.
11. Bhushan, B., Biomimetics: Lessons from nature - an overview. *Philos. Trans. R. Soc., A* **2009**, 367, 1445-1486.
12. Kustandi, T. S.; Low, H. Y.; Teng, J. H.; Rodriguez, I.; Yin, R., Mimicking domino-like photonic nanostructures on butterfly wings. *Small* **2009**, 5, 574-578.
13. Dalby, M. J.; Gadegaard, N.; Curtis, A. S.; Oreffo, R. O., Nanotopographical control of human osteoprogenitor differentiation. *Curr. Stem Cell Res. Ther.* **2007**, 2, 129-138.
14. Angeloni, N. L.; Bond, C. W.; Tang, Y.; Harrington, D. A.; Zhang, S., et al., Regeneration of the cavernous nerve by Sonic hedgehog using aligned peptide amphiphile nanofibers. *Biomaterials* **2011**, 32, 1091-1101.
15. Sargeant, T. D.; Oppenheimer, S. M.; Dunand, D. C.; Stupp, S. I., Titanium foam-bioactive nanofiber hybrids for bone regeneration. *J. Tissue Eng. Regen. Med.* **2008**, 2, 455-462.

16. Stout, D. A.; Basu, B.; Webster, T. J., Poly(lactic-co-glycolic acid): Carbon nanofiber composites for myocardial tissue engineering applications. *Acta Biomater.* **2011**, *7*, 3101-3112.
17. Woo, K. M.; Chen, V. J.; Ma, P. X., Nano-fibrous scaffolding architecture selectively enhances protein adsorption contributing to cell attachment. *J. Biomed. Mater. Res., Part A* **2003**, *67A*, 531-537.
18. Zhang, M.; Liu, M.; Prest, H.; Fischer, S., Nanoparticles secreted from ivy rootlets for surface climbing. *Nano Lett.* **2008**, *8*, 1277-1280.
19. Polesuk, J.; Amodeo, J. M.; Ma, T. S., Microchemical investigation of medicinal plants. X. Analysis of the Chinese herbal drug Yunnan Bai Yao. *Mikrochim. Acta* **1973**, 507-517.
20. Ogle, C. W.; Dai, S.; Ma, J. C., The haemostatic effects of the Chinese herbal drug Yunnan Bai Yao: A pilot study. *Am. J. Chin. Med.* **1976**, *4*, 147-152.
21. Horvathova, E.; Slamenova, D.; Marsalkova, L.; Sramkova, M.; Wsolova, L., Effects of borneol on the level of DNA damage induced in primary rat hepatocytes and testicular cells by hydrogen peroxide. *Food Chem. Toxicol.* **2009**, *47*, 1318-1323.
22. Hu, K.; Yao, X., The cytotoxicity of methyl protoneogracillin (NSC-698793) and gracillin (NSC-698787), two steroidal saponins from the rhizomes of *Dioscorea collettii* var. *hypoglauca*, against human cancer cells in vitro. *Phytother. Res.* **2003**, *17*, 620-626.
23. Hu, K.; Yao, X., The cytotoxicity of protoneodioscin (NSC-698789), a furostanol saponin from the rhizomes of *Dioscorea collettii* var. *hypoglauca*, against human cancer cells in vitro. *Phytomedicine* **2002**, *9*, 560-565.
24. Shen, C. C.; Tsai, S. Y.; Wei, S. L.; Wang, S. T.; Shieh, B. J., et al., Flavonoids isolated from *Draconis Resina*. *Nat. Prod. Res.* **2007**, *21*, 377-380.
25. Wang, Y.; Zhang, Y. J.; Gao, W. Y.; Yan, L. L., Anti-tumor constituents from *Paris polyphylla* var. *yunnanensis*. *Zhongguo Zhong Yao Za Zhi* **2007**, *32*, 1425-1428.
26. Huang, H.; Wu, D.; Tian, W. X.; Ma, X. F.; Wu, X. D., Antimicrobial effect by extracts of rhizome of *Alpinia officinarum* Hance may relate to its inhibition of beta-ketoacyl-ACP reductase. *J. Enzyme Inhib. Med. Chem.* **2008**, *23*, 362-368.
27. Cui, X.; Sakaguchi, T.; Shirai, Y.; Hatakeyama, K., Orally administered *Panax ginseng* extract decreases platelet adhesiveness in 66% hepatectomized rats. *Am. J. Chin. Med.* **1999**, *27*, 251-256.
28. Li, Y. H.; Sun, X. P.; Zhang, Y. Q.; Wang, N. S., The antithrombotic effect of borneol related to its anticoagulant property. *Am. J. Chin. Med.* **2008**, *36*, 719-727.

29. Rizzo, N. W.; Gardner, K. H.; Walls, D. J.; Keiper-Hrynko, N. M.; Ganzke, T. S., et al., Characterization of the structure and composition of gecko adhesive setae. *J. R. Soc. Interface* **2006**, 3, 441-451.
30. Tsai, W. J.; Hsieh, H. T.; Chen, C. C.; Kuo, Y. C.; Chen, C. F., Characterization of the antiplatelet effects of (2S)-5-methoxy-6-methylflavan-7-ol from *Draconis Resina*. *Eur. J. Pharmacol.* **1998**, 346, 103-110.
31. Akchurin, T.; Aissiou, T.; Kemeny, N.; Prosk, E.; Nigam, N., et al., Complex dynamics of osteoclast formation and death in long-term cultures. *PLoS One* **2008**, 3, e2104.
32. Radomski, A.; Jurasz, P.; Alonso-Escolano, D.; Drews, M.; Morandi, M., et al., Nanoparticle-induced platelet aggregation and vascular thrombosis. *Br. J. Pharmacol.* **2005**, 146, 882-893.
33. Park, H. J.; Rhee, M. H.; Park, K. M.; Nam, K. Y.; Park, K. H., Effect of non-saponin fraction from *Panax ginseng* on cGMP and thromboxane A2 in human platelet aggregation. *J. Ethnopharmacol.* **1995**, 49, 157-162.
34. Wang, J.; Huang, Z. G.; Cao, H.; Wang, Y. T.; Hui, P., et al., Screening of anti-platelet aggregation agents from *Panax notoginseng* using human platelet extraction and HPLC-DAD-ESI-MS/MS. *J. Sep. Sci.* **2008**, 31, 1173-1180.
35. Wang, J.; Xu, J.; Zhong, J. B., Effect of *Radix notoginseng* saponins on platelet activating molecule expression and aggregation in patients with blood hyperviscosity syndrome. *Zhongguo Zhong Xi Yi Jie He Za Zhi* **2004**, 24, 312-316.
36. Zielinska-Jencylik, J.; Sypula, A.; Budko, E.; Rzadkowska-Bodalska, H., Interferonogenic and antiviral effect of extracts from *Erodium cicutarium*. II. Modulatory activity of *Erodium cicutarium* extracts. *Arch. Immunol. Ther. Exp. (Warsz.)* **1988**, 36, 527-536.
37. Gohar, A. A.; Lahloub, M. E.; Niwa, M., Antibacterial polyphenol from *Erodium glaucophyllum*. *Z. Naturforsch. [C]* **2003**, 58, 670-674.
38. Sroka, Z.; Rzadkowska-Bodalska, H.; Mazol, I., Antioxidative effect of extracts from *Erodium cicutarium* L. *Z. Naturforsch. [C]* **1994**, 49, 881-884.
39. Cai, Z.; Hou, S.; Li, Y.; Zhao, B.; Yang, Z., et al., Effect of borneol on the distribution of gastrodin to the brain in mice via oral administration. *J. Drug Target.* **2008**, 16, 178-184.
40. Guo, L.; Su, J.; Deng, B. W.; Yu, Z. Y.; Kang, L. P., et al., Active pharmaceutical ingredients and mechanisms underlying phasic myometrial contractions stimulated with the saponin extract from *Paris polyphylla* Sm. var. *yunnanensis* used for abnormal uterine bleeding. *Hum. Reprod.* **2008**, 23, 964-971.
41. Yan, L. L.; Zhang, Y. J.; Gao, W. Y.; Man, S. L.; Wang, Y., In vitro and in vivo anticancer activity of steroid saponins of *Paris polyphylla* var. *yunnanensis*. *Exp. Oncol.* **2009**, 31, 27-32.

42. Zhao, Y.; Kang, L. P.; Liu, Y. X.; Liang, Y. G.; Tan, D. W., et al., Steroidal saponins from the rhizome of *Paris polyphylla* and their cytotoxic activities. *Planta Med.* **2009**, *75*, 356-363.
43. Miller, V. M.; Hunter, L. W.; Chu, K.; Kaul, V.; Squillace, P. D., et al., Biologic nanoparticles and platelet reactivity. *Nanomedicine* **2009**, *4*, 725-733.
44. Price, R. L.; Waid, M. C.; Haberstroh, K. M.; Webster, T. J., Selective bone cell adhesion on formulations containing carbon nanofibers. *Biomaterials* **2003**, *24*, 1877-1887.
45. Salehi-Khojin, A.; Stone, J. J.; Zhong, W.-H., Improvement of interfacial adhesion between UHMWPE fiber and epoxy matrix using functionalized graphitic nanofibers. *J. Compos. Mater.* **2007**, *41*, 1163-1176.
46. Xu, L. R.; Li, L.; Lukehart, C. M.; Kuai, H., Mechanical characterization of nanofiber-reinforced composite adhesives. *J. Nanosci. Nanotechnol.* **2007**, *7*, 2546-2548.
47. Mahdavi, A.; Ferreira, L.; Sundback, C.; Nichol, J. W.; Chan, E. P., et al., A biodegradable and biocompatible gecko-inspired tissue adhesive. *Proc. Natl. Acad. Sci. U. S. A.* **2008**, *105*, 2307-2312.
48. Zhao, B.; Pesika, N.; Rosenberg, K.; Tian, Y.; Zeng, H., et al., Adhesion and friction force coupling of gecko setal arrays: Implications for structured adhesive surfaces. *Langmuir* **2008**, *24*, 1517-1524.
49. Schneider, A.; Garlick, J. A.; Egles, C., Self-assembling peptide nanofiber scaffolds accelerate wound healing. *PLoS One* **2008**, *3*, e1410.
50. Long, J. H.; Tan, W. Y.; Jiang, R. W.; Zhang, Y. Z., Experimental study on gelatin/polycaprolactam composite nanofiber scaffold in wound healing. *Zhonghua Shao Shang Za Zhi* **2008**, *24*, 42-44.
51. Ruan, W. J.; Lai, M. D.; Zhou, J. G., Anticancer effects of Chinese herbal medicine, science or myth? *J. Zhejiang Univ. Sci. B* **2006**, *7*, 1006-1014.
52. Okuda, T.; Mori, K.; Hayashi, N., Constituents of *Geranium thunbergii* Sieb. et Zucc. III. Application of determination methods of tannin activity with hemoglobin and of ellagitannin with nitrous acid. *Yakugaku Zasshi* **1976**, *96*, 1143-1149.
53. Wilson, C. J.; Clegg, R. E.; Leavesley, D. I.; Pearcy, M. J., Mediation of biomaterial-cell interactions by adsorbed proteins: A review. *Tissue Eng.* **2005**, *11*, 1-18.
54. Rosales-Leal, J. I.; Rodríguez-Valverde, M. A.; Mazzaglia, G.; Ramón-Torregrosa, P. J.; Díaz-Rodríguez, L., et al., Effect of roughness, wettability and morphology of engineered titanium surfaces on osteoblast-like cell adhesion. *Colloids Surf., A* **2010**, *365*, 222-229.
55. Geiger, B.; Spatz, J. P.; Bershadsky, A. D., Environmental sensing through focal adhesions. *Nat. Rev. Mol. Cell Biol.* **2009**, *10*, 21-33.
56. Curtis, A. S.; Casey, B.; Gallagher, J. O.; Pasqui, D.; Wood, M. A., et al., Substratum nanotopography and the adhesion of biological cells. Are

- symmetry or regularity of nanotopography important? *Biophys. Chem.* **2001**, 94, 275-283.
57. Stevens, M. M.; George, J. H., Exploring and engineering the cell surface interface. *Science* **2005**, 310, 1135-1138.
 58. von der Mark, K.; Park, J.; Bauer, S.; Schmuki, P., Nanoscale engineering of biomimetic surfaces: Cues from the extracellular matrix. *Cell Tissue Res.* **2010**, 339, 131-153.
 59. Xin, H. L.; Wu, Y. C.; Su, Y. H.; Sheng, J. Y.; Ling, C. Q., Novel flavonoids from the leaves of *Actinidia valvata* Dunn: Structural elucidation and antioxidant activity. *Planta Med.* **2010**, 77, 70-73.
 60. Kuete, V.; Dongfack, M. D.; Mbaveng, A. T.; Lallemand, M. C.; Van-Dufat, H. T., et al., Antimicrobial activity of the methanolic extract and compounds from the stem bark of *Drypetes tessmanniana*. *Chin. J. Integ. Med.* **2010**, 16, 337-343.
 61. Huang, Y. N.; Zhao, Y. L.; Gao, X. L.; Zhao, Z. F.; Jing, Z., et al., Intestinal alpha-glucosidase inhibitory activity and toxicological evaluation of *Nymphaea stellata* flowers extract. *J. Ethnopharmacol.* **2010**, 131, 306-312.
 62. Zhou, P.; Gross, S.; Liu, J. H.; Yu, B. Y.; Feng, L. L., et al., Flavokawain B, the hepatotoxic constituent from kava root, induces GSH-sensitive oxidative stress through modulation of IKK/NF- κ B and MAPK signaling pathways. *FASEB J.* **2010**.
 63. Chang, R., Bioactive polysaccharides from traditional Chinese medicine herbs as anticancer adjuvants. *J. Altern. Complement. Med.* **2002**, 8, 559-565.
 64. Ma, C.; Wang, W.; Chen, Y. Y.; Liu, R. N.; Wang, R. F., et al., Neuroprotective and antioxidant activity of compounds from the aerial parts of *Dioscorea opposita*. *J. Nat. Prod.* **2005**, 68, 1259-1261.
 65. Zhang, Y.; Lin, Q.; Wei, J. N.; Zhu, H. J., Study on enzyme-assisted extraction of polysaccharides from *Dioscorea opposita*. *Zhongguo Zhong Yao Za Zhi* **2008**, 33, 374-377.
 66. Lamers, E.; van Horssen, R.; te Riet, J.; van Delft, F. C.; Luttge, R., et al., The influence of nanoscale topographical cues on initial osteoblast morphology and migration. *Eur. Cell. Mater.* **2010**, 20, 329-343.
 67. Su, W. T.; Liao, Y. F.; Chu, I. M., Observation of fibroblast motility on a micro-grooved hydrophobic elastomer substrate with different geometric characteristics. *Micron* **2007**, 38, 278-285.
 68. Jeon, H.; Hidai, H.; Hwang, D. J.; Healy, K. E.; Grigoropoulos, C. P., The effect of micronscale anisotropic cross patterns on fibroblast migration. *Biomaterials* **2010**, 31, 4286-4295.
 69. Lee, S. C.; Tsai, C. C.; Chen, J. C.; Lin, J. G.; Lin, C. C., et al., Effects of "Chinese yam" on hepato-nephrotoxicity of acetaminophen in rats. *Acta Pharmacol. Sin.* **2002**, 23, 503-508.

70. Shujun, W.; Jinglin, Y.; Wenyuan, G.; Hongyan, L.; Peigen, X., New starches from traditional Chinese medicine (TCM)--Chinese yam (*Dioscorea opposita* Thunb.) cultivars. *Carbohydr. Res.* **2006**, 341, 289-293.
71. Sautour, M.; Mitaine-Offer, A. C.; Miyamoto, T.; Wagner, H.; Lacaille-Dubois, M. A., A new phenanthrene glycoside and other constituents from *Dioscorea opposita*. *Chem. Pharm. Bull. (Tokyo)* **2004**, 52, 1235-1237.
72. Nagai, T.; Nagashima, T.; Suzuki, N., Purification and partial characterization of major viscous protein from yam (*Dioscorea opposita* Thunb.) tuber mucilage tororo. *Int. J. Food Prop.* **2007**, 10, 515-526.
73. Bai, B.; Li, M. J.; Wang, Y.; Liu, X. H., Studies on chemical constituents of *Dioscorea opposita*. *Zhongguo Zhong Yao Za Zhi* **2008**, 33, 1272-1274.
74. Yang, M. H.; Yoon, K. D.; Chin, Y. W.; Park, J. H.; Kim, S. H., et al., Neuroprotective effects of *Dioscorea opposita* on scopolamine-induced memory impairment in in vivo behavioral tests and in vitro assays. *J. Ethnopharmacol.* **2009**, 121, 130-134.
75. Gao, X.; Li, B.; Jiang, H.; Liu, F.; Xu, D., et al., *Dioscorea opposita* reverses dexamethasone induced insulin resistance. *Fitoterapia* **2007**, 78, 12-15.
76. Nagai, T.; Nagashima, T., Functional properties of dioscorin, a soluble viscous protein from Japanese yam (*Dioscorea opposita* thunb.) tuber mucilage tororo. *Z. Naturforsch. [C]* **2006**, 61, 792-798.
77. Karasuda, S.; Tanaka, S.; Kajihara, H.; Yamamoto, Y.; Koga, D., Plant chitinase as a possible biocontrol agent for use instead of chemical fungicides. *Biosci. Biotechnol. Biochem.* **2003**, 67, 221-224.
78. Hsieh, M. T.; Peng, W. H.; Wu, C. R.; Wang, W. H., The ameliorating effects of the cognitive-enhancing Chinese herbs on scopolamine-induced amnesia in rats. *Phytother. Res.* **2000**, 14, 375-377.
79. Kong, X. F.; Zhang, Y. Z.; Yin, Y. L.; Wu, G. Y.; Zhou, H. J., et al., Chinese yam polysaccharide enhances growth performance and cellular immune response in weanling rats. *J. Sci. Food Agric.* **2009**, 89, 2039-2044.
80. Zhao, G.; Kan, J.; Li, Z.; Chen, Z., Structural features and immunological activity of a polysaccharide from *Dioscorea opposita* Thunb roots. *Carbohydr. Polym.* **2005**, 61, 125-131.
81. Xu, Q.; Xu, Z. L.; Shen, Z. G.; Shi, Y. Y., Research of polysaccharide from *Dioscorea opposita* Thunb. *Zhong Yao Cai* **2006**, 29, 909-912.
82. Shekaran, A.; Garcia, A. J., Nanoscale engineering of extracellular matrix-mimetic bioadhesive surfaces and implants for tissue engineering. *Biochim. Biophys. Acta, Gen. Subj.* **2011**, 1810, 350-360.
83. Svensson, A.; Nicklasson, E.; Harrah, T.; Panilaitis, B.; Kaplan, D. L., et al., Bacterial cellulose as a potential scaffold for tissue engineering of cartilage. *Biomaterials* **2005**, 26, 419-431.
84. Zielinski, B. A.; Aebischer, P., Chitosan as a matrix for mammalian cell encapsulation. *Biomaterials* **1994**, 15, 1049-1056.

85. Keilhoff, G.; Stang, F.; Wolf, G.; Fansa, H., Bio-compatibility of type I/III collagen matrix for peripheral nerve reconstruction. *Biomaterials* **2003**, 24, 2779-2787.
86. Sakai, S.; Hashimoto, I.; Kawakami, K., Synthesis of an agarose-gelatin conjugate for use as a tissue engineering scaffold. *J. Biosci. Bioeng.* **2007**, 103, 22-26.
87. Knight, R. L.; Wilcox, H. E.; Korossis, S. A.; Fisher, J.; Ingham, E., The use of acellular matrices for the tissue engineering of cardiac valves. *Proc. Inst. Mech. Eng.* **2008**, 222, 129-143.
88. Cheng, E. Y.; Kropp, B. P., Urologic tissue engineering with small-intestinal submucosa: Potential clinical applications. *World J. Urol.* **2000**, 18, 26-30.
89. Wu, W.; Feng, X.; Mao, T.; Feng, X.; Ouyang, H. W., et al., Engineering of human tracheal tissue with collagen-enforced poly-lactic-glycolic acid non-woven mesh: A preliminary study in nude mice. *Br. J. Oral Maxillofac. Surg.* **2007**, 45, 272-278.
90. Thein-Han, W. W.; Kitiyanant, Y.; Misra, R. D. K., Chitosan as scaffold matrix for tissue engineering. *Mater. Sci. Technol.* **2008**, 24, 1062-1075.
91. Dvir-Ginzberg, M.; Gamlieli-Bonshtein, I.; Agbaria, R.; Cohen, S., Liver tissue engineering within alginate scaffolds: Effects of cell-seeding density on hepatocyte viability, morphology, and function. *Tissue Eng.* **2003**, 9, 757-766.
92. Xia, L.; Lenaghan, S.; Zhang, M.; Zhang, Z.; Li, Q., Naturally occurring nanoparticles from English ivy: An alternative to metal-based nanoparticles for UV protection. *J. Nanobiotechnol.* **2010**, 8, 12.
93. Tuszyński, G. P.; Murphy, A., Spectrophotometric quantitation of anchorage-dependent cell numbers using the bicinchoninic acid protein assay reagent. *Anal. Biochem.* **1990**, 184, 189-191.
94. Farndale, R. W.; Buttle, D. J.; Barrett, A. J., Improved quantitation and discrimination of sulphated glycosaminoglycans by use of dimethylmethylene blue. *Biochim. Biophys. Acta, Gen. Subj.* **1986**, 883, 173-177.
95. Zhang, M.; Lenaghan, S.; Xia, L.; Dong, L.; He, W., et al., Nanofibers and nanoparticles from the insect-capturing adhesive of the Sundew (*Drosera*) for cell attachment. *J. Nanobiotechnol.* **2010**, 8, 20.
96. Nerem, R. M., Tissue engineering: Confronting the transplantation crisis. *Proc. Inst. Mech. Eng.* **2000**, 214, 95-99.
97. Bhattarai, S. R.; Bhattarai, N.; Yi, H. K.; Hwang, P. H.; Cha, D. I., et al., Novel biodegradable electrospun membrane: Scaffold for tissue engineering. *Biomaterials* **2004**, 25, 2595-2602.
98. He, W.; Yong, T.; Teo, W. E.; Ma, Z.; Ramakrishna, S., Fabrication and endothelialization of collagen-blended biodegradable polymer nanofibers: Potential vascular graft for blood vessel tissue engineering. *Tissue Eng.* **2005**, 11, 1574-1588.

99. Kikuchi, M.; Ikoma, T.; Itoh, S.; Matsumoto, H. N.; Koyama, Y., et al., Biomimetic synthesis of bone-like nanocomposites using the self-organization mechanism of hydroxyapatite and collagen. *Compos. Sci. Technol.* **2004**, 64, 819-825.
100. Hubbell, J. A.; Massia, S. P.; Drumheller, P. D., Surface-grafted cell-binding peptides in tissue engineering of the vascular graft. *Ann. N. Y. Acad. Sci.* **1992**, 665, 253-258.
101. Ciardelli, G.; Chiono, V.; Vozzi, G.; Pracella, M.; Ahluwalia, A., et al., Blends of poly-(ϵ -caprolactone) and polysaccharides in tissue engineering applications. *Biomacromolecules* **2005**, 6, 1961-1976.
102. Iwasaki, N.; Yamane, S. T.; Majima, T.; Kasahara, Y.; Minami, A., et al., Feasibility of polysaccharide hybrid materials for scaffolds in cartilage tissue engineering: Evaluation of chondrocyte adhesion to polyion complex fibers prepared from alginate and chitosan. *Biomacromolecules* **2004**, 5, 828-833.
103. Madhally, S. V.; Matthew, H. W. T., Porous chitosan scaffolds for tissue engineering. *Biomaterials* **1999**, 20, 1133-1142.
104. Baier Leach, J.; Bivens, K. A.; Patrick, C. W.; Schmidt, C. E., Photocrosslinked hyaluronic acid hydrogels: Natural, biodegradable tissue engineering scaffolds. *Biotechnol. Bioeng.* **2003**, 82, 578-589.
105. Lasky, L. A., Selectin-carbohydrate interactions and the initiation of the inflammatory response. *Biochemistry* **1995**, 64, 113-139.
106. Klementsén, B.; Jørgensen, L., Distribution of adhesion molecules on HeLa cells, platelets and endothelium in an in vitro model mimicking the early phase of metastasis. An immunogold electron microscopic study. *APMIS* **1997**, 105, 546-558.
107. Dixon, K. W.; Pate, J. S.; Bailey, W. J., Nitrogen nutrition of the tuberous sundew *Drosera erythrorhiza* Lindl. with special reference to catch of arthropod fauna by its glandular leaves. *Aust. J. Bot.* **1980**, 28, 283-297.
108. Williams, S. E.; Pickard, B. G., Receptor potentials and action potentials in *Drosera* tentacles. *Planta* **1972**, 103, 193-221.
109. Williams, S. E., Comparative sensory physiology of the Droseraceae - the evolution of a plant sensory system. *Proc. Natl. Acad. Sci. U. S. A.* **1976**, 120, 187-204.
110. Amagase, S., Digestive enzymes in insectivorous plants. III. Acid proteases in the genus *Nepenthes* and *Drosera peltata*. *J. Biochem. (Tokyo)* **1972**, 72, 73-81.
111. Amagase, S.; Mori, M.; Nakayama, S., Digestive enzymes in insectivorous plants. IV. Enzymatic digestion of insects by *Nepenthes* secretion and *Drosera peltata* extract: Proteolytic and chitinolytic activities. *J. Biochem. (Tokyo)* **1972**, 72, 765-767.
112. Chandler, G. E.; Anderson, J. W., Studies on the origin of some hydrolytic enzymes associated with the leaves and tentacles of *Drosera* species and their role in heterotrophic nutrition. *New Phytol.* **1976**, 77, 51-62.

113. Libantová, J.; Kämäräinen, T.; Moravčíková, J.; Matušíková, I.; Salaj, J., Detection of chitinolytic enzymes with different substrate specificity in tissues of intact sundew (*Drosera rotundifolia* L.). *Mol. Biol. Rep.* **2009**, *36*, 851-856.
114. Matušíková, I.; Salaj, J.; Moravčíková, J.; Mlynárová, L.; Nap, J. P., et al., Tentacles of in vitro-grown round-leaf sundew (*Drosera rotundifolia* L.) show induction of chitinase activity upon mimicking the presence of prey. *Planta* **2005**, *222*, 1020-1027.
115. White, J., The proteolytic enzyme of *Drosera*. *Proc. R. Soc. London, B* **1910**, *83*, 134-139.
116. Bopp, M.; Weber, I., Hormonal regulation of the leaf blade movement of *Drosera capensis*. *Physiol. Plant.* **1981**, *53*, 491-496.
117. Rost, K.; Schauer, R., Physical and chemical properties of the mucin secreted by *Drosera capensis*. *Phytochemistry* **1977**, *16*, 1365-1368.
118. Gowda, D. C.; Reuter, G.; Schauer, R., Structural features of an acidic polysaccharide from the mucin of *Drosera binata*. *Phytochemistry* **1982**, *21*, 2297-2300.
119. Goda, T.; Watanabe, J.; Takai, M.; Ishihara, K., Water structure and improved mechanical properties of phospholipid polymer hydrogel with phosphorylcholine centered intermolecular cross-linker. *Polymer* **2006**, *47*, 1390-1396.
120. Kusoglu, A.; Tang, Y.; Lugo, M.; Karlsson, A. M.; Santare, M. H., et al., Constitutive response and mechanical properties of PFSA membranes in liquid water. *J. Power Sources* **2010**, *195*, 483-492.
121. Paul, S. J.; Leach, M.; Rueggeberg, F. A.; Pashley, D. H., Effect of water content on the physical properties of model dentine primer and bonding resins. *J. Dent.* **1999**, *27*, 209-214.
122. Wang, J.; Wu, W., Swelling behaviors, tensile properties and thermodynamic studies of water sorption of 2-hydroxyethyl methacrylate/epoxy methacrylate copolymeric hydrogels. *Eur. Polym. J.* **2005**, *41*, 1143-1151.
123. Lin, Z.; Wu, W.; Wang, J.; Jin, X., Studies on swelling behaviors, mechanical properties, network parameters and thermodynamic interaction of water sorption of 2-hydroxyethyl methacrylate/novolac epoxy vinyl ester resin copolymeric hydrogels. *React. Funct. Polym.* **2007**, *67*, 789-797.
124. Chayed, S.; Winnik, F. M., In vitro evaluation of the mucoadhesive properties of polysaccharide-based nanoparticulate oral drug delivery systems. *Eur. J. Pharm. Biopharm.* **2007**, *65*, 363-370.
125. Payne, G. F., Biopolymer-based materials: The nanoscale components and their hierarchical assembly. *Curr. Opin. Chem. Biol.* **2007**, *11*, 214-219.

126. Beaty, N. B.; Mello, R. J., Extracellular mammalian polysaccharides: Glycosaminoglycans and proteoglycans. *J. Chromatogr.* **1987**, 418, 187-222.
127. Zhang, M.; Liu, M.; Bewick, S.; Suo, Z., Nanoparticles to increase adhesive properties of biologically secreted materials for surface affixing. *J. Biomed. Nanotechnol.* **2009**, 5, 294-299.
128. Dunham, A. C.; Wilkinson, F. C. F., Accuracy, precision and detection limits of energy-dispersive electron-microprobe analyses of silicates. *X-Ray Spectrom.* **1978**, 7, 50-56.
129. Dutkiewicz, J.; Lityńska-Dobrzyńska, L.; Kovačová, A.; Molnarova, M.; Rogal, Ł., et al., HRTEM studies of amorphous ZrNiTiCu nanocrystalline composites. *J. Microsc.* **2010**, 237, 237-241.
130. Xu, H.; Chen, T.; Konishi, H., HRTEM investigation of trilling todorokite and nano-phase Mn-oxides in manganese dendrites. *Am. Mineral.* **2010**, 95, 556-562.
131. Aasrum, E.; Ng'ang'a, P. M.; Dahm, S.; Øgaard, B., Tensile bond strength of orthodontic brackets bonded with a fluoride-releasing light-curing adhesive. An in vitro comparative study. *Am. J. Orthod. Dentofacial Orthop.* **1993**, 104, 48-50.
132. Lapique, F.; Redford, K., Curing effects on viscosity and mechanical properties of a commercial epoxy resin adhesive. *Int. J. Adhes. Adhes.* **2002**, 22, 337-346.
133. Malucelli, G.; Priola, A.; Ferrero, F.; Quaglia, A.; Frigione, M., et al., Polyurethane resin-based adhesives: Curing reaction and properties of cured systems. *Int. J. Adhes. Adhes.* **2005**, 25, 87-91.
134. Ninan, L.; Stroshine, R. L.; Wilker, J. J.; Shi, R., Adhesive strength and curing rate of marine mussel protein extracts on porcine small intestinal submucosa. *Acta Biomater.* **2007**, 3, 687-694.
135. Park, Y.; Lim, D.; Kim, H.; Park, D.; Sung, I., UV- and thermal-curing behaviors of dual-curable adhesives based on epoxy acrylate oligomers. *Int. J. Adhes. Adhes.* **2009**, 29, 710-717.
136. Greene, L. A.; Tischler, A. S., Establishment of a noradrenergic clonal line of rat adrenal pheochromocytoma cells which respond to nerve growth factor. *Proc. Natl. Acad. Sci. U. S. A.* **1976**, 73, 2424-2428.
137. Belliveau, D. J.; Bani-Yaghub, M.; McGirr, B.; Naus, C. C.; Rushlow, W. J., Enhanced neurite outgrowth in PC12 cells mediated by connexin hemichannels and ATP. *J. Biol. Chem.* **2006**, 281, 20920-20931.
138. Aoki, K.; Nakamura, T.; Inoue, T.; Meyer, T.; Matsuda, M., An essential role for the SHIP2-dependent negative feedback loop in neuritogenesis of nerve growth factor-stimulated PC12 cells. *J. Cell Biol.* **2007**, 177, 817-827.
139. Satoh, T.; Nakamura, S.; Taga, T.; Matsuda, T.; Hirano, T., et al., Induction of neuronal differentiation in PC12 cells by B-cell stimulatory factor 2/interleukin 6. *Mol. Cell. Biol.* **1988**, 8, 3546-3549.

140. Fratzl, P.; Barth, F. G., Biomaterial systems for mechanosensing and actuation. *Nature* **2009**, 462, 442-448.
141. Diffey, B. L., Solar ultraviolet radiation effects on biological systems. *Phys. Med. Biol.* **1991**, 36, 299-328.
142. Pathak, S.; Mason, N., Our shrinking ozone layer. *Resonance* **2002**, 7, 71-80.
143. Hockberger, P. E., A history of ultraviolet photobiology for humans, animals and microorganisms. *Photochem. Photobiol.* **2002**, 76, 561-579.
144. Longstreth, J.; de Gruijl, F. R.; Kripke, M. L.; Abseck, S.; Arnold, F., et al., Health risks. *J. Photochem. Photobiol. B* **1998**, 46, 20-39.
145. Friedberg, E. C., DNA damage and repair. *Nature* **2003**, 421, 436-440.
146. http://www.cancer.org/docroot/ped/content/ped_7_1_what_you_need_to_know_about_skin_cancer.asp
147. van der Leun, J. C.; de Gruijl, F. R., UV-B radiation and ozone depletion: Effects on humans, animals, plants, microorganisms, and materials. In *Influences of Ozone Depletion on Human and Animal Health*, Lewis Publishers: Ann Arbor, **1993**; pp 95-123.
148. Smith, R. C.; Prézelin, B. B.; Baker, K. S.; Bidigare, R. R.; Boucher, N. P., et al., Ozone depletion: Ultraviolet radiation and phytoplankton biology in Antarctic waters. *Science* **1992**, 255, 952-959.
149. Wolf, R.; Wolf, D.; Morganti, P.; Ruocco, V., Sunscreens. *Clin. Dermatol.* **2001**, 19, 452-459.
150. Nohynek, G. J.; Lademann, J.; Ribaud, C.; Roberts, M. S., Grey goo on the skin? Nanotechnology, cosmetic and sunscreen safety. *Crit. Rev. Toxicol.* **2007**, 37, 251-277.
151. Durand, L.; Habran, N.; Henschel, V.; Amighi, K., In vitro evaluation of the cutaneous penetration of sprayable sunscreen emulsions with high concentrations of UV filters. *Int. J. Cosmet. Sci.* **2009**, 31, 279-292.
152. Gontier, E.; Ynsa, M.-D.; Bíró, T.; Hunyadi, J.; Kiss, B., et al., Is there penetration of titania nanoparticles in sunscreens through skin? A comparative electron and ion microscopy study. *Nanotoxicology* **2009**, 2, 218-231.
153. Newman, M. D.; Stotland, M.; Ellis, J. I., The safety of nanosized particles in titanium dioxide- and zinc oxide-based sunscreens. *J. Am. Acad. Dermatol.* **2009**, 61, 685-692.
154. Oberdörster, E., Manufactured nanomaterials (fullerenes, C₆₀) induce oxidative stress in the brain of juvenile largemouth bass. *Environ. Health Perspect.* **2004**, 112, 1058-1062.
155. Baroli, B.; Ennas, M. G.; Loffredo, F.; Isola, M.; Pinna, R., et al., Penetration of metallic nanoparticles in human full-thickness skin. *J. Invest. Dermatol.* **2007**, 127, 1701-1712.
156. Menzel, F.; Reinert, T.; Vogt, J.; Butz, T., Investigations of percutaneous uptake of ultrafine TiO₂ particles at the high energy ion nanoprobe

- LIPSION. *Nucl. Instrum. Methods Phys. Res. Sect. B* **2004**, 219-220, 82-86.
157. Wu, J.; Liu, W.; Xue, C.; Zhou, S.; Lan, F., et al., Toxicity and penetration of TiO₂ nanoparticles in hairless mice and porcine skin after subchronic dermal exposure. *Toxicol. Lett.* **2009**, 191, 1-8.
 158. Buzea, C.; Pacheco, I. I.; Robbie, K., Nanomaterials and nanoparticles: Sources and toxicity. *Biointerphases* **2007**, 2, MR17-MR71.
 159. Oberdörster, G.; Oberdörster, E.; Oberdörster, J., Nanotoxicology: An emerging discipline evolving from studies of ultrafine particles. *Environ. Health Perspect.* **2005**, 113, 823-839.
 160. Nel, A.; Xia, T.; Mädler, L.; Li, N., Toxic potential of materials at the nanolevel. *Science* **2006**, 311, 622-627.
 161. Dunford, R.; Salinaro, A.; Cai, L.; Serpone, N.; Horikoshi, S., et al., Chemical oxidation and DNA damage catalysed by inorganic sunscreen ingredients. *FEBS Lett.* **1997**, 418, 87-90.
 162. Donaldson, K.; Beswick, P. H.; Gilmour, P. S., Free radical activity associated with the surface of particles: A unifying factor in determining biological activity? *Toxicol. Lett.* **1996**, 88, 293-298.
 163. Hussain, S. M.; Hess, K. L.; Gearhart, J. M.; Geiss, K. T.; Schlager, J. J., In vitro toxicity of nanoparticles in BRL 3A rat liver cells. *Toxicol. in Vitro* **2005**, 19, 975-983.
 164. Oberdörster, G.; Maynard, A.; Donaldson, K.; Castranova, V.; Fitzpatrick, J., et al., Principles for characterizing the potential human health effects from exposure to nanomaterials: Elements of a screening strategy. *Part. Fibre Toxicol.* **2005**, 2, 8.
 165. Luo, J., Toxicity and bioaccumulation of nanomaterial in aquatic species. *J. U.S. SJWP* **2007**, 2, 1-16.
 166. Zhu, S.; Oberdörster, E.; Haasch, M. L., Toxicity of an engineered nanoparticle (fullerene, C₆₀) in two aquatic species, Daphnia and fathead minnow. *Mar. Environ. Res.* **2006**, 62 Suppl, S5-S9.
 167. Tinkle, S. S.; Antonini, J. M.; Rich, B. A.; Roberts, J. R.; Salmen, R., et al., Skin as a route of exposure and sensitization in chronic beryllium disease. *Environ. Health Perspect.* **2003**, 111, 1202-1208.
 168. Larese, F. F.; D'Agostin, F.; Crosera, M.; Adami, G.; Renzi, N., et al., Human skin penetration of silver nanoparticles through intact and damaged skin. *Toxicology* **2009**, 255, 33-37.
 169. Mortensen, L. J.; Oberdörster, G.; Pentland, A. P.; DeLouise, L. A., In vivo skin penetration of quantum dot nanoparticles in the murine model: The effect of UVR. *Nano Lett.* **2008**, 8, 2779-2787.
 170. Zhang, L. W.; Yu, W. W.; Colvin, V. L.; Monteiro-Riviere, N. A., Biological interactions of quantum dot nanoparticles in skin and in human epidermal keratinocytes. *Toxicol. Appl. Pharmacol.* **2008**, 228, 200-211.
 171. Hoet, P. H.; Brüske-Hohlfeld, I.; Salata, O. V., Nanoparticles - known and unknown health risks. *J. Nanobiotechnol.* **2004**, 2, 12-12.

172. Park, I. Y.; Kim, I. Y.; Yoo, M. K.; Choi, Y. J.; Cho, M. H., et al., Mannosylated polyethylenimine coupled mesoporous silica nanoparticles for receptor-mediated gene delivery. *Int. J. Pharm.* **2008**, 359, 280-287.
173. Chithrani, D.; Stewart, J.; Allen, C.; Jaffray, D., Intracellular uptake, transport, and processing of nanostructures in cancer cells. *Nanomed. Nanotech. Biol. Med.* **2009**, 5, 118-127.
174. Harush-Frenkel, O.; Benita, M. B.; Nassar, T.; Springer, C.; Sherman, Y., et al., A safety and tolerability study of differently-charged nanoparticles for local pulmonary drug delivery. *Toxicol. Appl. Pharmacol.* **2010**, 246, 83-90.
175. Minchin, R., Nanomedicine: Sizing up targets with nanoparticles. *Nat. Nanotechnol.* **2008**, 3, 12-13.
176. Ryman-Rasmussen, J. P.; Riviere, J. E.; Monteiro-Riviere, N. A., Penetration of intact skin by quantum dots with diverse physicochemical properties. *Toxicol. Sci.* **2006**, 91, 159-165.
177. Benson, H. A., Transdermal drug delivery: Penetration enhancement techniques. *Curr. Drug Deliv.* **2005**, 2, 23-33.
178. Elias, P. M., Stratum corneum defensive functions: An integrated view. *J. Invest. Dermatol.* **2005**, 125, 183-200.
179. Lauer, A. C.; Ramachandran, C.; Lieb, L. M.; Niemiec, S.; Weiner, N. D., Targeted delivery to the pilosebaceous unit via liposomes. *Adv. Drug Delivery Rev.* **1996**, 18, 311-324.
180. Johnson, M. E.; Blankschtein, D.; Langer, R., Evaluation of solute permeation through the stratum corneum: Lateral bilayer diffusion as the primary transport mechanism. *J. Pharm. Sci.* **1997**, 86, 1162-1172.
181. Wartewig, S.; Neubert, R. H., Properties of ceramides and their impact on the stratum corneum structure: A review. Part 1: Ceramides. *Skin Pharmacol. Physiol.* **2007**, 20, 220-229.
182. Sugibayashi, K.; Hayashi, T.; Morimoto, Y., Simultaneous transport and metabolism of ethyl nicotinate in hairless rat skin after its topical application: The effect of enzyme distribution in skin. *J. Control. Release* **1999**, 62, 201-208.
183. Alvarez-Román, R.; Naik, A.; Kalia, Y. N.; Guy, R. H.; Fessi, H., Skin penetration and distribution of polymeric nanoparticles. *J. Control. Release* **2004**, 99, 53-62.
184. Kohli, A. K.; Alpar, H. O., Potential use of nanoparticles for transcutaneous vaccine delivery: Effect of particle size and charge. *Int. J. Pharm.* **2004**, 275, 13-17.
185. Diaz-Torres, R.; Sandoval, S. J. J.; Ibanez-Orozco, O.; Rodriguez-Romo, S., Polyethylcyanoacrylate nanoparticle transport through the stratum corneum. *Appl. Phys. Lett.* **2009**, 95, 043702.
186. Kuntsche, J.; Bunjes, H.; Fahr, A.; Pappinen, S.; Rönkkö, S., et al., Interaction of lipid nanoparticles with human epidermis and an organotypic cell culture model. *Int. J. Pharm.* **2008**, 354, 180-195.

187. Coulman, S. A.; Anstey, A.; Gateley, C.; Morrissey, A.; McLoughlin, P., et al., Microneedle mediated delivery of nanoparticles into human skin. *Int. J. Pharm.* **2009**, 366, 190-200.
188. Zvyagin, A. V.; Zhao, X.; Gierden, A.; Sanchez, W.; Ross, J. A., et al., Imaging of zinc oxide nanoparticle penetration in human skin in vitro and in vivo. *J. Biomed. Opt.* **2008**, 13, 064031.
189. Kalia, Y. N.; Pirot, F.; Guy, R. H., Homogeneous transport in a heterogeneous membrane: Water diffusion across human stratum corneum in vivo. *Biophys. J.* **1996**, 71, 2692-2700.
190. Kalia, Y. N.; Alberti, I.; Sekkat, N.; Curdy, C.; Naik, A., et al., Normalization of stratum corneum barrier function and transepidermal water loss in vivo. *Pharm. Res.* **2000**, 17, 1148-1150.
191. Alberti, I.; Kalia, Y. N.; Naik, A.; Bonny, J. D.; Guy, R. H., In vivo assessment of enhanced topical delivery of terbinafine to human stratum corneum. *J. Control. Release* **2001**, 71, 319-327.
192. Schwindt, D. A.; Wilhelm, K. P.; Maibach, H. I., Water diffusion characteristics of human stratum corneum at different anatomical sites in vivo. *J. Invest. Dermatol.* **1998**, 111, 385-389.
193. Williams, A. C., Transdermal drug delivery: Second edition (revised and expanded), Richard H. Guy, Jonathan Hadgraft (Eds.), ISBN: 0-8247-0861-x. *Int. J. Pharm.* **2003**, 261, 171.
194. Popov, A. P.; Lademann, J.; Priezzhev, A. V.; Myllyla, R., Effect of size of TiO₂ nanoparticles embedded into stratum corneum on ultraviolet-A and ultraviolet-B sun-blocking properties of the skin. *J. Biomed. Opt.* **2005**, 10, 064037.
195. Pitcher, H. M.; Longstreth, J. D., Melanoma mortality and exposure to ultraviolet radiation: An empirical relationship. *Environ. Int.* **1991**, 17, 7-21.
196. Jennifer, A.; Jun, W., Evolution of Hedera (the ivy genus, Araliaceae): Insights from chloroplast DNA data. *Int. J. Plant Sci.* **2003**, 164, 593-602.
197. Darwin, C. R., *The Movements and Habits of Climbing Plants*. 2nd ed.; D. Appleton and company: New York, **1876**.
198. Endress, A. G.; Thomson, W. W., Ultrastructural and cytochemical studies on the developing adhesive disc of Boston ivy tendrils. *Protoplasma* **1976**, 88, 315-331.
199. Endress, A. G.; Thomson, W. W., Adhesion of the Boston ivy tendril. *Can. J. Bot.* **1977**, 55, 918-924.
200. Moens, P., Ontogenese des vrilles et differenciation des ampoules adhesives chez quelques vegetaux (Ampelopsis, Bignonia, Glaziovia). *Cellule* **1956**, 57, 369-401.
201. Melzer, B.; Steinbrecher, T.; Seidel, R.; Kraft, O.; Schwaiger, R., et al., The attachment strategy of English ivy: A complex mechanism acting on several hierarchical levels. *J. Royal Soc. Interface* **2010**, 7, 1383-1389.

202. Autumn, K.; Sitti, M.; Liang, Y. A.; Peattie, A. M.; Hansen, W. R., et al., Evidence for van der Waals adhesion in gecko setae. *Proc. Natl. Acad. Sci. U. S. A.* **2002**, 99, 12252-12256.
203. Peattie, A. M.; Full, R. J., Phylogenetic analysis of the scaling of wet and dry biological fibrillar adhesives. *Proc. Natl. Acad. Sci. U. S. A.* **2007**, 104, 18595-18600.
204. Steinbrecher, T.; Danninger, E.; Harder, D.; Speck, T.; Kraft, O., et al., Quantifying the attachment strength of climbing plants: A new approach. *Acta Biomater.* **2010**, 6, 1497-1504.
205. Gao, H.; Yao, H., Shape insensitive optimal adhesion of nanoscale fibrillar structures. *Proc. Natl. Acad. Sci. U. S. A.* **2004**, 101, 7851-7856.
206. Wu, Y.; Zhao, X.; Zhang, M., Adhesion mechanics of ivy nanoparticles. *J. Colloid Interface Sci.* **2010**, 344, 533-540.
207. Zhai, L.; Ling, G.; Li, J.; Wang, Y., The effect of nanoparticles on the adhesion of epoxy adhesive. *Mater. Lett.* **2006**, 60, 3031-3033.
208. Corkery, R. W.; Fleischer, C.; Daly, R. C. Polymeric adhesive including nanoparticle filler. WO/2008/124389, **2008**.
209. Xing, M.; Zhong, W.; Xu, X.; Thomson, D., Adhesion force studies of nanofibers and nanoparticles. *Langmuir* **2010**, 26, 11809-11814.
210. Panyam, J.; Labhasetwar, V., Biodegradable nanoparticles for drug and gene delivery to cells and tissue. *Adv. Drug Delivery Rev.* **2003**, 55, 329-347.
211. Aoki, T.; Hiroshima, M.; Kitamura, K.; Tokunaga, M.; Yanagida, T., Non-contact scanning probe microscopy with sub-piconewton force sensitivity. *Ultramicroscopy* **1997**, 70, 45-55.
212. Binnig, G.; Quate, C. F.; Gerber, C., Atomic force microscope. *Phys. Rev. Lett.* **1986**, 56, 930-933.
213. Muller, D. J.; Dufrene, Y. F., Atomic force microscopy as a multifunctional molecular toolbox in nanobiotechnology. *Nat. Nanotechnol.* **2008**, 3, 261-269.
214. Noy, A., Chemical force microscopy of chemical and biological interactions. *Surf. Interface Anal.* **2006**, 38, 1429-1441.
215. Matthias, R.; Filipp, O.; Berthold, H.; Hermann, E. G., Single molecule force spectroscopy on polysaccharides by atomic force microscopy. *Science* **1997**, 275, 1295-1297.
216. Châtellier, X.; Senden, T. J.; Joanny, J. F.; di Meglio, J. M., Detachment of a single polyelectrolyte chain adsorbed on a charged surface. *Europhys. Lett.* **1998**, 41, 303.
217. Murashige, T.; Skoog, F., A revised medium for rapid growth and bio assays with tobacco tissue cultures. *Physiol. Plant.* **1962**, 15, 473-497.
218. Hennebert, E.; Viville, P.; Lazzaroni, R.; Flammang, P., Micro- and nanostructure of the adhesive material secreted by the tube feet of the sea star *Asterias rubens*. *J. Struct. Biol.* **2008**, 164, 108-118.

219. Callow, J. A.; Stanley, M. S.; Wetherbee, R.; Callow, M. E., Cellular and molecular approaches to understanding primary adhesion in Enteromorpha: An overview. *Biofouling* **2000**, 16, 141-150.
220. Urushida, Y.; Nakano, M.; Matsuda, S.; Inoue, N.; Kanai, S., et al., Identification and functional characterization of a novel barnacle cement protein. *FEBS J.* **2007**, 274, 4336-4346.
221. Grinevich, O.; Mejiritski, A.; Neckers, D. C., AFM force-distance curve methods for measuring the kinetics of silicon chemical etching and reactions between silylating agents and a silicon surface. *Langmuir* **1999**, 15, 2077-2079.
222. Wang, T.; Lei, C. H.; Dalton, A. B.; Creton, C.; Lin, Y., et al., Waterborne, nanocomposite pressure-sensitive adhesives with high tackenergy, optical transparency, and electrical conductivity. *Adv. Mater. (Weinheim, Ger.)* **2006**, 18, 2730-2734.
223. Gay, C.; Leibler, L., Theory of tackiness. *Phys. Rev. Lett.* **1999**, 82, 936.
224. Waychunas, G. A.; Zhang, H., Structure, chemistry, and properties of mineral nanoparticles. *Elements* **2008**, 4, 381-387.
225. Sun, W.; Neuzil, P.; Kustandi, T. S.; Oh, S.; Samper, V. D., The nature of the gecko lizard adhesive force. *Biophys. J.* **2005**, 89, L14-L17.
226. Johnson, K. L.; Kendall, K.; Roberts, A. D., Surface energy and the contact of elastic solids. *Proc. R. Soc. London, A* **1971**, 324, 301-313.
227. Israelachvili, J. N., *Intermolecular and Surface Forces*. 2nd ed.; Academic Press: Salt Lake City, **1992**.
228. Gardea-Torresdey, J. L.; Parsons, J. G.; Gomez, E.; Peralta-Videa, J.; Troiani, H. E., et al., Formation and growth of Au nanoparticles inside live alfalfa plants. *Nano Lett.* **2002**, 2, 397-401.
229. Chandran, S. P.; Chaudhary, M.; Pasricha, R.; Ahmad, A.; Sastry, M., Synthesis of gold nanotriangles and silver nanoparticles using Alovera plant extract. *Biotechnol. Prog.* **2006**, 22, 577-583.
230. Shankar, S. S.; Ahmad, A.; Pasricha, R.; Sastry, M., Bioreduction of chloroaurate ions by geranium leaves and its endophytic fungus yields gold nanoparticles of different shapes. *J. Mater. Chem.* **2003**, 13, 1822-1826.
231. Song, J. Y.; Jang, H.-K.; Kim, B. S., Biological synthesis of gold nanoparticles using Magnolia kobus and Diopyros kaki leaf extracts. *Process Biochem.* **2009**, 44, 1133-1138.
232. Xie, J.; Lee, J. Y.; Wang, D. I. C.; Ting, Y. P., Identification of active biomolecules in the high-yield synthesis of single-crystalline gold nanoplates in algal solutions. *Small* **2007**, 3, 672-682.
233. Park, Y.; Hong, Y. N.; Weyers, A.; Kim, Y. S.; Linhardt, R. J., Polysaccharides and phytochemicals: A natural reservoir for the green synthesis of gold and silver nanoparticles. *IET Nanobiotechnol.* **2011**, 5, 69-78.

234. Moulton, M. C.; Braydich-Stolle, L. K.; Nadagouda, M. N.; Kunzelman, S.; Hussain, S. M., et al., Synthesis, characterization and biocompatibility of "green" synthesized silver nanoparticles using tea polyphenols. *Nanoscale* **2010**, *2*, 763-770.
235. Grzelczak, M.; Perez-Juste, J.; Mulvaney, P.; Liz-Marzan, L. M., Shape control in gold nanoparticle synthesis. *Chem. Soc. Rev.* **2008**, *37*, 1783-1791.
236. Yee, C. K.; Ulman, A.; Ruiz, J. D.; Parikh, A.; White, H., et al., Alkyl selenide- and alkyl thiolate-functionalized gold nanoparticles: Chain packing and bond nature. *Langmuir* **2003**, *19*, 9450-9458.
237. Briñas, R. P.; Hu, M.; Qian, L.; Lyman, E. S.; Hainfeld, J. F., Gold nanoparticle size controlled by polymeric Au(I) thiolate precursor size. *J. Am. Chem. Soc.* **2007**, *130*, 975-982.
238. Birbaum, K.; Brogioli, R.; Schellenberg, M.; Martinoia, E.; Stark, W. J., et al., No evidence for cerium dioxide nanoparticle translocation in maize plants. *Environ. Sci. Technol.* **2010**, *44*, 8718-8723.
239. Zhang, Z.; He, X.; Zhang, H.; Ma, Y.; Zhang, P., et al., Uptake and distribution of ceria nanoparticles in cucumber plants. *Metallomics* **2011**, *3*, 816-822.
240. Cifuentes, Z.; Custardoy, L.; de la Fuente, J.; Marquina, C.; Ibarra, M. R., et al., Absorption and translocation to the aerial part of magnetic carbon-coated nanoparticles through the root of different crop plants. *J. Nanobiotechnol.* **2010**, *8*, 26.
241. Larson, T. A.; Bankson, J.; Aaron, J.; Sokolov, K., Hybrid plasmonic magnetic nanoparticles as molecular specific agents for MRI/optical imaging and photothermal therapy of cancer cells. *Nanotechnology* **2007**, *18*, 325101.
242. Debouttière, P. J.; Roux, S.; Vocanson, F.; Billotey, C.; Beuf, O., et al., Design of gold nanoparticles for magnetic resonance imaging. *Adv. Funct. Mater.* **2006**, *16*, 2330-2339.
243. Podsiadlo, P.; Sinani, V. A.; Bahng, J. H.; Kam, N. W. S.; Lee, J., et al., Gold nanoparticles enhance the anti-leukemia action of a 6-mercaptopurine chemotherapeutic agent. *Langmuir* **2007**, *24*, 568-574.
244. Frens, G., Controlled nucleation for regulation of particle-size in monodisperse gold suspensions. *Nat. Phys. Sci.* **1973**, *241*, 20-22.
245. Brust, M.; Fink, J.; Bethell, D.; Schiffrin, D. J.; Kiely, C., Synthesis and reactions of functionalised gold nanoparticles. *Chem. Commun.* **1995**, 1655-1656.
246. Sun, X.; Jiang, X.; Dong, S.; Wang, E., One-step synthesis and size control of dendrimer-protected gold nanoparticles: A heat-treatment-based strategy. *Macromol. Rapid Commun.* **2003**, *24*, 1024-1028.
247. Mandal, M.; Ghosh, S. K.; Kundu, S.; Esumi, K.; Pal, T., UV photoactivation for size and shape controlled synthesis and coalescence of gold nanoparticles in micelles. *Langmuir* **2002**, *18*, 7792-7797.

248. Kimling, J.; Maier, M.; Okenve, B.; Kotaidis, V.; Ballot, H., et al., Turkevich method for gold nanoparticle synthesis revisited. *J. Phys. Chem. B* **2006**, 110, 15700-15707.
249. Caruso, R. A.; Ashokkumar, M.; Grieser, F., Sonochemical formation of gold sols. *Langmuir* **2002**, 18, 7831-7836.
250. Qi, Z.; Zhou, H.; Matsuda, N.; Honma, I.; Shimada, K., et al., Characterization of gold nanoparticles synthesized using sucrose by seeding formation in the solid phase and seeding growth in aqueous solution. *J. Phys. Chem. B* **2004**, 108, 7006-7011.
251. Wang, B.; Chen, K.; Jiang, S.; Reincke, F.; Tong, W., et al., Chitosan-mediated synthesis of gold nanoparticles on patterned poly(dimethylsiloxane) surfaces. *Biomacromolecules* **2006**, 7, 1203-1209.
252. Sakai, T.; Alexandridis, P., Single-step synthesis and stabilization of metal nanoparticles in aqueous pluronic block copolymer solutions at ambient temperature. *Langmuir* **2004**, 20, 8426-8430.
253. Xiao, J.; Qi, L., Surfactant-assisted, shape-controlled synthesis of gold nanocrystals. *Nanoscale* **2011**, 3, 1383-1396.
254. Yu, Y.; Chang, S.; Lee, C.; Wang, C. R. C., Gold nanorods: Electrochemical synthesis and optical properties. *J. Phys. Chem. B* **1997**, 101, 6661-6664.
255. Liu, Y.; Shipton, M. K.; Ryan, J.; Kaufman, E. D.; Franzen, S., et al., Synthesis, stability, and cellular internalization of gold nanoparticles containing mixed peptide-poly(ethylene glycol) monolayers. *Anal. Chem.* **2007**, 79, 2221-2229.
256. Jouikov, V. V., Electrochemical reactions of organosilicon compounds. *Russ. Chem. Rev.* **1997**, 66, 509.
257. Lukevics, E.; Ignatovich, L., ¹⁴Si biological activity of organosilicon compounds. In *Metallotherapeutic Drugs and Metal-Based Diagnostic Agents*, John Wiley & Sons, Ltd: **2005**; pp 83-107.
258. Owens III, D. E.; Peppas, N. A., Opsonization, biodistribution, and pharmacokinetics of polymeric nanoparticles. *Int. J. Pharm.* **2006**, 307, 93-102.
259. Shenoy, D.; Fu, W.; Li, J.; Crasto, C.; Jones, G., et al., Surface functionalization of gold nanoparticles using hetero-bifunctional poly(ethylene glycol) spacer for intracellular tracking and delivery. *Int. J. Nanomedicine* **2006**, 1, 51-57.
260. Wang, C.; Liu, C.; Wang, C.; Hua, T.; Obliosca, J. M., et al., Optimizing the size and surface properties of polyethylene glycol (PEG)-gold nanoparticles by intense x-ray irradiation. *J. Phys. D: Appl. Phys.* **2008**, 41, 195301.
261. El-Brolossy, T. A.; Abdallah, T.; Mohamed, M. B.; Abdallah, S.; Easawi, K., et al., Shape and size dependence of the surface plasmon resonance of gold nanoparticles studied by Photoacoustic technique. *Eur. Phys. J-Spec. Top.* **2008**, 153, 361-364.

262. Xiong, Y.; Xia, Y., Shape-controlled synthesis of metal nanostructures: The case of palladium. *Adv. Mater. (Weinheim, Ger.)* **2007**, 19, 3385-3391.
263. Zhou, M.; Wang, B.; Rozynek, Z.; Xie, Z.; Fossum, J. O., et al., Minute synthesis of extremely stable gold nanoparticles. *Nanotechnology* **2009**, 20, 505606.
264. Nikoobakht, B.; El-Sayed, M. A., Preparation and growth mechanism of gold nanorods (NRs) using seed-mediated growth method. *Chem. Mater.* **2003**, 15, 1957-1962.
265. Seo, D.; Yoo, C. I.; Park, J. C.; Park, S. M.; Ryu, S., et al., Directed surface overgrowth and morphology control of polyhedral gold nanocrystals. *Angew. Chem., Int. Ed.* **2008**, 47, 763-767.
266. Niidome, T.; Shiotani, A.; Katayama, Y.; Niidome, Y., Spherical and anisotropic gold nanomaterials in medical therapy. In *Nanotechnologies for the Life Sciences*, Wiley-VCH Verlag GmbH & Co. KGaA: **2007**.
267. Liu; Guyot-Sionnest, P., Mechanism of silver(I)-assisted growth of gold nanorods and bipyramids. *J. Phys. Chem. B* **2005**, 109, 22192-22200.
268. Raghunandan, D.; Bedre, M. D.; Basavaraja, S.; Sawle, B.; Manjunath, S. Y., et al., Rapid biosynthesis of irregular shaped gold nanoparticles from macerated aqueous extracellular dried clove buds (*Syzygium aromaticum*) solution. *Colloids Surf., B* **2010**, 79, 235-240.
269. Wang, S. H.; Lee, C. W.; Chiou, A.; Wei, P. K., Size-dependent endocytosis of gold nanoparticles studied by three-dimensional mapping of plasmonic scattering images. *J. Nanobiotechnol.* **2010**, 8, 33.
270. Hutter, E.; Boridy, S.; Labrecque, S.; Lalancette-Hébert, M.; Kriz, J., et al., Microglial response to gold nanoparticles. *ACS Nano* **2010**, 4, 2595-2606.

VITA

Lijin Xia comes from China. He received his bachelor's degree in science from Wuhan University. After graduation, he has been working for years in Guangdong, China. He got his master degree in Biochemistry later from Brigham Young University. In January of 2009, he entered University of Tennessee, Knoxville to pursue advanced degree in Biomedical Engineering. He received his Ph.D. degree in May of 2012.